

ULTRAFAST DYNAMICS OF TWO DIMENSIONAL MATERIALS

by

Dheeraj Golla

---

Copyright © Dheeraj Golla 2017

A Dissertation Submitted to the Faculty of the

DEPARTMENT OF PHYSICS

In Partial Fulfillment of the Requirements

For the Degree of

DOCTOR OF PHILOSOPHY

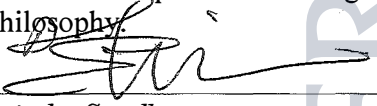
In the Graduate College

THE UNIVERSITY OF ARIZONA

2017

THE UNIVERSITY OF ARIZONA  
GRADUATE COLLEGE

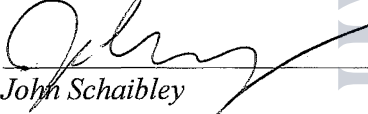
As members of the Dissertation Committee, we certify that we have read the dissertation prepared by *Dheeraj Golla*, titled *Ultrafast Dynamics of Two Dimensional Materials* and recommend that it be accepted as fulfilling the dissertation requirement for the Degree of Doctor of Philosophy.

  
\_\_\_\_\_  
*Arvinder Sandhu*

Date: 11/21/17

  
\_\_\_\_\_  
*Brian LeRoy*

Date: 11/21/17

  
\_\_\_\_\_  
*John Schaibley*

Date: 11/21/17

*Weigang Wang*  
\_\_\_\_\_  

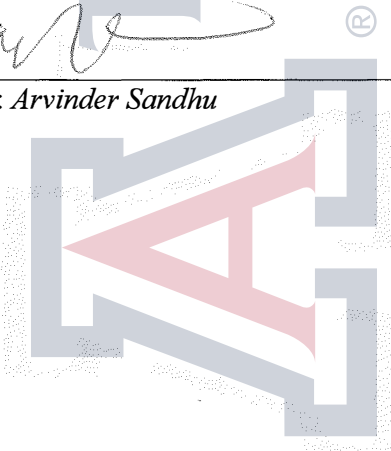

Date: 11/21/17

Final approval and acceptance of this dissertation is contingent upon the candidate's submission of the final copies of the dissertation to the Graduate College.

I hereby certify that I have read this dissertation prepared under my direction and recommend that it be accepted as fulfilling the dissertation requirement.

  
\_\_\_\_\_  
Dissertation Director: *Arvinder Sandhu*

Date: 12/4/2017



## STATEMENT BY AUTHOR

This dissertation has been submitted in partial fulfillment of the requirements for an advanced degree at the University of Arizona and is deposited in the University Library to be made available to borrowers under rules of the Library.

Brief quotations from this dissertation are allowable without special permission, provided that an accurate acknowledgement of the source is made. Requests for permission for extended quotation from or reproduction of this manuscript in whole or in part may be granted by the head of the major department or the Dean of the Graduate College when in his or her judgment the proposed use of the material is in the interests of scholarship. In all other instances, however, permission must be obtained from the author.

SIGNED: Dheeraj Golla

## Acknowledgements

Any scientific work is seldom done in isolation. I owe thanks to many people who have helped me through my time in graduate school. The biggest influence in shaping my scientific thinking so far has been my advisor Arvinder Sandhu. He taught me to question everything and never take anything for granted. I greatly enjoyed our discussions and I admire his ability to untiringly pursue the finer details. I would like to thank Niranjan, Henry, Adam and Chen-Ting who mentored me and softened my transition to experimental physics. I would like to thank Alex Plunkett, Alex Brasington, Nate, Shengqiang and Arpit for being the best lab mates ever. I would like to thank Brian LeRoy and John Schaibley for scientific guidance. Their expertise allowed me to pursue projects spanning the major fields: ultrafast spectroscopy and 2D materials. I would also like to thank Sumit Majumdar, Rolf Binder and Weigang Wang for agreeing to serve on my committee. Finally, I would like to thank Hannah, whose presence in my life for the last two years made it all worth it.

# Dedication

To my wonderful parents, Babu and Giri Kumari.

# Table of Contents

<b>TABLE OF FIGURES</b>	<b>9</b>
<b>ABSTRACT</b>	<b>15</b>
<b>CHAPTER 1. INTRODUCTION</b>	<b>17</b>
<b>CHAPTER 2. EXPERIMENTAL METHODS</b>	<b>19</b>
<b>2.1 Description of a femtosecond pulse</b>	<b>20</b>
<b>2.2 Generation and amplification of femtosecond pulses</b>	<b>23</b>
2.2.1 Kerr Lens Mode-locking	23
2.2.2 Chirped Pulse Amplification	29
2.2.3 Frequency Resolved Optical Gating	32
<b>2.3 Pump-probe spectroscopy</b>	<b>34</b>
<b>CHAPTER 3. OPTICAL PROPERTIES AND SPECTROSCOPY OF GRAPHENE</b>	<b>37</b>
<b>3.1 Electronic properties</b>	<b>37</b>
<b>3.2 CVD growth procedure</b>	<b>41</b>
<b>3.3 Raman Spectroscopy of Graphene</b>	<b>44</b>
<b>3.4 Optical absorption spectrum of graphene</b>	<b>51</b>
<b>3.5 Multibody effects in graphene</b>	<b>54</b>

3.5.1	Electron-phonon interaction in graphene	55
3.5.2	Pump-probe spectroscopy of graphene	57
3.5.3	Bandgap renormalization in graphene	59
<b>CHAPTER 4. ULTRAFAST DYNAMICS OF GRAPHENE HETEROSTRUCTURES</b>		<b>63</b>
4.1	Optical Characterization of the thickness of hBN	64
4.2	Transferring Graphene on hBN	71
4.3	Electronic properties of g-hBN	73
4.4	Ultrafast relaxation of hot phonons in g-hBN Heterostructures	76
4.4.1	Experimental Results	78
4.4.2	Two-Temperature Model	81
4.4.3	Heat transfer in graphene heterostructures	88
4.4.4	Theoretical aspects of heat transfer in g-hBN	90
<b>CHAPTER 5. PHONON INDUCED RENORMALIZATION IN TRANSITION METAL DICHALCOGENIDES</b>		<b>94</b>
5.1	Static spectroscopy of WS <sub>2</sub> and MoS <sub>2</sub>	96
5.2	Non-degenerate pump-probe spectroscopy of WS <sub>2</sub>	99
5.3	Modelling recombination rates	106
<b>CHAPTER 6. CONCLUSIONS</b>		<b>112</b>
<b>APPENDIX A</b>		<b>114</b>

<b>APPENDIX B</b>	<b>116</b>
<b>B.1 High energy excitons in graphene</b>	<b>116</b>
<b>B.2 XUV spectroscopy of magnetic materials</b>	<b>118</b>
<b>REFERENCES</b>	<b>121</b>

# Table of Figures

Figure 2.1: (a) Fourier transform limited ultrashort pulse measuring 5.5 fs. (b) Chirped pulse of the same duration. (c) and (d) Fourier transforms of pulses in (a) and (b) respectively.....	21
Figure 2.2: (a) Simulated pulse train with a 500 fs repetition rate. (b) Fourier transform of the pulse train in (a) showing comb structure...	24
Figure 2.3: (a) An ultrafast pulse showing the peak which gets focused and the wings that do not pass through the aperture. (b) A schematic of a cavity that is set up for Kerr lens mode-locking.....	27
Figure 2.4: Schematic of a Kerr lens mode-locked ultrafast oscillator.	29
Figure 2.5: Schematic of a multipass chirped pulse amplifier.....	31
Figure 2.6: (a) Experimental setup for a FROG scan. (b) Spectrogram of a 40 fs pulse. (c) Reconstructed electric field intensity (blue) and phase of the same pulse as in (b) showing a quadratic phase (red).....	34
Figure 2.7: Schematic representation of a pump-probe experiment in the transmission geometry.....	36
Figure 3.1: (a) Hexagonal crystal structure of graphene showing the unit cell (parallelogram) (b) First Brillouin zone in reciprocal space showing important points and reciprocal lattice vectors .....	38
Figure 3.2: Electronic bandstructure of graphene. Inset: Close up near Dirac point showing linear dispersion.....	40
Figure 3.3: Typical CVD grown graphene flake showing petal like six-fold symmetry with multilayers in the center .....	43

Figure 3.4: Energy diagram of a Raman process showing Stokes, Rayleigh and Anti-Stokes scattering processes .....	45
Figure 3.5: Typical experimental setup for Raman spectroscopy. ....	46
Figure 3.6: Typical Raman spectrum for pristine CVD graphene (red) and graphene with defects (blue) .....	47
Figure 3.7 : Position of the G peak (left) and the 2D peak (right) as a function of electron and hole doping. Solid lines denote adiabatic DFT calculations. Adapted with permission from Das et al., Nature Nanotechnology, vol. 3, no. 4, pp. 210-215, 2008. ....	49
Figure 3.8: Variation of $I_D/I_G$ ratio with average crystalline size of graphene in the amorphous carbon regime (a-C) and the nanocrystallite graphene regime (nc-G). Figure adapted with permission from Ferrari and Robertson, Physical Review B, Vol 61, number 20, pages 14095-14107 (2000).....	50
Figure 3.9: 2D line strength as a function of the number of laser exposures. Solid lines are decaying exponential fits. Adapted from “Time Domain Spectroscopy of graphene”, Adam Roberts (2012) .....	51
Figure 3.10: (left) interband and (right) intraband electronic transitions responsible for the dynamic conductivity in graphene.....	53
Figure 3.11: Pump induced change in the absorption spectrum of graphene due to electron-phonon renormalization.....	56
Figure 3.12: The above figure shows a schematic of the pump probe setup in a transmission geometry. ....	57
Figure 3.13: $\Delta T/T_0$ value of the probe pulse at pump-probe energies of (a) 4.8 eV, (b) 3.2 eV, and (c) 1.6 eV. (d) The linear absorption profile	

indicating the probing energies relative to the saddle point absorption maxima. ....	58
Figure 3.14: $\Delta T/T_0$ as a function of probe photon energy at three time delays (4, 40 and 400 ps). The pump fluence is $400 \mu J/cm^2$ and fixed pump energy of 4.8 eV. Each panel is labeled with a specific phonon temperature value. The calculated results for coupling to acoustic phonons only with $D^{eff}_{ac} = 5.3 eV$ are shown in red (thick line) and acoustic + optical phonons with $D^{eff}_{op} = 11 eV\text{\AA}$ are shown in green (thin line). The dashed black line (top panel) shows acoustic-only coupling with $D^{eff}_{ac} = 20 eV$ . The dash-dotted gray line (top panel) shows the statically screened Hartree-Fock result for e-e interaction (multiplied by 50 for ease of comparison) using thermally excited carriers. ....	61
Figure 4.1: The optical contrast of hBN on SiO <sub>2</sub> /Si substrate as a function of the wavelength of light. Different curves correspond to flakes with different number of layers. The dark solid lines are the fits obtained using the multilayer interference calculations. The bottom panels show optical microscope images at three discrete wavelengths corresponding to positive, zero, and negative contrast. The scale bar represents $5 \mu m$ . ....	65
Figure 4.2 : (a) Calculated optical contrast as a function of the wavelength of light and thickness of hBN for a 282 nm SiO <sub>2</sub> layer. (b) Line out at 516nm shows that the contrast varies linearly with the thickness of the hBN flake between 1 and 80 layers.....	69
Figure 4.3: The comparison of optical contrast image with the atomic force microscopy image. (a) AFM image of a hBN flake on a SiO <sub>2</sub>	

substrate. (b) Optical contrast image of the same hBN flake. The thickness of the two central regions in number of layers is marked on the images. Color bar representing the number of layers is common between the AFM and optical contrast image. The optical contrast values are converted to thickness using 2.5 % per layer. Inset shows the microscope image of hBN flake. The length scale bar represents 2 nm in all images. The comparison illustrates the ability of the optical contrast method to measure the thickness of hBN flakes as well as differentiate small steps corresponding to changes in thickness of a few layers of hBN..... 70

Figure 4.4: Schematic for the steps involved in transferring graphene onto hBN flakes on top of a fused silica substrate..... 72

Figure 4.5: Charge fluctuations (left), represented by variation in Fermi level, and surface topography (right) for graphene on hBN (top) and SiO<sub>2</sub> (bottom). Image adapted from Jiamin Xue et al, Nature Materials, Vol 10, pages 282 – 285 (2011). ..... 74

Figure 4.6: Bandstructure of graphene near the Dirac point modified by the weak periodic superlattice potential. New Dirac points are formed around the original Dirac point. .... 76

Figure 4.7: (a) Optical image of sample 1. The mean thickness of the hBN flake shown here is 118 nm as measured using AFM. Spot marked 1 is g-hBN and spot marked 2 is g-SiO<sub>2</sub> (b) Raman spectra of the graphene on hBN (red) and on SiO<sub>2</sub> (black). The curves are vertically offset for clarity..... 79

Figure 4.8: Experimental differential reflectivity curves for different samples of g-hBN pumped using  $60 \mu J/cm^2$  per pulse. The reflectivity of g-SiO<sub>2</sub> is shown for comparison (red: g-hBN and black: g- SiO<sub>2</sub>) ..... 80

Figure 4.9: (a) Reflectivity curves for plain SiO<sub>2</sub>/Si chip and hBN flakes over various thicknesses. (b) Long scan of time delay of g-hBN showing a flat response after the initial cooling. .... 81

Figure 4.10: Differential reflectivity curves versus temperature for g-hBN (red) and g-SiO<sub>2</sub> (black) calculated using the two-temperature model. .... 84

Figure 4.11 : (a) Differential reflectivity curves for graphene-hBN with different pump fluences:  $80 \mu J/cm^2$  (orange),  $60 \mu J/cm^2$  (green) and  $50 \mu J/cm^2$  (blue). (b) Differential reflectivity curves for graphene-SiO<sub>2</sub> for the same fluences. Inset: Electronic (red) and phonon (black) temperature profiles for the case with the lowest fluence. .... 85

Figure 4.12: Transient differential reflectivity curves for g-hBN calculated ignoring (yellow) and including (red) the initial p-doping doping. .... 88

Figure 4.13: Different heat flow pathways available to photoexcited charge carriers. .... 91

Figure 5.1: Schematic representation of the bandstructure of a TMD near the K point. Defect states, free and localized excitons are also shown..... 97

Figure 5.2: Optical images of CVD grown WS<sub>2</sub> (left) and MoS<sub>2</sub> on a c-sapphire substrate. .... 98

Figure 5.3: Absorbance (black) and photoluminescence (red) of (a) WS<sub>2</sub> and (b) MoS<sub>2</sub> ..... 98

Figure 5.4: Transient absorbance curves for WS <sub>2</sub> at (a) 1.92 eV (b) 2 eV and (c) 2.07 eV at a pump fluence of 1500 $\mu\text{J}/\text{cm}^2$ .....	100
Figure 5.5: (a) PL of WS <sub>2</sub> sample at 4.3 K (b) Transient absorbance of WS <sub>2</sub> with varying fluence.....	102
Figure 5.6: Energy schematic of the model used to simulate dynamics showing the coupling between states.....	107
Figure 5.7: Calculated absorbance curves simulating the data in Fig 5.3 using Eqn. 5.7.....	109
Figure 5.8: (a) Measured room temperature absorbance (blue) and temperature renormalized absorbance using Eqn. 5.8. (b) Change in absorbance due to renormalization. ....	111
Figure A.1: Transient absorption curves for MoS <sub>2</sub> with probe energy (a) 1.77 eV, (b) 1.86 eV and (c) 2.02 eV. The fluence is fixed at 1500 $\mu\text{J}/\text{cm}^2$ . .....	115
Figure B.1: Optical absorption spectrum with and without electron-hole interactions for (a) monolayer and (b) bilayer graphene. Adapted with permission from Li Yang, “Excitons in intrinsic and bilayer graphene”, PHYSICAL REVIEW B 83, 085405 (2011).....	117
Figure B.2: Sample geometry for probing PMA effect in CoFeB ferromagnet with a MgO insulating capping layer. ....	120

# ABSTRACT

Two dimensional (2D) materials are poised to revolutionize the future of optics and electronics. The past decade saw intense research centered around graphene. More recently, the tide has shifted to a bigger class of two-dimensional materials including graphene but more expansive in their capabilities. The so called ‘2D material zoo’ includes metals, semi-metals, semiconductors, superconductors and insulators. The possibility of mixing and matching 2D materials to fabricate heterostructures with desirable properties is very exciting.

To make devices with superior electronic, optical and thermal properties, we need to understand how the electrons, phonons and other quasi particles interact with each other and exchange energy in the femtosecond and nanosecond timescales. To measure the timescales of energy distribution and dissipation, I used ultrafast pump-probe spectroscopy to perform time-domain measurements of optical absorption. This approach allows us to understand the impact of many-body interactions on the bandstructure and carrier dynamics of 2D materials.

After a brief introduction to femtosecond laser spectroscopy, I will explore the transient absorption dynamics of three classes of 2D materials: intrinsic graphene, graphene-hBN heterostructures and Transition Metal Dichalcogenides (TMDs). We will see that using pump-probe measurements around the high energy M-point of intrinsic

graphene, we can extract the value of the acoustic deformation potential which is vital in characterizing the electron-acoustic phonon interactions. In the next part of the thesis, I will delineate the role of the substrate in the cooling dynamics in graphene devices. We will see that excited carriers in graphene on hBN substrates cool much faster than on SiO<sub>2</sub> substrates due to faster decay of the optical phonons in graphene-hBN heterostructures. These results show that graphene-hBN heterostructures can solve the hot phonon bottleneck that plagues graphene devices at high power densities. In the last part, I will demonstrate the role of phonon induced bandgap renormalization in the carrier dynamics of TMD materials and measure the timescale of phonon decay through the generation of low-energy phonons and transfer to the substrate. This study will help us understand carrier recombination in TMD devices under high-bias conditions which show great potential in opto-electronic applications such as photovoltaics, LEDs etc.

# CHAPTER 1.

## Introduction

The rapid pace of development in the field of electronics means we are pushing the limit on how many transistors and other active elements we can pack into a single chip. Consequently, device dimensions are scaling down while current densities are increasing. Pushing the frontier in this direction requires that we overcome various challenges. The rise of 2D semiconductors since the discovery of graphene has been meteoric and it poised to offer alternative solutions to the problems encountered by scaling down the dimensions of silicon transistors. The reduced dimensionality of 2D structures causes increased many-body interactions due to reduced screening effects. 2D materials offer a convenient test bed to observe exotic physics in table top experiments. State of the art vapor deposition and transfer techniques make it possible to construct vertical heterostructures with electronic or optical properties that are engineered to suit specific applications. To enable a tailored approach to heterostructure construction, a thorough understanding of carrier dynamics is essential. Relaxation of excited carriers via multibody scattering processes is the dominant mechanism of energy loss. Pump-probe spectroscopy using ultrafast femtosecond lasers has made it possible to study carrier dynamics directly in the time domain. In this thesis, I will describe a series of experimental investigations probing the dynamics of two

dimensional materials using mainly pump-probe spectroscopy techniques. In chapter two, I will describe the physics of ultrafast pulses; particularly, their generation, amplification and measurement. In chapter three, starting with the electronic properties of graphene, I will discuss carrier dynamics in graphene where electron-phonon interactions lead to bandstructure renormalization near the M-point of the Brillouin zone. Chapter four deals with carrier dynamics in heterostructures of graphene and hexagonal boron nitride (hBN). In this chapter I will discuss our experimental results where we prove conclusively that hBN substrates cause faster carrier relaxation in graphene than SiO<sub>2</sub> substrates due to enhanced optical phonon decay. In chapter five, I will describe our results in non-degenerate pump-probe spectroscopy of Transition Metal Dichalcogenides where we see an interesting interplay of excitonic dynamics due to mid-gap defect states and carrier-phonon renormalization. Understanding excitonic dynamics is important to reduce recombination rates in photoexcited TMDs and leverage their potential as a photovoltaic material.

# CHAPTER 2.

## Experimental Methods

Coherent laser pulses shorter than one picosecond were first produced by mode-locked dye lasers more than forty years ago<sup>1</sup>. State-of-the-art lasers capable of producing pulses with durations in the few-femtosecond range can be purchased commercially at prices within the reach of small research groups.

The commercial interest in ultrafast lasers is driven by their application in materials processing and spectroscopy. Ultrafast lasers are used in micro and nanomachining of metals, semiconductors and soft materials. Ultrashort pulses deliver large quantities of energy at timescales far less than thermal diffusion timescales of materials. This reduces heat diffusion to regions adjacent to the processed area, thereby producing sharp edges and a high-quality finish. Ultrafast lasers are ideally suited for processing soft matter like bio-polymers (e.g. used in the manufacturing of stents) and tissue<sup>2</sup>. In fact, the widely advertised bladeless Lasik surgery uses femtosecond lasers to cut a flap on the cornea to expose the lens.

Rapid advances in technology have brought femtosecond time domain spectroscopy into the purview of research labs around the world. Modern Ti-Sapphire based amplified lasers can produce peak powers in the terawatt range. This makes ultrafast lasers useful in studying the

non-linear properties of materials such as two-photon absorption, saturable absorption etc.

In this chapter, I will talk about the various experimental aspects of a typical ultrafast spectroscopy setup starting with the generation, manipulation and measurement of ultrafast pulses. I will also briefly describe data acquisition schemes and signal-noise considerations in pump-probe experiments.

## 2.1 Description of a femtosecond pulse

An ultrashort light pulse can be mathematically described by expression of the electric field as a function of time. Sinusoidal electric fields are best described using the complex number notation, while keeping in mind that it is the real value of the complex field that is physical. The expression for a typical ultrashort pulse is (ignoring the polarization):

$$E(t) = E_0 e^{-i(\omega_0 t - \varphi(t))} e^{-\frac{t^2}{2\tau^2}} \quad 2.1$$

Here,  $\omega_0$  is the central frequency,  $\varphi(t)$  is the temporal variation of the phase,  $E_0$  is the maximum amplitude and  $\tau$  is the pulse width. Throughout this thesis, I will always refer to the pulsewidth as the value for  $\tau$  in Eqn. 2.1. A single pulse with a pulsewidth of 5.5 fs is shown along with the intensity envelope in *Figure 2.1* (a). The instantaneous frequency is the derivative of the temporal phase:

$$\omega(t) = \frac{d\varphi(t)}{dt} \quad 2.2$$

For the pulse shown in Fig. 2.1 (a), I assume that  $\varphi(t)$  is constant or more generally, a linearly increasing with time, i.e. the pulse is unchirped. This means that the instantaneous frequency of an

unchirped pulse is constant. A chirped pulse is one where the instantaneous frequency varies with time. A linear variation of  $\varphi(t)$  is a simple shift of the center frequency and is not a chirp. To obtain a linear chirp, the phase has to increase quadratically with time. Fig. 2.1(b) shows the time profile of a chirped pulse where the temporal phase varies quadratically as:

$$\varphi(t) = 0.006 t^2 \quad 2.3$$

The red lines in Figs. 2.1 (a) and (b) mark the normalized intensity of the light pulse. The intensity is proportional to the square of the electric field.

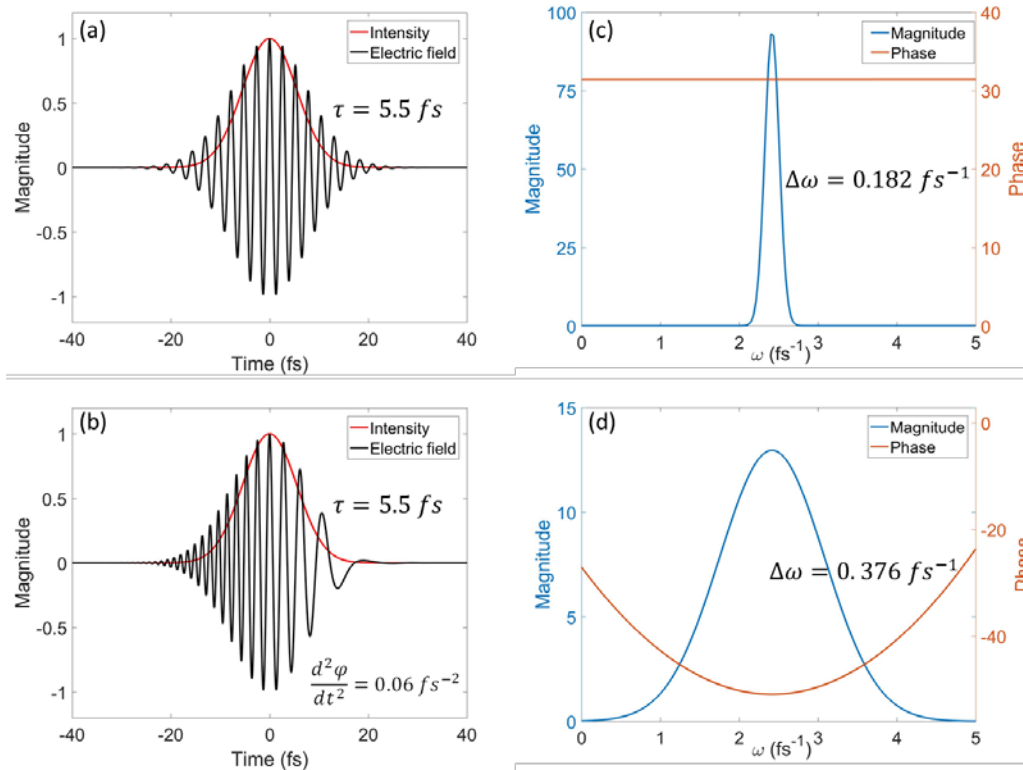


Figure 2.1: (a) Fourier transform limited ultrashort pulse measuring 5.5 fs. (b) Chirped pulse of the same duration. (c) and (d) Fourier transforms of pulses in (a) and (b) respectively.

The spectrum of the pulse is given by the Fourier transform of the time domain expression. The spectrum has important physical significance because of the ease of its measurement in the laboratory. Taking the Fourier transform of the expression in Eqn. 2.1, we get:

$$\begin{aligned}\tilde{E}(\omega) &= \int_{-\infty}^{\infty} E(t)e^{-i\omega t} dt \\ &= \tilde{E}_0 e^{-\frac{(\omega-\omega_0)^2}{2(\Delta\omega)^2}}\end{aligned}\tag{2.4}$$

Here,  $\Delta\omega$  is the spectral bandwidth of the pulse whose spectrum centered around  $\omega_0$ . Being inverse Fourier variables,  $\Delta\omega$  and  $\tau$  are related to each other by the relation:

$$\Delta\omega = \frac{1}{\tau}\tag{2.5}$$

*Figure 2.1* (c) and (d) show the Fourier transform of the pulses in Figs. 2.1 (a) and (b) respectively. We note that the spectral phase is flat for the unchirped pulse and varies quadratically for the chirped pulse. We see that even though the unchirped pulse and the chirped pulse have the same temporal width ( $\tau = 5.5 \text{ fs}$ ), the spectrum of the chirped pulse is more than twice as broad as that of the unchirped pulse because of the additional frequency components generated due to chirping. From Eqn. 2.5, we see that in order to generate a short pulse, it is necessary to have a large spectral bandwidth. More generally, a broad bandwidth with all the spectral components adding up in phase generates a short pulse. The shortest pulse that can be generated with a given bandwidth is known as the Fourier transform-limited pulse.

## 2.2 Generation and amplification of femtosecond pulses

A typical ultrafast laser system like the one in our lab consists of a laser oscillator producing the ultrafast pulses and an amplifier to increase the pulse energy. In the following sections, I will briefly describe the working principles of an ultrafast laser.

### 2.2.1 Kerr Lens Mode-locking

In a typical laser with an inhomogenously broadened gain profile, numerous longitudinal cavity modes are oscillating simultaneously with random phases and amplitudes. Ultrafast pulses of light are produced via mode-locking, i.e. locking the phase of adjacent cavity modes of the laser cavity so that they constructively add up to produce short pulses. Mode-locking produces a train of ultrafast pulses. The temporal spacing between the pulses ( $t_{rep}$ ) is determined by the roundtrip travel time for a pulse in the cavity. If  $L$  is the length of the cavity, then  $L_{eff} \approx 2L$  is the total optical distance travelled by the pulse in one round trip.

$$t_{rep} = \frac{L_{eff}}{c} \quad 2.6$$

In the frequency domain, the cavity modes that are supported by the cavity (and are phase locked) are given by:

$$\omega_n = n \left( \frac{2\pi c}{L_{eff}} \right) = \frac{2\pi n}{t_{rep}} \quad 2.7$$

Where  $n$  is a positive integer. The gain bandwidth of the lasing medium (usually a titanium-doped sapphire crystal) needs to span multiple cavity modes so that they can be mode-locked and produce a train of ultrafast pulses. Thus, in the frequency domain, the spectrum

of an ultrafast train of pulses is a comb of frequencies spaced  $\omega_{cav} = \frac{2\pi c}{L_{eff}}$  apart. This frequency comb spectrum of an ultrafast laser has spawned a whole new field of high precision spectroscopy<sup>3</sup>. A train of ultrafast pulses ( $\tau = 5.5 fs$ ) spaced  $t_{rep} = 500 fs$  apart and the equivalent frequency comb spectrum with comb spacing  $\omega_{cav} = 0.0125 fs^{-1}$  is shown in Fig. 2.2. The broad envelope of the frequency comb spectrum is the gain spectrum of the gain medium.

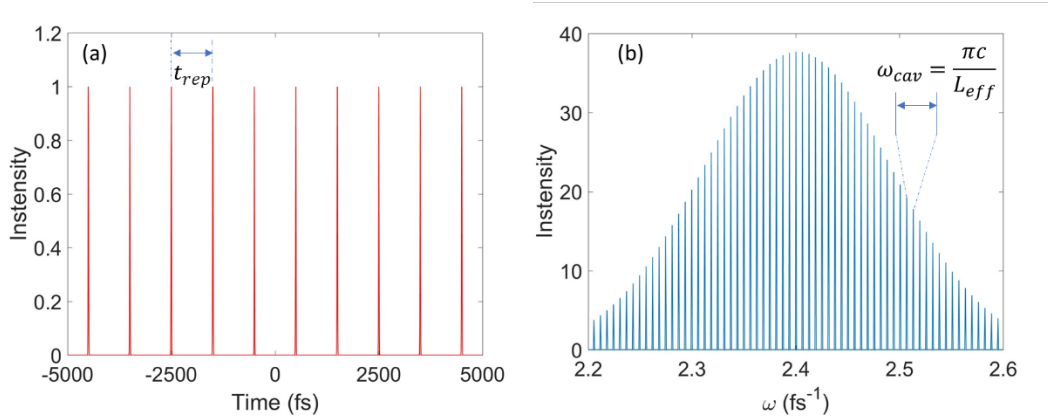


Figure 2.2: (a) Simulated pulse train with a 500 fs repetition rate. (b) Fourier transform of the pulse train in (a) showing comb structure.

We can estimate the number of oscillating longitudinal cavity modes using:

$$N = \frac{\Delta\omega}{\omega_{cav}} \quad 2.8$$

In our lab, we use a laser oscillator (Griffin-I, KMLabs) with a repetition rate of 78 MHz, corresponding to  $t_{rep} = 12.83 ns$ . This gives us a comb spacing of  $\omega_{cav} = 4.897 \times 10^{-7} fs^{-1}$ . From Eqn. 2.5, we know that the gain bandwidth of a transform limited 30 fs pulse (typical) is  $\Delta\omega = 0.033 fs^{-1}$ . Plugging the numbers in Eqn. 2.8, we estimate about

67,388 cavity modes oscillating with locked phases in our mode-locked laser.

Mode-locking is achieved in practice by modulating the loss (or gain) of the laser cavity at the repetition rate  $t_{rep}$ . We can imagine this modulation as the ‘opening’ and ‘closing’ of a window in the cavity when light can pass through it. Modulating the loss discriminates against all possibilities except the one where all modes oscillate in phase, thus confining the electric field in space and time so that the pulse can pass through the gain medium when the window is open. Modulating the loss in a cavity can be done ‘actively’ using a fast acting aperture like an Acousto-Optic Modulator or ‘passively’ by placing a saturable absorber in the cavity. Almost all modern ultrafast lasers work based on a passive mode-locking mechanism called Kerr lens mode-locking. An ultrashort pulse propagating inside a mode-locked cavity is a soliton solution of a non-linear Schrodinger equation (Eqn. 2.9) where the dispersion effects (playing the role of the kinetic energy) are balanced by the non-linear Kerr effects (potential energy term).

$$j \frac{\partial A(z, t)}{\partial z} = -D_2 \frac{\partial^2 A}{\partial t^2} + \delta |A|^2 A \quad 2.9$$

Here,  $A(z, t)$  represents the vector potential of the light field,  $z$  is the direction of propagation,  $D_2$  represents the chromatic dispersion and  $\delta$  is a constant proportional to the non-linear refractive index of the medium. Precise modelling of generation of ultrafast pulses is an active and challenging area of research because of the tangled spatial and temporal dynamics involved. Instead, I will try to qualitatively describe the physics behind the mode-locking process.

The Kerr effect is an electro-optic effect where the refractive index of a medium changes with the intensity,  $I(r, t)$ , of the incident light.

$$n(r, t) = n_0 + n_2 I(r, t) \quad 2.10$$

Here,  $n_0$  is the usual refractive index of the material and  $n_2$  is the non-linear refractive index coefficient of the material. All centrosymmetric materials have a non-zero  $n_2$ . When an ultrafast pulse passes through a Kerr medium, the refractive index of the medium affecting the pulse is maximum at the peak intensity of the pulse. Since the pulse is Gaussian-shaped both spatially and temporally, the Kerr medium acts as an effective lens. The medium is effectively optically denser near the center (Gaussian peak) than on the edges. In the time domain, the strongest focusing occurs at the temporal peak of the pulse and weak focusing occurs at the wings, thereby entangling the spatial and temporal dynamics of the beam. This effectively generates a light pulse with a time-dependent mode size. By placing a physical aperture in the cavity after the Kerr medium, we can selectively pass the most intense part of the beam near the temporal peak (which is focused tighter), effectively shortening the pulse. This process is schematically shown in *Figure 2.3*. The success of this mechanism rests on the fact that the Kerr effect response times of the medium are as fast as the ultrafast pulse.

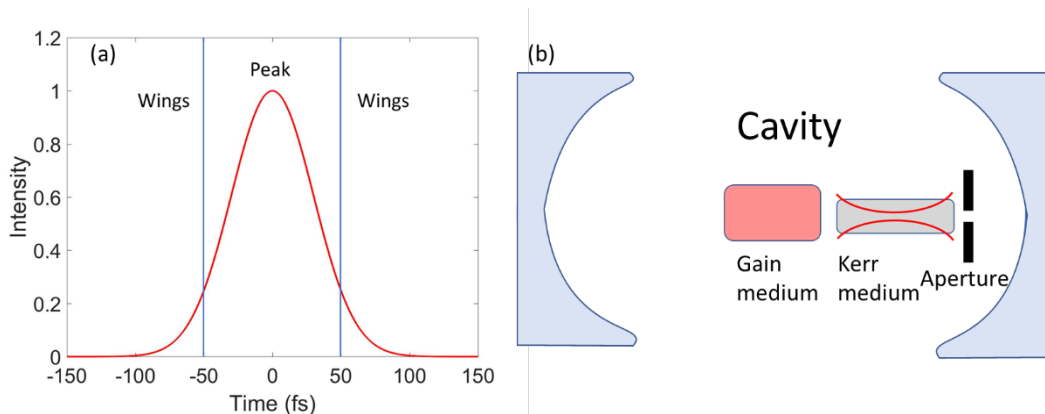


Figure 2.3: (a) An ultrafast pulse showing the peak which gets focused and the wings that do not pass through the aperture. (b) A schematic of a cavity that is set up for Kerr lens mode-locking.

In practice, the gain medium doubles as the Kerr medium and instead of placing an aperture (called a hard aperture), we can use a soft aperture scheme where an effective aperture is created on the gain medium by focusing the pump beam to a spot size that is smaller resonator spot size (when the laser is not mode-locked) but is matched to the spot size of a self-focused ultrafast pulse. Since the gain is proportional to the overlap of the pump and laser beams, this configuration preferentially picks the mode-locked oscillation mode (pulsed mode) as opposed to the usual continuous wave mode (CW mode).

The Kerr effect also causes the laser beam to undergo self-phase modulation (SPM) along with the self-focusing effect. As the pulse passes through the medium it experiences a refractive index-dependent phase shift:

$$\varphi(t) = \omega_0 t - \frac{2\pi}{\lambda_0} n(t) \cdot d \quad 2.11$$

Using Eqn. 2.3 the instantaneous frequency is:

$$\omega(t) = \frac{d\varphi(t)}{dt} = \omega_0 + \frac{2\pi d}{\lambda_0} I_0 \frac{2t}{\tau^2} e^{-\frac{t^2}{\tau^2}} \quad 2.12$$

We see that the leading edge ( $t < 0$ ) of the pulse is red-shifted and the trailing edge ( $t > 0$ ) is blue-shifted. This frequency shift can be approximated as a linear chirp in the central portion of the curve,

$$\omega(t) \approx \omega_0 + \alpha \cdot t \quad 2.13$$

where  $\alpha = \frac{2\pi d}{\lambda_0} I_0 \frac{2}{\tau^2}$ .

The effect of SPM on the pulse is similar to that of positive or normal dispersion, i.e. it causes an effective upchirp (increase in frequency with time) in the pulse. Since ultrafast pulses have a comparatively broad spectrum, and all materials show chromatic dispersion to some degree, we can expect that the pulse will suffer additional positive (or normal) dispersion in the cavity due to chromatic dispersion. The chromatic dispersion introduced into a pulse can be quantified by the group delay dispersion (GDD) of the cavity.

$$D = \frac{-\lambda}{c} \frac{d^2 n}{d\lambda^2} \quad 2.14$$

We need to compensate this dispersion inside the cavity. This is done using a prism dispersion compensator. The basic principle behind a prism compensator is shown in *Figure 2.4*. The lower frequency components of the light pulse travel a longer distance than the higher frequency components, causing anomalous (or negative) dispersion. By moving one of the prisms in and out, i.e. changing the value of  $L$ , we can control the amount of negative chirp imparted to the pulse.

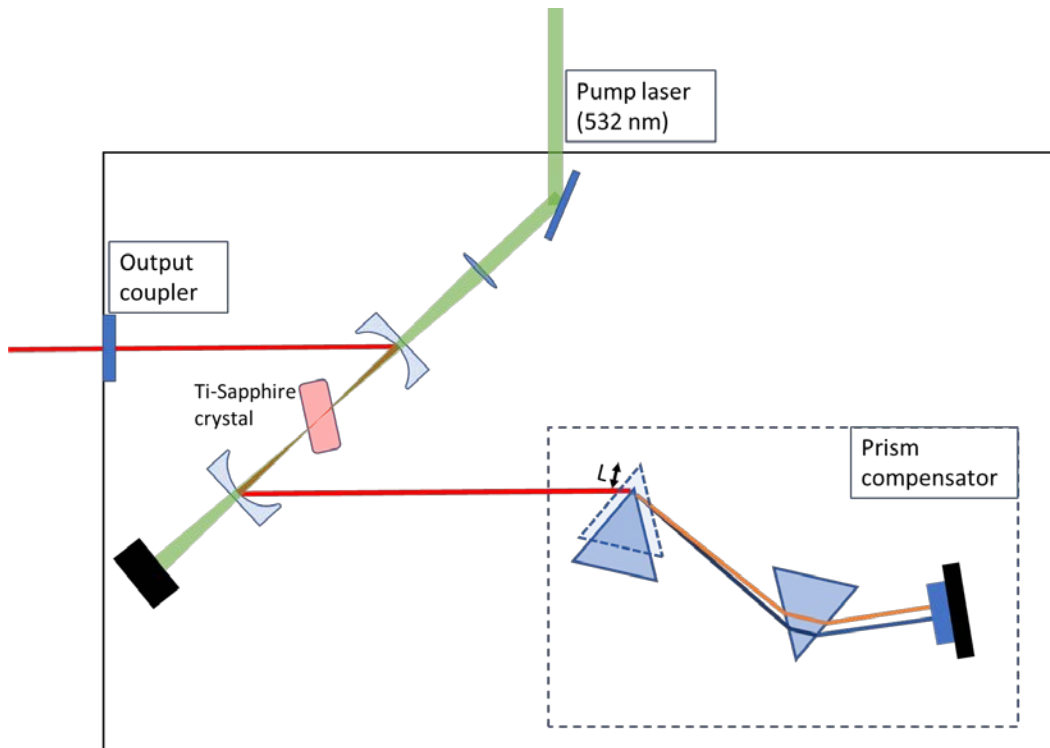


Figure 2.4: Schematic of a Kerr lens mode-locked ultrafast oscillator.

### 2.2.2 Chirped Pulse Amplification

The pulses produced in the laser oscillator via mode-locking have an energy of about  $6 \text{ nJ}$ . The pulse duration is typically  $\sim 30 \text{ fs}$ , thus peak power is  $\sim 200 \text{ kW}$ . Upon focusing to a spot size of  $1000 \mu\text{m}^2$ , the peak intensity that we can expect is  $\sim 20 \frac{\text{GW}}{\text{cm}^2}$ . This is not sufficient to see highly non-linear effects like High Harmonic Generation (which is used to generate XUV pulses that are used in our lab to study attosecond level dynamics of atoms, molecules and materials). In order to increase the pulse energy, we amplify the femtosecond seed pulses from the oscillator using a multipass amplifier.

The amplification stage mimics the gain stage in the oscillator without the cavity. Energy is pumped into a gain medium (Ti-Sapphire)

using a pump laser. The seed pulse extracts the stored energy in a stimulated emission process and is amplified in the process. The pump laser for the amplification stage is a kHz repetition rate Q-switched Nd:YLF laser which emits light at  $527\text{ nm}$ . The pulse duration is about  $400\text{ ns}$ , and pulse energy is about  $20\text{ mJ}$ . For maximum gain extraction and a high peak pulse power, we need to reduce the repetition rate of the oscillator pulse train from  $78\text{ MHz}$  to  $1\text{ KHz}$ . This is done by passing the seed pulse train through a Pockels cell. A Pockels cell is essentially an electro-optic device that rotates the plane of polarization of the light by  $\pi/2$  when a pulsed high voltage ( $\sim 5\text{ kV}$ ) is applied across it. The width and repetition rate of the high voltage pulse train is timed to coincide precisely with one seed pulse every millisecond (matching the repetition rate of the pump laser). Using a crossed polarizer to let the rotated pulses pass through and reject the others, we effectively reduce the repetition rate of the seed pulse train to  $1\text{ kHz}$ .

To avoid damage to the crystal and other thermal and non-linear distortion effects, the seed pulse is stretched from  $30\text{ fs}$  to  $\sim 200\text{ ps}$  using a grating stretcher. The stretcher imparts a positive chirp to the pulse by propagating the blue components farther than the red components. Since the  $527\text{ nm}$  pump pulse duration is much longer ( $\sim 200\text{ ns}$ ) than the stretched  $780\text{ nm}$  seed pulse ( $\sim 200\text{ ps}$ ), the seed can be sent around into the gain medium multiple times using a ring geometry to repeatedly extract gain from a single pump pulse, limited only by the saturation limit of the gain medium. Typically, we choose to use 10 or 11 passes to extract maximum gain from the crystal. To prevent thermal damage and wavefront distortion to the crystal, it is

held under high vacuum ( $\sim 10^{-9}$  torr) and at liquid nitrogen temperature (77 K). After amplification, the pulse energy is  $\sim 2$  mJ. We can estimate the gain factor in a multipass chirped pulse amplifier as  $\sim 3 \times 10^5$ . The amplified seed pulse is sent into a grating compressor, which works like the opposite of the stretcher, to compress the pulse back to 30 – 50 fs.

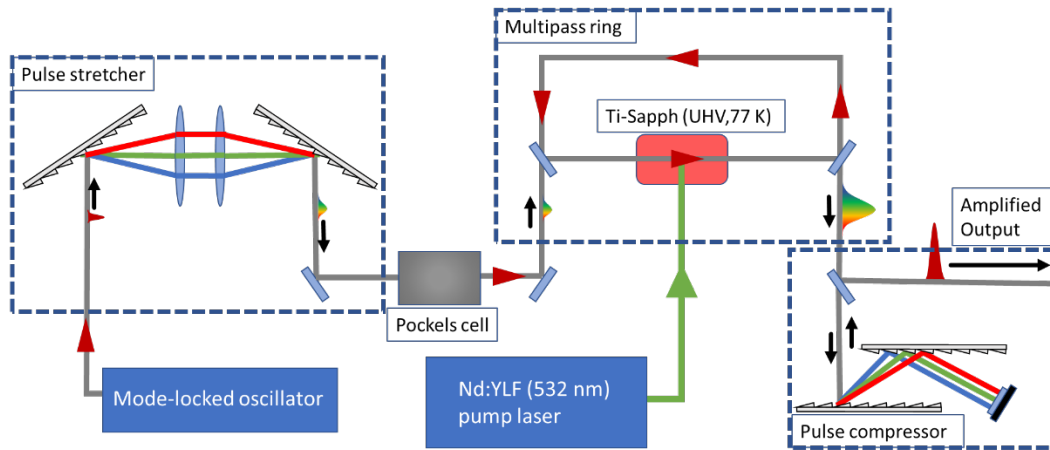


Figure 2.5: Schematic of a multipass chirped pulse amplifier.

The ultrafast pulses from the amplifier are centered around 780 nm and have a bandwidth of about 40 nm. Frequency doubling of the gives us access to an ultrafast laser beam with a central wavelength of  $\sim 400$  nm. In order to extend the range of wavelengths that we can use in experiments, we use an Optical Parametric Amplifier (OPA). We have two-stage, non-collinear OPA in our lab. In the first stage, the 780-nm pump light from the amplifier is split into three portions. One portion of it is used to generate a white light continuum seed, which is non-linearly mixed with the second portion of the pump to generate a signal and idler beam in the mid-IR wavelength range. The signal is then amplified in the second stage using the third portion of the pump beam. Using

frequency doubling, we can further extend the range of the OPA output into the visible and near-UV. The conversion efficiency depends on the desired wavelength, with the highest conversion efficiency being about 20% at 1500 nm. The pulse width of the OPA output is similar to that of the pump pulse ( $\sim 30$  fs).

### 2.2.3 Frequency Resolved Optical Gating

Since ultrafast pulses are some of the fastest physical processes that can be reliably recreated, it is not possible to use electronic detectors and circuits to measure pulse duration. One way to overcome this problem is to measure it against a time-delayed copy of itself. We use a non-linear crystal like  $\beta$  - barium borate (BBO) to generate the sum frequency pulse of the original pulse and the delayed pulse in a three-wave mixing process. This process is called autocorrelation. The time profile of the second harmonic pulse can be easily measured by scanning the delay stage and measuring the intensity using a photodetector. This is used to estimate the pulse width of the original pulse.

$$I_{SHG}(\tau) \propto \left| \int_{-\infty}^{\infty} E(t)E(t - \tau)dt \right|^2 \quad 2.15$$

There is, however, a drawback with autocorrelation. Autocorrelation does not give us any information about the phase of the pulse. In order to be able to retrieve phase information, we need to take the spectrum of the second harmonic beam at every delay step ( $\tau$ ) i.e., a frequency resolved autocorrelation. The resulting two dimensional data set is called a spectrogram. It can be mathematically described by:

$$S(\omega, \tau) \propto \left| \int_{-\infty}^{\infty} E(t)E(t - \tau)e^{-i\omega t} dt \right|^2 \quad 2.16$$

This technique is called Frequency Resolved Optical Gating or FROG. The experimental setup for a FROG measurement is shown in *Figure 2.6* (a) and a typical spectrogram of an ultrafast pulse is shown in Fig. 2.6 (b). The algorithm to retrieve the magnitude and phase of the electric field from the spectrogram is called the Principle Components Generalized Projections algorithm<sup>4,5</sup>. Fig. 2.6(c) shows the electric field reconstructed using commercial FROG software.

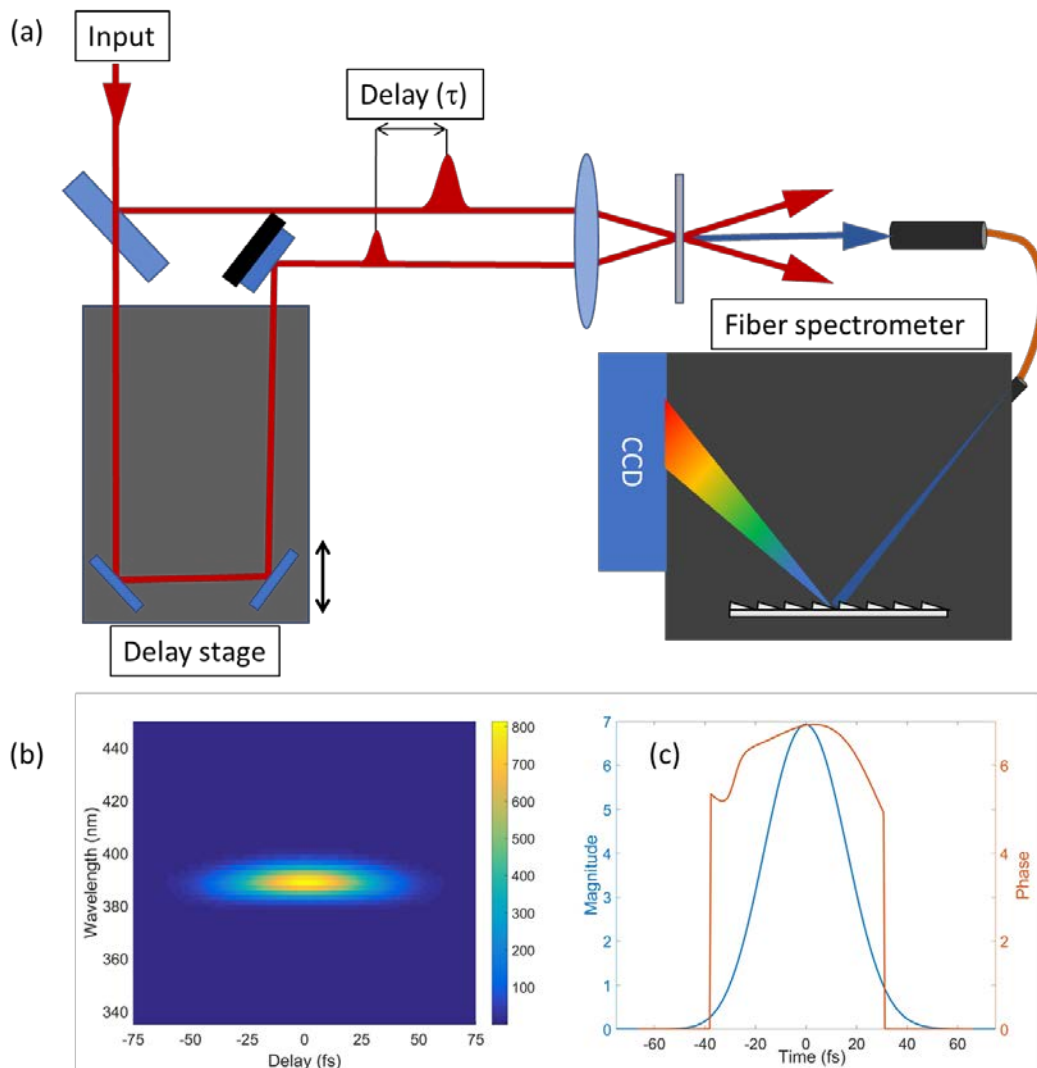


Figure 2.6: (a) Experimental setup for a FROG scan. (b) Spectrogram of a 40 fs pulse. (c) Reconstructed electric field intensity (blue) and phase of the same pulse as in (b) showing a quadratic phase (red).

## 2.3 Pump-probe spectroscopy

With the ultrafast pulses at our disposal, we can perform experiments to measure the timescales of various optical and electronic processes in materials, atoms and molecules. Time-resolved experiments are typically performed in a pump-probe geometry.

Wavelength tunable ultrafast pulse trains from the OPA, the 780 nm beam from the amplifier and the second harmonic at 395 nm can be sent into either the pump arm or the probe arm of the experiment to obtain a spectrally resolved time domain measurement of material properties. The basic principle behind pump-probe spectroscopy of a typical semiconductor is quite simple. A pump pulse promotes charge carriers (electrons and holes) into the conduction and valence bands. The fluence of the pump determines the number of charge carriers excited. Typically, the timescale of the excitation process is of the same order of magnitude as the pulse width. Upon excitation, the energy is redistributed inside the material via various relaxation mechanisms. The reflection or transmission of a time delayed probe pulse is used to probe the state of the material at a fixed time delay. By scanning the time delay using a delay stage, we can obtain the relaxation dynamics of the material. Since the probe must not cause any material property changes of its own, the intensity of the probe pulse must be much smaller than the pump pulse. By adjusting the spot size of the probe to be much smaller than the spot size of the pump, we ensure that the probe samples a uniform spatial carrier distribution. *Figure 2.7* shows the typical setup of a pump-probe experiment.

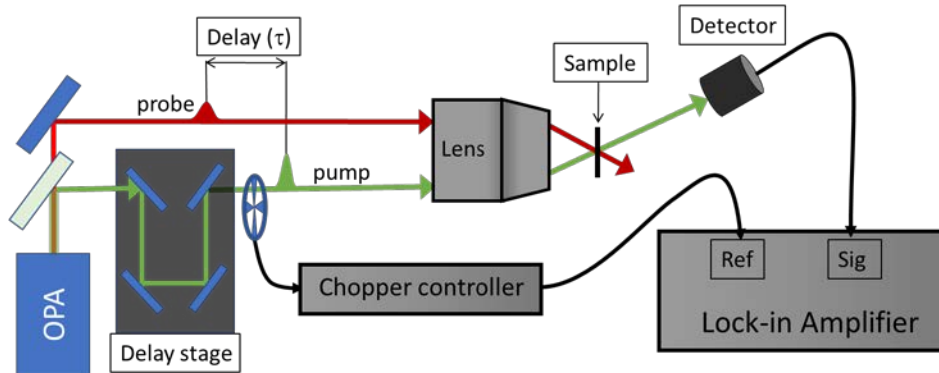


Figure 2.7: Schematic representation of a pump-probe experiment in the transmission geometry.

Since the pump-induced reflection or transmission changes can be smaller than 0.1%, and the laser intensity fluctuates as much as 2%, we need to increase the signal to noise ratio. We use a chopper to modulate the intensity of the pump beam at a fixed frequency  $f_{ch}$ . The transmission or reflection of the probe which is monitored on a fast silicon photodiode, is fed into a lock-in amplifier's input. The reference frequency of the lock-in amplifier is connected to the chopping frequency signal from the chopper. The output of the lock-in amplifier is windowed around  $f_{ch}$ , with a bandwidth that is determined by the integration time scale of the lock-in. Effectively, the output of the lock-in amplifier measures only the pump-induced changes in the reflection (or transmission) of the probe. This scheme increases the SNR by a factor of 1000 and makes it possible to measure fractional changes in optical properties as small as  $10^{-4}$ .

Using the tools and methods describe in this chapter, I have performed time resolved experiments to probe the optical properties of select 2D materials and heterostructures that are of current interest (2012-2017).

# CHAPTER 3.

## Optical Properties and Spectroscopy of Graphene

Although the theoretical existence of graphene has been known for a long time, graphene was first isolated from graphite in 2004<sup>6</sup> by Andre Geim and Kostya Novoselev at the University of Manchester. They received the Nobel prize in 2010 for their breakthrough discovery. Since then, there has been a barrage of research in every aspect of graphene physics. The deceptively simple “Scotch tape method” made graphene isolation simple and accessible to many research groups around the world. Optical and electronic devices manufactured using graphene as the active material have shown high functionality coupled with mechanical characteristics such as flexibility and strength. Graphene’s high electrical conductivity ( $1,000 - 20,000 \text{ cm}^2 \text{ V}^{-1} \text{ s}^{-1}$ )<sup>7,8</sup> coupled with high thermal conductivity ( $5000 \text{ W} \cdot \text{m}^{-1} \cdot \text{K}^{-1}$ )<sup>9</sup> make it an ideal candidate for opto-electronic devices such as photodetectors<sup>10</sup>, saturable absorbers<sup>11</sup>, photovoltaic cells<sup>12</sup>, photonic crystals<sup>13</sup>, field effect transistors<sup>14</sup>, transparent conductors<sup>15</sup> and even loudspeakers<sup>16</sup>.

### 3.1 Electronic properties

Graphene is a two-dimensional sheet of carbon atoms in a hexagonal lattice as shown in *Figure 3.1*. Graphite which is a well-

known material used in many applications consists of graphene sheets stacked on each other in a crystallographic alignment. The carbon atoms in a sheet of graphene are  $sp^2$  hybridized which involves one  $s$  and two  $p$  orbitals resulting in a trigonal planar structure with a  $\sigma$  bond connecting any two carbon atoms. This leaves a  $p$  orbital on each carbon atom perpendicular to the graphene plane which forms half-filled  $\pi$  bonds with neighboring carbon atoms. The strong  $\sigma$  bonds are the reason graphene is structurally robust for a single layer of atoms. The non-locality of the  $\pi$  bonded electrons results in the high electrical and thermal conductivity of graphene.

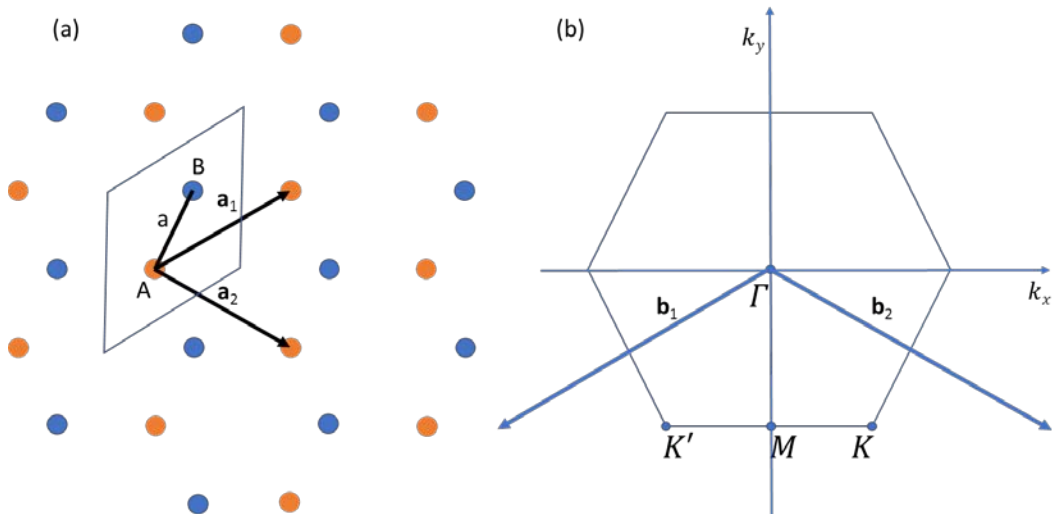


Figure 3.1: (a) Hexagonal crystal structure of graphene showing the unit cell (parallelogram) (b) First Brillouin zone in reciprocal space showing important points and reciprocal lattice vectors

The repeating unit cell of graphene is a parallelogram as shown in Fig. 3.1(a). The crystal lattice consists of two carbon atoms (A, B), which are set in a triangular lattice interlocked with each other to form the hexagonal graphene lattice. Neighbouring carbon atoms in graphene

are separated by  $a = 1.43 \text{ \AA}$ . The primitive lattice vectors in the real space are

$$\mathbf{a}_1 = \frac{a}{2}(3, \sqrt{3}), \quad \mathbf{a}_2 = \frac{a}{2}(3, -\sqrt{3}) \quad 3.1$$

The reciprocal lattice vectors are

$$\mathbf{b}_1 = \frac{2\pi}{3a}(1, \sqrt{3}), \quad \mathbf{b}_2 = \frac{2\pi}{3a}(1, -\sqrt{3}) \quad 3.2$$

The important points in the first Brillouin zone are marked in *Figure 3.1* (b). The K-points are of particular interest as the fermi surface of graphene passes through these points. We use a tight binding approach<sup>7</sup> to describe the electronic properties of graphene. The tight binding model assumes that the electrons can hop from one carbon atom to the nearest carbon atom and next to nearest carbon atom. The energy expense for an electron to hop to the nearest atom is  $t = 2.8\text{eV}$  and to the next to nearest atom is  $t' = 0.56\text{eV}$ . The Hamiltonian for the system can be written in the second quantization scheme as:

$$H = -t \sum_{\langle i,j \rangle, s} (a_{s,i}^\dagger b_{s,j} + H.C.) - t' \sum_{\langle\langle i,j \rangle\rangle, s} (a_{s,i}^\dagger a_{s,j} + b_{s,i}^\dagger b_{s,j} + H.C.) \quad 3.3$$

Here,  $s$  denotes the spin of the electrons which can be up ( $\uparrow$ ) or down ( $\downarrow$ ) and  $i, j$  denote the lattice sites where  $\langle i, j \rangle$  denotes summation over neighboring carbon atoms and  $\langle\langle i, j \rangle\rangle$  denotes summation over next to nearest carbon atoms. The operators  $a, a^\dagger$  and  $b, b^\dagger$  denote creation and annihilation operators for electrons on the A and B lattice sites. Diagonalizing the above hamiltonian, we can solve for the energy dispersion of the electrons. If  $\bar{\mathbf{k}} = (k_x, k_y)$  denotes the momentum vector in the first Brillouin zone, the dispersion relation is

$$E(k) = \pm t\sqrt{3 + f(k)} - t' \cdot f(k) \quad 3.4$$

$$f(k) = 2 \cos \sqrt{3} k_y a + 4 \cos \left( \frac{\sqrt{3}}{2} k_y a \right) \cos \left( \frac{3}{2} k_x a \right) \quad 3.5$$

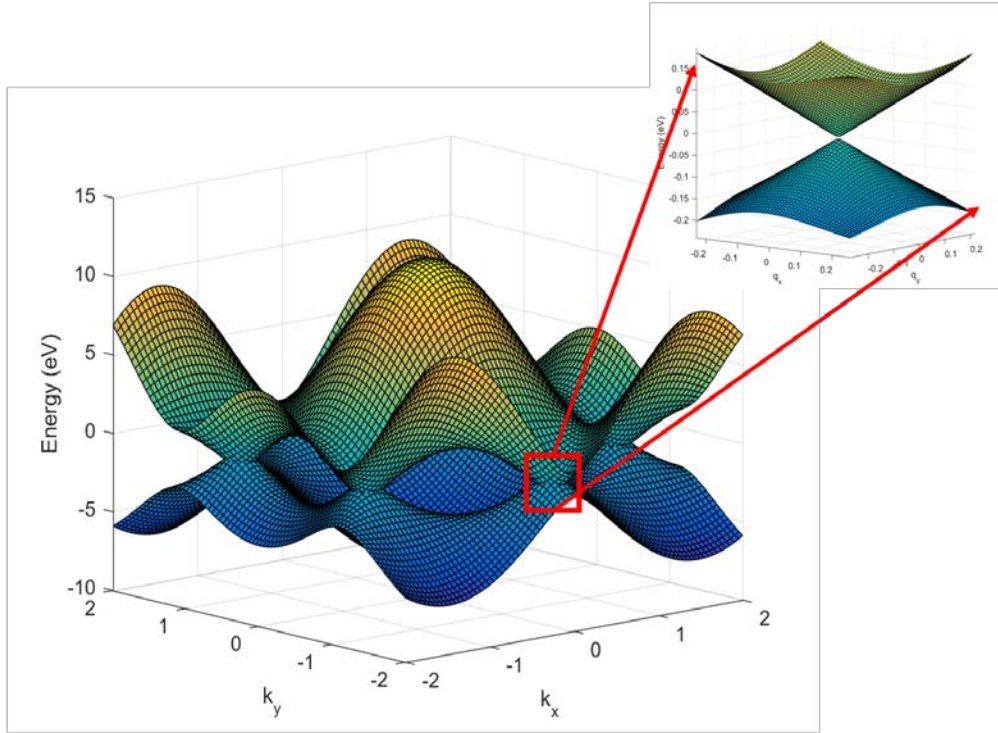


Figure 3.2: Electronic bandstructure of graphene. Inset: Close up near Dirac point showing linear dispersion.

The two bands seen Fig. 3.2 are the conduction band ( $\pi$ ) and lower valence band ( $\pi^*$ ). The Fermi surface passes through the K-points, which is also where the conduction and valence band meet. This makes graphene a zero bandgap material; i.e., a semi-metal. For low energy optical or electronic excitations, we can deduce the dynamics by expanding the dispersion about the K-point momentum as  $\mathbf{k} = \mathbf{K} + \mathbf{q}$  where the K-point momentum vector is  $\mathbf{K} = \left( \frac{2\pi}{3a}, \frac{2\pi}{3\sqrt{3}a} \right)$  and  $|\mathbf{q}| \ll |\mathbf{K}|$  is the momentum relative to the K-point. Such an expansion gives us a linear dispersion relation near the Dirac point.

$$E_{\pm}(\mathbf{q}) = \pm v_f |\mathbf{q}| \quad 3.6$$

Here, the constant  $v_f \approx 1 \times 10^6 \frac{m}{s}$  is called the fermi velocity. The inset to *Figure 3.2* shows the linear dispersion close to the Dirac point. The linear dispersion relation implies that the charge carriers in the conduction and valence bands are massless. The carriers near the Dirac point are usually referred to as Dirac fermions since they can be describes using the massless Dirac equation. The opportunity to study relativitic effects in a laboratory setting is one of the prime reasons graphene research attracts a lot of attention.

## 3.2 CVD growth procedure

The easiest (and the earliest) method to isolate graphene is the “scotch tape method” where chunks of HOPG (Highly Oriented Pyrolytic Graphite) is stuck to a piece of low residue scotch tape and repeatedly exfoliated to reduce the average flake thickness. After sufficient iterations, the thinned and reduced flakes are deposited on a Si/SiO<sub>2</sub> chip. This last step is vital for optical identification of monolayer graphene due to thin film interference as we will see in the next section. This procedure produces a few high-quality, albeit tiny, graphene flakes on some Si/SiO<sub>2</sub> chips. To get larger graphene flakes we use a low pressure chemical vapor deposition (CVD) technique. This technique was used to make most the samples that were used in the studies described in this dissertation. The actual procedure has evolved and changed over many years but the basic steps follow the recipe by X. Li et al<sup>17</sup>. The steps below represent one particular recipe for graphene growth.

1. Cut a flat piece of 25 $\mu$ m thick copper foil and clean it by sonicating the foil in acetone for 20 minutes followed by rinsing with methanol. Then immerse it in a 20:1 solution of DI water:HCl. Rinse off with DI water and dry it off using compressed nitrogen.
2. Make a small enclosure (pouch) out of the copper foil by folding it along its length and crimping the edges.
3. Place the foil in the tube and insert it into the furnace.
4. Anneal the copper at 1010°C for 20 minutes.
5. Flow methane and hydrogen gas at 1 SCCM and 2 SCCM respectively keeping the temperature at 1035°C for 120 minutes and shut off gas flow and turn the heating coil off.
6. When the pouch comes to room temperature, remove it from the furnace. Open the pouch up and keep track of which side corresponds to the inside as we are only interested on the growth inside the pouch. Graphene grows on both sides of the pouch.
7. Spin coat PMMA onto the copper foil. Keep the PMMA confined to the side which has the graphene of interest.
8. Float the foil with the PMMA facing up in a solution of 1:1:10 HCl:H<sub>2</sub>O<sub>2</sub>:DI water until the copper dissolves away. This usually takes up to 12 hours.
9. Rinse very gently with DI water.
10. Using the desired substrate, pick off the PMMA/graphene structure gently and use compressed nitrogen to push the film flat onto the substrate.
11. Bake the PMMA/graphene/substrate stack at 130°C for about 30 minutes to soften the PMMA.

12. Use acetone to dissolve the PMMA leaving the graphene on the substrate.
13. Clean the sample with methanol and dry it with compressed nitrogen.

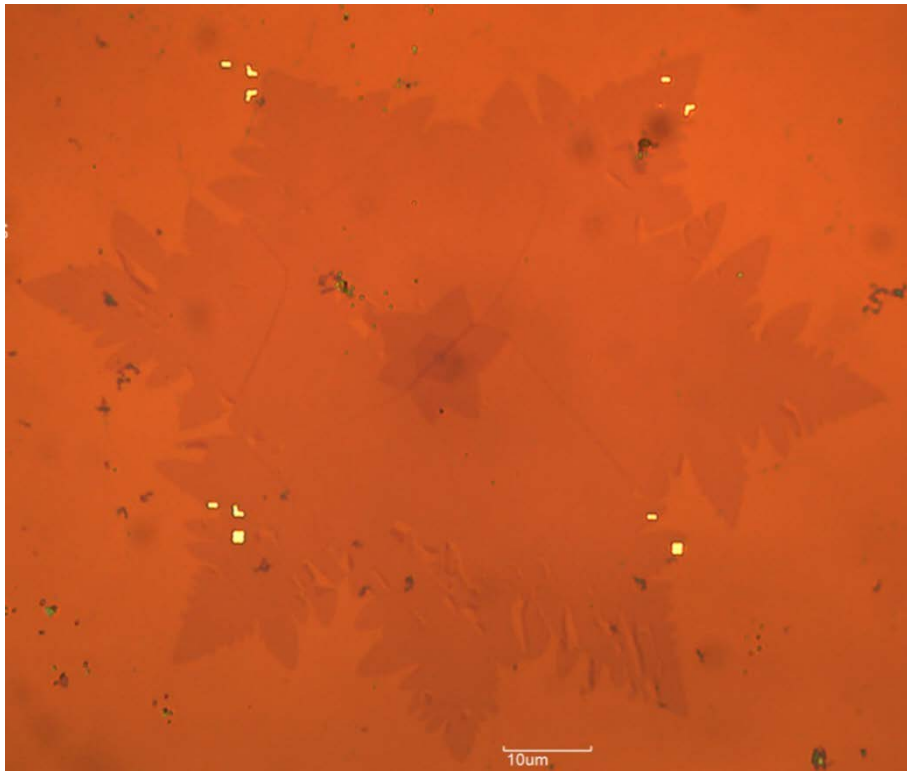


Figure 3.3: Typical CVD grown graphene flake showing petal like six-fold symmetry with multilayers in the center

The above growth procedure results in graphene flakes with a large domain size with a six-fold symmetry as seen in Fig. 3.3. Since graphene has no bandgap, it interacts very strongly with light of any wavelength. To enable optical identification of monolayer graphene, it is deposited on an oxidized silicon chip with a carefully chosen oxidation layer width. Thin film interference in the layered structure results in

strong contrast of the graphene over the background for some wavelengths, enabling us to identify monolayer graphene. The thickness of SiO<sub>2</sub> used by most groups is about 290nm which provides maximum contrast at about 550nm<sup>18</sup>. Even a 5% change in the thickness of the oxide layer can significantly lower the contrast.

### 3.3 Raman Spectroscopy of Graphene

Although simple optical imaging is sufficient to identify monolayer graphene or to identify the thickness of multilayer graphene, Raman spectroscopy is a reliable test for the quality of graphene. Pristine monolayer graphene has a well characterized Raman spectroscopy signature<sup>19</sup>. Graphene interacts strongly with light in the visible and IR wavelengths, making Raman spectroscopy an indispensable tool in graphene characterization. The energy diagram of a Raman scattering process is shown in Fig. 3.4. A photon excites an electron from its ground state to a virtual state before relaxing to a new state that is either higher (Stokes scattering) or lower (anti-Stokes scattering) in energy compared to the initial ground state. The energy of the photon absorbed is denoted as  $\hbar\omega_i$  and the energy of the emitted photon as  $\hbar\omega_s$ . The differential energy between the initial and final states of the electron,  $\hbar\Omega$ , is taken away by or given to the lattice in the form of absorption or emission of a phonon. The scattering cross section of Raman processes is typically very small and most of the exciting photons are elastically scattered in a process called Rayleigh scattering. Rayleigh scattered light is the same wavelength as the exciting light and contains no information about the phonons in the system. The Raman

scattered light intensity is proportional to the square of the polarizability tensor of the material given by

$$\alpha \propto \sum_I \frac{\langle F|\hat{r}|I\rangle\langle I|\hat{r}|G\rangle}{\hbar\omega_{GI} - \hbar\omega_i - i\Gamma} \quad 3.5$$

G, I and F are the ground, intermediate, and final states of the transition. The energy difference between ground (G) and real intermediate (I) states is  $\hbar\omega_{GI}$  and  $\hbar\omega_i$  is the energy of the incoming photon.  $\Gamma$  denotes the damping in the oscillation between the G and I states. From the expression for the polarizability, we see that the polarizability tensor diverges when  $\omega_{GI} = \omega_i$ . In other words, if the incoming photon excites the electron to a real state, then the scattering cross section is much higher and the process is called Resonance Raman Scattering.

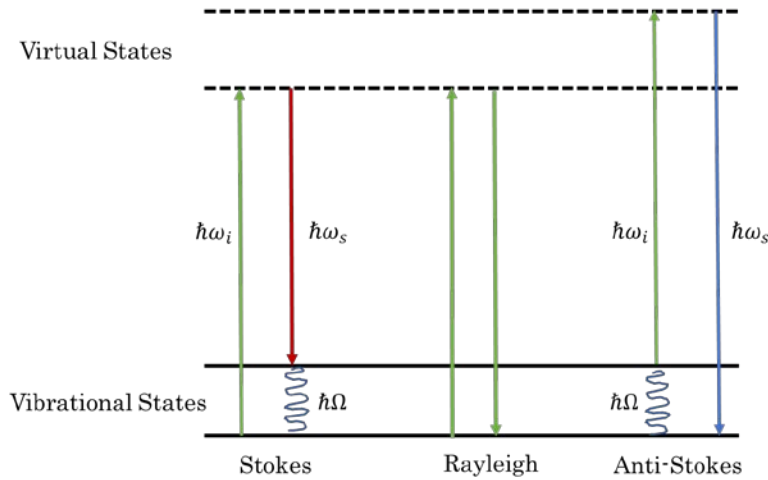


Figure 3.4: Energy diagram of a Raman process showing Stokes, Rayleigh and Anti-Stokes scattering processes

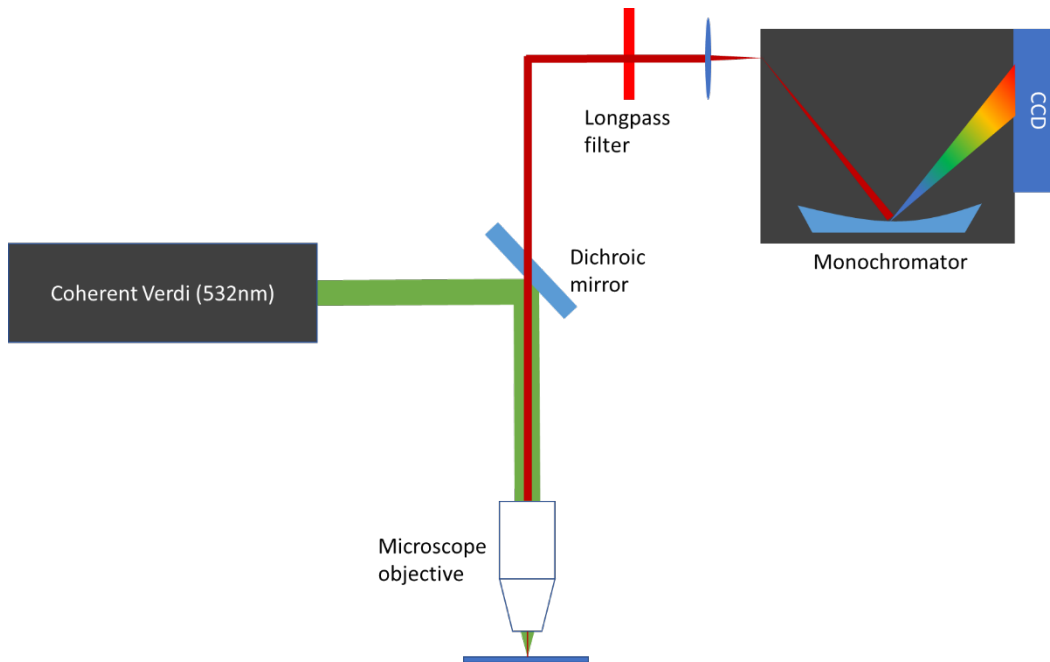


Figure 3.5: Typical experimental setup for Raman spectroscopy.

A basic schematic of the Raman spectroscopy setup in our lab is shown in Fig. 3.5. The exciting laser is a Coherent Verdi laser (which also pumps our ultrafast oscillator) with a narrow linewidth centered at 532nm. The green light is incident on the sample after passing through a microscope objective. The spot size is about  $2\mu m$ . The intensity of the exciting laser is kept below  $2 \frac{mW}{\mu m^2}$  to avoid damaged to the sample and heating effects. The reflected light, which includes the Raman and the Rayleigh scattered light, is collected by the objective. The dichroic mirror and longpass filter attenuate the Rayleigh scattered light which would otherwise saturate the detector with background signal. The Raman light is sent into a monochromator. The dispersed Raman lines are recorded using a Peltier cooled CCD.

In the case of graphene, the lack of a bandgap means that photons ranging from IR to UV will be resonant with a real excited state. This is the reason why the Raman cross section of graphene is very high despite it being a single layer of atoms. The work by Ferrari and Basko<sup>19</sup> reviews the physics behind the Raman processes in graphene in excellent detail.

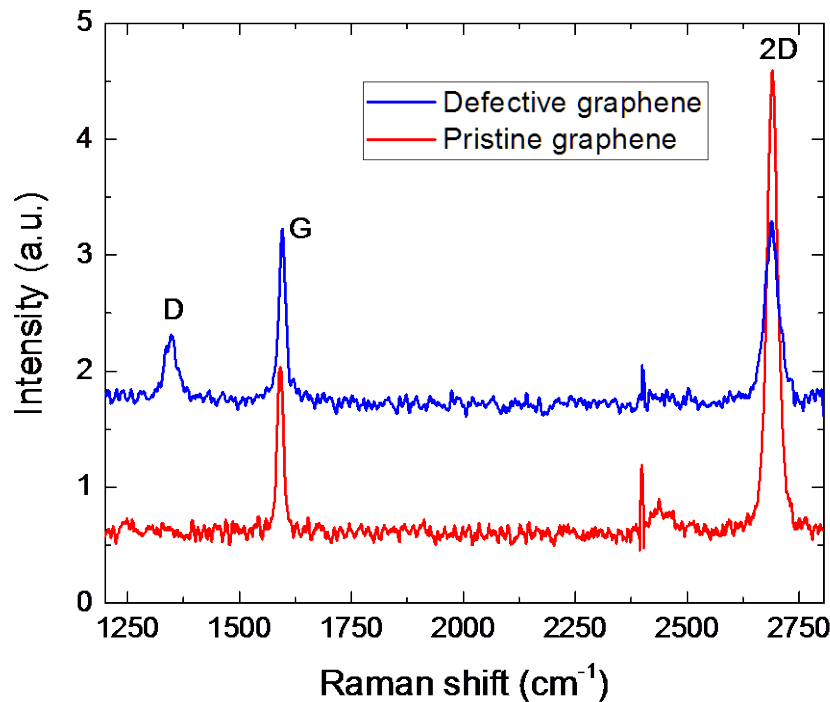


Figure 3.6: Typical Raman spectrum for pristine CVD graphene (red) and graphene with defects (blue)

Typical Raman spectra of pristine (bottom, red) and defective graphene (top, blue) is shown in Fig. 3.6. The curves are offset for clarity. The main features are the G peak at about 1590 cm<sup>-1</sup> and the 2D peak at 2690 cm<sup>-1</sup>. In the case of defective graphene, we see an additional peak, called the D peak at about 1349 cm<sup>-1</sup>. Pristine monolayer graphene

is characterized by a relatively high  $\frac{I_{2D}}{I_G}$  ratio where  $I_{2D}$  and  $I_G$  represent the intensities of the 2D and G Raman lines respectively. The intensity of the G peak scales with number of layers whereas the 2D peak intensity remains approximately constant; this allows us to use the  $\frac{I_{2D}}{I_G}$  ratio as an identifying feature of monolayer graphene. Another differentiating factor in the spectrum of monolayer and multilayer graphene is that the 2D peak of monolayer graphene can be fit with a single Lorentzian profile while the 2D peak of multilayer graphene needs more than one Lorentz curve for a proper fit. For example, the 2D peak of bilayer is a sum of four Lorentzian profiles<sup>19</sup>.

Defective graphene was produced by exposing pristine CVD graphene to ultrafast radiation with a fluence of  $500 \frac{\mu J}{cm^2}$  for one hour. Apart from the D peak, the other features of the Raman spectrum of the defective graphene which differentiate it from pristine graphene are the positions and widths of the G and 2D peak. External factors like doping (either due to gating or oxygen substitution) or stress<sup>20</sup> cause the positions, widths and relative intensity of the G and 2D peak to vary. We observe that upon exposure to ultrafast laser light, the G and 2D peaks blue shift and broaden. The  $\frac{I_{2D}}{I_G}$  ratio also reduces upon exposure to ultrafast radiation. This change in peak shape and position is brought about because exposure to ultrafast radiation increases the number of substitutional defects in the graphene where oxygen atoms replace carbon atoms. This substitution causes p-doping in the exposed graphene sample. The effect of doping on graphene's Raman spectrum

has been studied<sup>21</sup> by applying a vertical gate potential across the graphene layer.

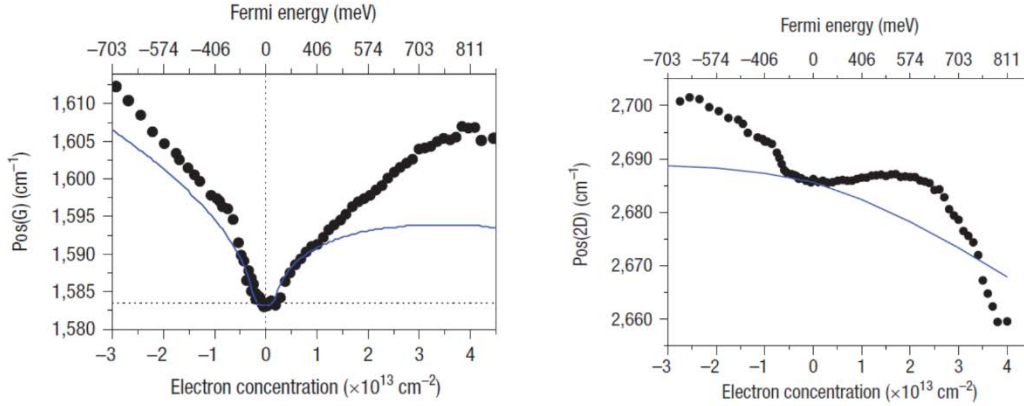


Figure 3.7 : Position of the G peak (left) and the 2D peak (right) as a function of electron and hole doping. Solid lines denote adiabatic DFT calculations. Adapted with permission from Das et al., Nature Nanotechnology, vol. 3, no. 4, pp. 210-215, 2008.

Fig. 3.7 (adapted from Das et al., Nature Nanotechnology, vol. 3, no. 4, pp. 210-215, 2008) shows the relationship between the G peak (left) and 2D peak (right) position depend on the carrier concentration. Using Fig. 3.7 for calibration, we can infer from the peak positions in *Figure 3.6* that the pristine sample is p-doped by about  $0.5 \times 10^{13} \text{ cm}^{-2}$  and the defective sample is p-doped by about  $1 \times 10^{13} \text{ cm}^{-2}$ . The defective graphene (produced by laser damage) is p-doped because of oxygen binding to the dangling carbon bonds. Since oxygen is highly electronegative, it draws electron concentration away from the carbon sheet, rendering it p-doped<sup>22</sup>.

The intensity of the D peak ( $I_D$ ) is a measure of the disorder in graphene. Upon exposure to ultrafast laser radiation, the density of defects in graphene increases, converting graphene to a nano-crystalline carbon, where the average crystalline size is reduced to 2nm<sup>23</sup>. Upon

further exposure, nano-crystalline carbon turns into amorphous carbon. In this state, the  $sp^2$  bond between carbon atoms are broken. The average crystalline size and the intensity of the D-peak in the nano-crystalline phase, are related as follows<sup>23</sup>.

$$\frac{I_D}{I_G} = \frac{C(\lambda)}{L_a} \quad 3.6$$

Here,  $C(\lambda)$  is an excitation wavelength dependent constant. For  $\lambda = 514nm$ ,  $C(\lambda) = 4.4nm^{24}$ .

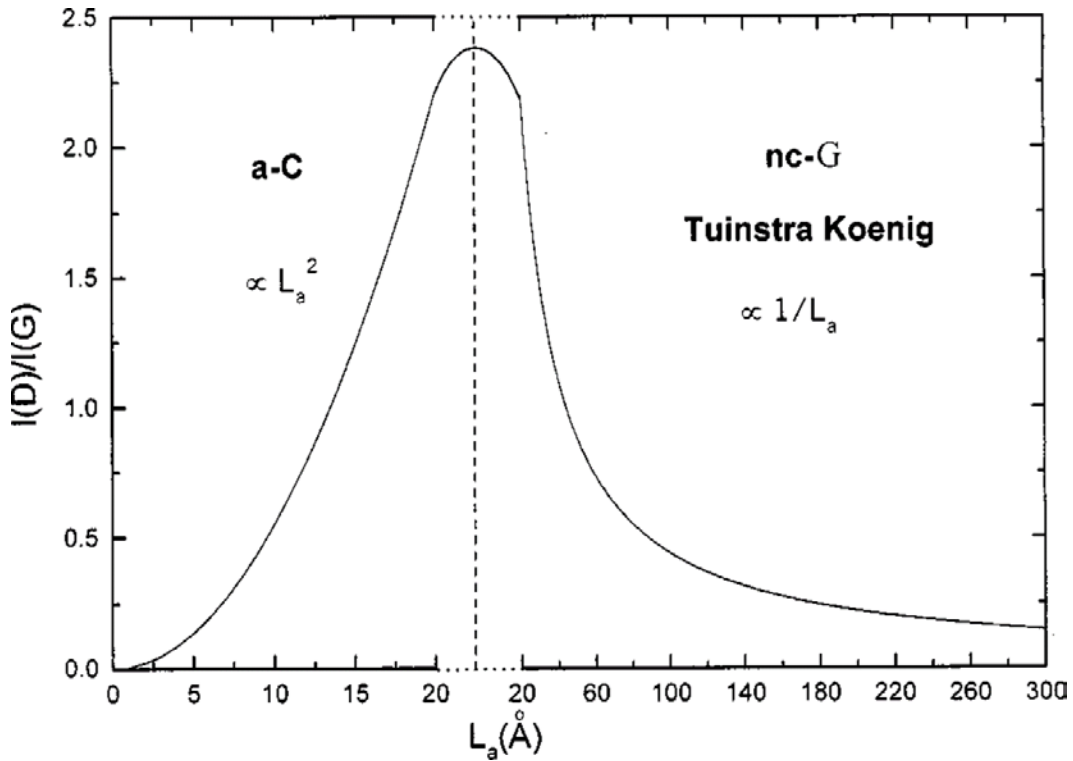


Figure 3.8: Variation of  $\frac{I_D}{I_G}$  ratio with average crystalline size of graphene in the amorphous carbon regime (a-C) and the nano-crystallite graphene regime (nc-G). Figure adapted with permission from Ferrari and Robertson, Physical Review B, Vol 61, number 20, pages 14095-14107 (2000).

Below an average crystalline of 2nm, i.e. in the amorphous phase, the  $\frac{I_D}{I_G}$  ratio drops because D-peak requires approximate lattice periodicity which is absent in the amorphous phase.

Adam Roberts et al<sup>22</sup> studied the response of graphene to femtosecond radiation. Fig. 3.9 shows the variation of the strength of the 2D peak as a function of the number of shots that the graphene is exposed to at various intensities. The results of this study were used as a threshold for laser induced damage on graphene for the ultrafast experiments described in this thesis<sup>33</sup>.

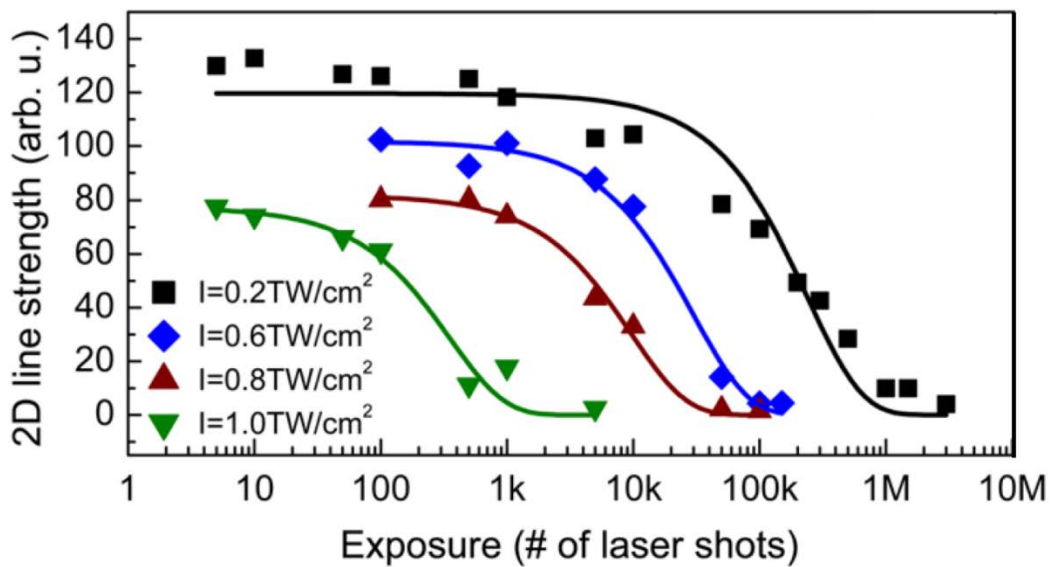


Figure 3.9: 2D line strength as a function of the number of laser exposures. Solid lines are decaying exponential fits. Adapted from “Time Domain Spectroscopy of graphene”, Adam Roberts (2012)

### 3.4 Optical absorption spectrum of graphene

A surprising amount of theoretical research on graphene was done before its isolation in 2004. Researchers could abstract a single

layer of carbon atoms as a single layered sheet of graphite. This honeycomb lattice of carbon atoms was amenable to solid state techniques such as the tight binding model as described in Section 3.1. Tsuneya Ando et al gave the first detailed analysis of light absorption of graphene in 2002<sup>25</sup>. In this section, I will briefly describe some theoretical calculations and experimental results on the optical absorption of graphene.

The response of materials to electromagnetic radiation of frequency  $\omega$  is described by the dynamic optical conductivity,  $\sigma(\omega)$ , of the material. The optical conductivity is related to the dielectric permittivity ( $\varepsilon(\omega)$ ) of the material via the relation:

$$\varepsilon(\omega) = \varepsilon_0 + \frac{i\sigma(\omega)}{\omega} \quad 3.7$$

Here,  $\varepsilon_0$  is the vacuum permittivity. The dielectric permittivity is a linear response function to incident light. It is related to the refractive index of the material via:

$$n(\omega) = \sqrt{\frac{\varepsilon(\omega)}{\varepsilon_0}} \quad 3.8$$

The dynamic conductivity can be calculated via the Kubo formula<sup>25,26</sup>. The optical conductivity has contributions from the intraband and interband optical transitions. Depending on the wavelength of the incident light, either the intra or interband contributions can dominate the optical response of graphene. The interband transitions stem from transitions of the charge carriers within the valence or the conduction band. This type of transition dominates in the low energy (far infrared and terahertz) region of the graphene spectrum. Interband transitions stem from the Drude

scattering of the carriers by the lattice to empty momentum states. At visible and ultraviolet excitations, the major contribution to graphene's response comes from the interband transitions. Here, the photon excites electrons from the valence to the conduction band leaving a hole behind.

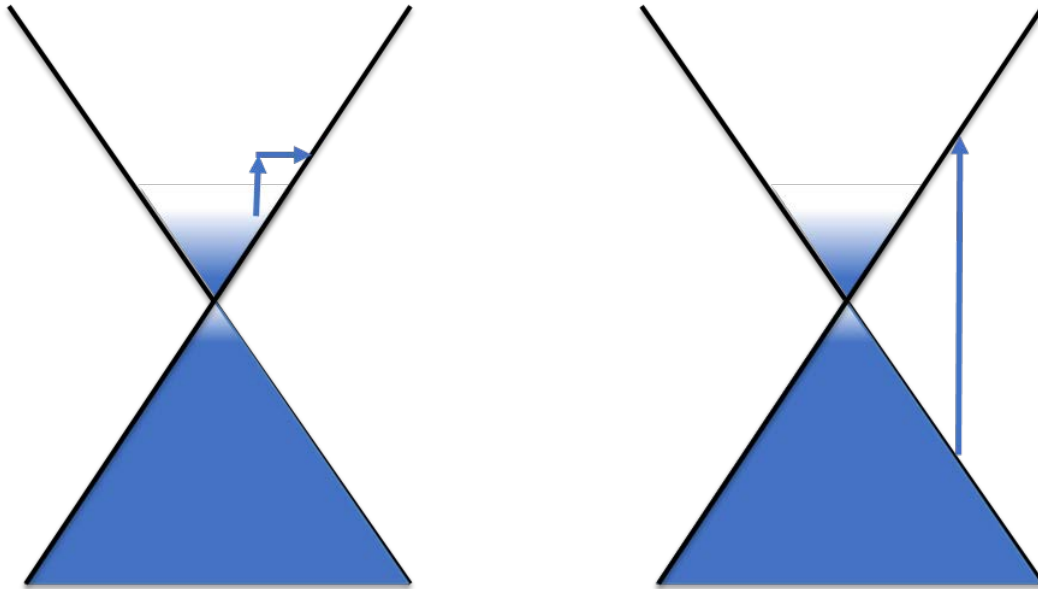


Figure 3.10: (left) interband and (right) intraband electronic transitions responsible for the dynamic conductivity in graphene

Interband transitions are ‘vertical transitions’ (ref. Fig. 3.10) in  $\mathbf{E}-\vec{\mathbf{k}}$  space since the momentum of the incident photon is negligible compared to the momentum of the carrier. In the case of pristine graphene at low temperatures and under the linear dispersion regime, the contribution from interband transitions to the conductivity is constant and independent of incident photon energy<sup>27</sup>. This value is given by:

$$\sigma_0 = \frac{e^2}{4\hbar} \quad 3.9$$

For a thin sheet like graphene, the optical absorption is related to the conductivity via:

$$A = \frac{4\pi}{c} \sigma(\omega) \quad 3.10$$

Thus, the frequency independent conductivity leads to a universal absorption for graphene at low temperatures. Substituting the value for  $\sigma_0$  from Eqn. 3.9 into Eqn. 3.10, we obtain

$$A_0 = \frac{4\pi}{c} \sigma_0 = \pi\alpha \quad 3.11$$

where  $\alpha$  is the fine structure constant. This has been experimentally verified<sup>28,29</sup> over a range of low photon energies. At higher photon energies where the bandstructure deviates from the linear dispersion regime, an increase in absorption is seen<sup>30</sup>. A maximum in the absorption spectrum is seen near 4.6eV. This maximum is associated with transitions from the valence band ( $\pi$ ) to the conduction band ( $\pi^*$ ) near the M-point in the Brillouin zone of graphene. The van Hove singularity in the density of states near the M-point causes a maximum in the absorption spectrum. However, in the independent particle picture, the absorption peak is predicted to occur near 5.2 eV. The red shift in the peak absorption is attributed to the attractive electron-hole interactions<sup>31</sup>.

### 3.5 Multibody effects in graphene

*Note: This section contains material published in the article “Optical Characterization of Electron-Phonon Interactions at the saddle Point in Graphene”, PRL 112, 187401 (2014) by Adam T. Roberts et al*

The previous section described the optical properties of graphene in the independent particle approximation, i.e., neglecting the multibody interactions between the carriers and other quasi-particles in the system. Multibody effects include electron-electron interactions, electron-phonon interactions and excitonic effects<sup>32</sup>. Multibody effects can affect the bandstructure of graphene significantly, especially at high carrier densities. To completely understand the optical and electronic properties of graphene, multibody effects must be considered.

Pump-probe spectroscopy is a powerful tool to study multibody effects as it is sensitive to the bandstructure changes induced by photoexcited carriers. In this section, I will describe ultrafast pump-probe experiments conducted in our lab to study multibody effects in CVD graphene. Although most of the experimental and theoretical work presented in this section were led by Adam Roberts<sup>33</sup>, I verified the degenerate pump-probe measurements with varying pump fluence presented in section 3.5.2 and confirmed our main hypothesis about renormalization due to electron-phonon coupling.

### 3.5.1 Electron-phonon interaction in graphene

Upon photoexcitation over short timescales ( $< 1ps$ ), electron-electron scattering processes dominate the dynamics in graphene due to high electron scattering rates<sup>32,34</sup>. Over longer timescales ( $\gg 1ps$ ) electron-phonon coupling becomes the dominant effect as thermally excited carriers give up excess energy to the lattice<sup>35,36</sup>. The electron-phonon scattering mechanism is of practical importance to the success of graphene electronics as it limits the intrinsic carrier mobility in graphene devices<sup>37-39</sup>.

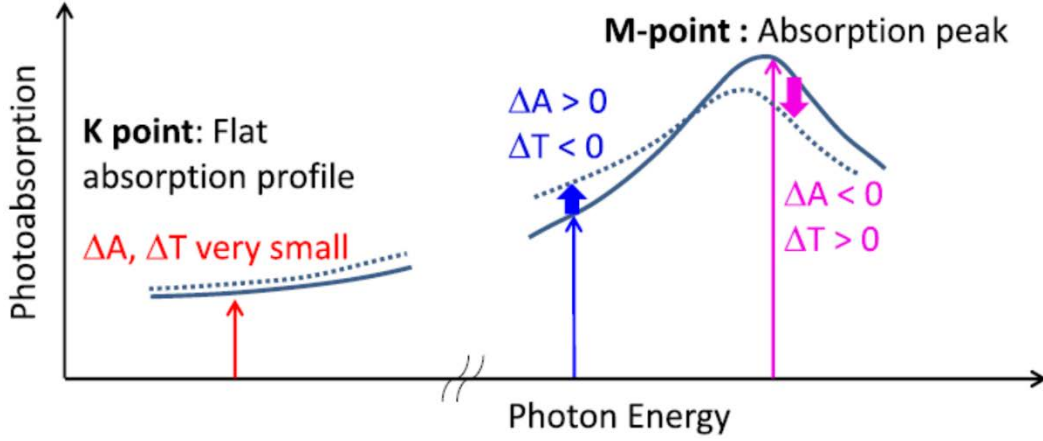


Figure 3.11: Pump induced change in the absorption spectrum of graphene due to electron-phonon renormalization

The electron-acoustic phonon interaction is characterized by the deformation potential,  $D_{eff}^{ac}$ . The estimated values of  $D_{eff}^{ac}$  range from 3 – 50eV<sup>37,40–42</sup>. Since most observables depend on the square of the deformation potential, the range of estimates spans two orders of magnitude. In this experiment, pump induced changes are studied near the M-point at 4.6eV in the bandstructure of graphene. The bandstructure changes due to multibody interactions are stronger at the M-point than at the K- point where the absorption profile is flat (ref. *Figure 3.11*). In this study, we find that for timescales  $\geq 2ps$ , the bandstructure renormalization predicted for electron-acoustic phonon interaction matches the differential absorption spectrum. From our data, we estimate the deformation potential to be  $D_{eff}^{ac} \cong 5eV$ , which is significantly lower than the values obtained through transport measurements but in line with more recent theoretical predictions<sup>42–44</sup>. Since the temperature increase due to the pump pulse (initial phonon temperature  $T_0 \cong 610 K$ ) is smaller than that required to excite optical

phonons ( $\cong 2400 K$ ), we can conclude that the absorption changes are mostly due to the interactions between electrons and acoustic phonons.

### 3.5.2 Pump-probe spectroscopy of graphene

In a pump-probe experiment, a pump pulse excites carriers in the sample. A time delayed probe pulse, which is much less intense compared to the pump pulse, is incident on the sample at a fixed time delay. The transmission or reflection of the probe pulse is dependent on the evolving state of the system due to the pump pulse. By monitoring the transient transmission or reflection changes, it is possible to extract a time domain picture of the carrier dynamics in the system.

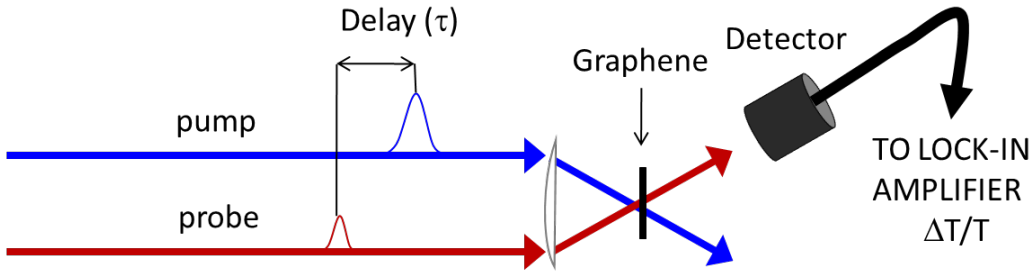


Figure 3.12: The above figure shows a schematic of the pump probe setup in a transmission geometry.

The normalized differential transmission ( $\frac{\Delta T}{T_0}$ ) of a ten-layer stack of monolayer graphene at three different photon energies is shown in *Figure 3.13*. These measurements were degenerate in pump and probe energy ( $\hbar\omega_{pu} = \hbar\omega_{pr}$ ). The pump fluences excite carriers to densities in the  $10^{12} - 10^{13} cm^{-2}$  range.

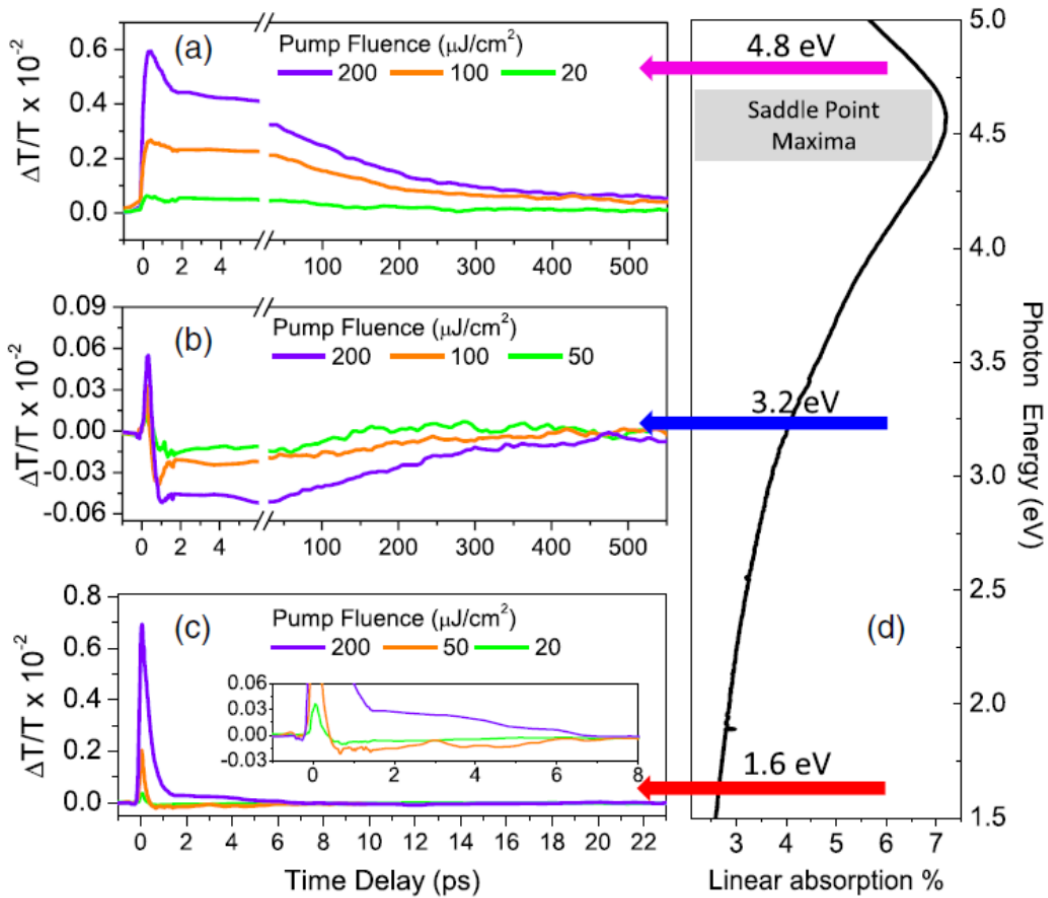


Figure 3.13:  $\frac{\Delta T}{T_0}$  value of the probe pulse at pump-probe energies of (a) 4.8 eV, (b) 3.2 eV, and (c) 1.6 eV. (d) The linear absorption profile indicating the probing energies relative to the saddle point absorption maxima.

Fig. 3.13 (a), (b) and (c) show the differential transmission, (note that  $\Delta T = 1 - \Delta A$ , where  $\Delta A$  is the change in absorption) for excitation at 4.8eV, 3.2eV and 1.6eV respectively. In all cases, there is a strong increase in absorption at small time delays when the pump and probe nearly overlap. This peak near the zero-time delay is due to Pauli blocking of probe absorption due to the pump induced electrons (holes) in the conduction (valence) bands. This transient increase in

transmission lasts a few hundred femtoseconds and relaxes due to carrier-carrier interactions and carrier-phonon interactions<sup>32,34,45</sup>. After 2ps, for 3.2 eV and 4.8 eV excitations, the signal shows a slow relaxation to the baseline. The sign of the  $\frac{\Delta T}{T_0}$  signal is opposite in these two cases. In the case of 4.8 eV excitation, the signal shows a strong positive trend whereas, the signal is negative for the 3.2 eV excitation. The negative signal indicates stronger absorption for the pump excited graphene compared to unexcited graphene. The opposite is true for 4.8 eV excitation which shows decreased absorption. This change lasts for the same duration in both cases ( $\sim 300ps$ ) which suggests a common origin for the effect despite opposite signs. As seen in *Figure 3.11*, this common cause is bandgap renormalization due to electron-phonon interactions. For 1.6 eV photons, a very weak  $\frac{\Delta T}{T_0}$  signal is seen beyond 2 ps. In the near-infrared region ( $\sim 1.6$  eV), graphene has a flat absorption profile and the absorption is unaffected by bandgap renormalization. In contrast, at higher photon energies, the absorption features (ref. *Figure 3.13* (d)) are very sensitive to bandgap renormalization and serve to quantify the electron-phonon interaction effects.

### 3.5.3 Bandgap renormalization in graphene

To obtain the line shape of the  $\frac{\Delta T}{T_0}$  spectrum, we can fix the pump photon energy at 4.8 eV and vary the probe photon energy around the saddle point (M-point) transition. The result of this measurement is shown in *Figure 3.14* (black squares) for time delays of 4, 40 and 400 ps. The initial temperature of the phonon system is estimated by assuming that within a short time ( $< 2ps$ ), the photoexcited carriers relax and the

energy of the laser pulse is deposited into the phonon system. The estimated initial energy in the case of the highest fluence used is  $\mathcal{T}_0 = 610 \text{ K}$ . The temperature will decrease as the phonons decay and transfer energy to the substrate. The  $\frac{\Delta T}{T_0}$  signal at 4.8 eV is proportional to the phonon temperature when the electron-phonon coupling dominates (at time delay  $> 2 \text{ ps}$ ). Therefore, we can find the temperature profile by fitting the data in *Figure 3.13* (a) with an exponential decay profile. Using this technique, we estimate the temperatures at 4, 40 and 400 ps time delay to be 600, 550 and 350 K respectively.

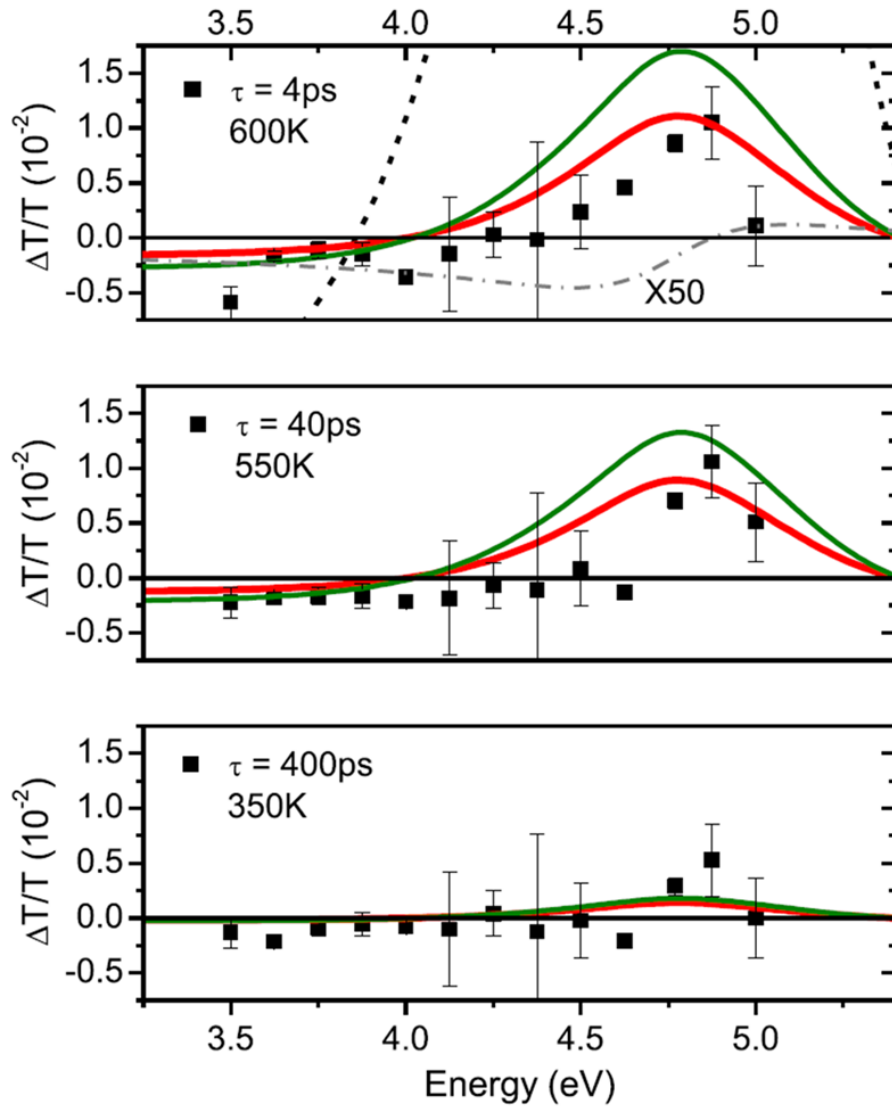


Figure 3.14:  $\frac{\Delta T}{T_0}$  as a function of probe photon energy at three time delays (4, 40 and 400 ps). The pump fluence is  $400 \frac{\mu\text{J}}{\text{cm}^2}$  and fixed pump energy of 4.8 eV. Each panel is labeled with a specific phonon temperature value. The calculated results for coupling to acoustic phonons only with  $D_{eff}^{ac} = 5.3 \text{ eV}$  are shown in red (thick line) and acoustic + optical phonons with  $D_{eff}^{op} = 11 \frac{\text{eV}}{\text{\AA}}$  are shown in green (thin line). The dashed black line (top panel) shows acoustic-only coupling with  $D_{eff}^{ac} = 20 \text{ eV}$ . The dash-dotted gray line (top panel) shows the statically screened Hartree-Fock result for e-e interaction (multiplied by 50 for ease of comparison) using thermally excited carriers.

As mentioned before, the electron-phonon coupling depends on the deformation potential  $D_{eff}^{ac}$ . The line shape can be theoretically modelled considering the electron-acoustic phonon, electron-optical phonon and electron-electron interactions. The results are shown in *Figure 3.14*. The theoretical modelling was done by Rolf Binder, Nai Kwong and Adam Roberts. More details can be found in Ref. 46<sup>46</sup>. The theoretical curves calculated using the value of  $D_{eff}^{ac} = 5 \text{ eV}$  reproduce the line shape and zero crossing very well for all three time delays. We also see from *Figure 3.14* (a) that electron-electron interactions are not significant at longer timescales considered in our model. The model can be further improved by including the fast carrier dynamics occurring in the initial femtosecond timescale and including the role of exciton-phonon coupling.

In this chapter, we dealt with the multi-body effects in intrinsic graphene. To fully realize the potential of graphene and other 2D materials, we need to construct and study 2D heterostructures. In the next chapter, I will describe the electronic properties of graphene-hBN structures and present pump-probe measurements that prove that interaction between the different 2D layers enhances cooling properties of the whole heterostructure.

# CHAPTER 4.

## Ultrafast Dynamics of Graphene Heterostructures

*Note: This chapter contains material published in the following articles:*

1. “Optical thickness determination of hexagonal boron nitride flakes”, *Applied Physics Letters* **102**, 161906 (2013) by Dheeraj Golla et al
2. “Ultrafast relaxation of hot phonons in Graphene-hBN Heterostructures”, *APL Materials* **5**, 056101 (2017) by Dheeraj Golla et al

Hexagonal Boron Nitride (hBN) has a planar hexagonal structure similar to graphite, and has proven to be an excellent substrate for graphene based electronic and optoelectronic devices. Graphene devices on hBN substrates show enhanced performance like increased carrier mobility and reduced charge fluctuations.<sup>47-49</sup> Graphene sheets conform to atomically flat hBN resulting in reduced roughness and charge puddle formation as compared to other common substrates<sup>48</sup> such as Si/SiO<sub>2</sub>. Flakes of hBN have also proven to be an excellent dielectric or tunnel barrier for device applications<sup>50,51</sup>, and can modify graphene’s band structure<sup>52-54</sup>. A large direct bandgap makes hBN attractive for

compact UV laser applications<sup>55</sup>. Interestingly, the success of hBN in graphene electronics is now also being mirrored in the development of other two dimensional materials such as transition metal dichalcogenides (TMD) (e.g., MoS<sub>2</sub>, MoSe<sub>2</sub>, WS<sub>2</sub>, etc.) devices, where hBN substrates have led to 10 times better photoluminescence quantum yields<sup>56</sup> than Si/SiO<sub>2</sub>. hBN is anticipated to be an essential constituent for future graphene and TMD heterostructure devices in many roles ranging from a tunnel barrier to a gate dielectric.

## 4.1 Optical Characterization of the thickness of hBN

Methods for quick, economical, and non-invasive characterization of hBN flakes, specifically, the exact number of hBN monolayers and its flatness over the size of the device are important. In that regards, optical reflection microscopy has proven to be a highly useful tool. Optical contrast measurements have been used to identify mono and few layered graphene on various substrates<sup>18,57</sup>. In this section, I outline a procedure for characterization of thicker (a few to 100 layer) hBN flakes deposited on a SiO<sub>2</sub>/Si substrate. hBN flakes in this thickness range are highly relevant for device applications. For example, it has been shown that hBN substrate thickness of about 10 nm (or about 30 layers) is required for the reduction of surface roughness<sup>47</sup>. Thick hBN flakes also serve to increase the distance from the underlying SiO<sub>2</sub> which reduces the effect of charged impurities (in the oxide layer) on the performance of high mobility devices<sup>51</sup>. I will establish parameters which can enable quick identification for hBN flakes varying from a few to 100 layers. I also show that this approach is sensitive to optical thickness changes as

small as 1–2 layers, allowing the identification of steps in flakes which appear flat under white light illumination.

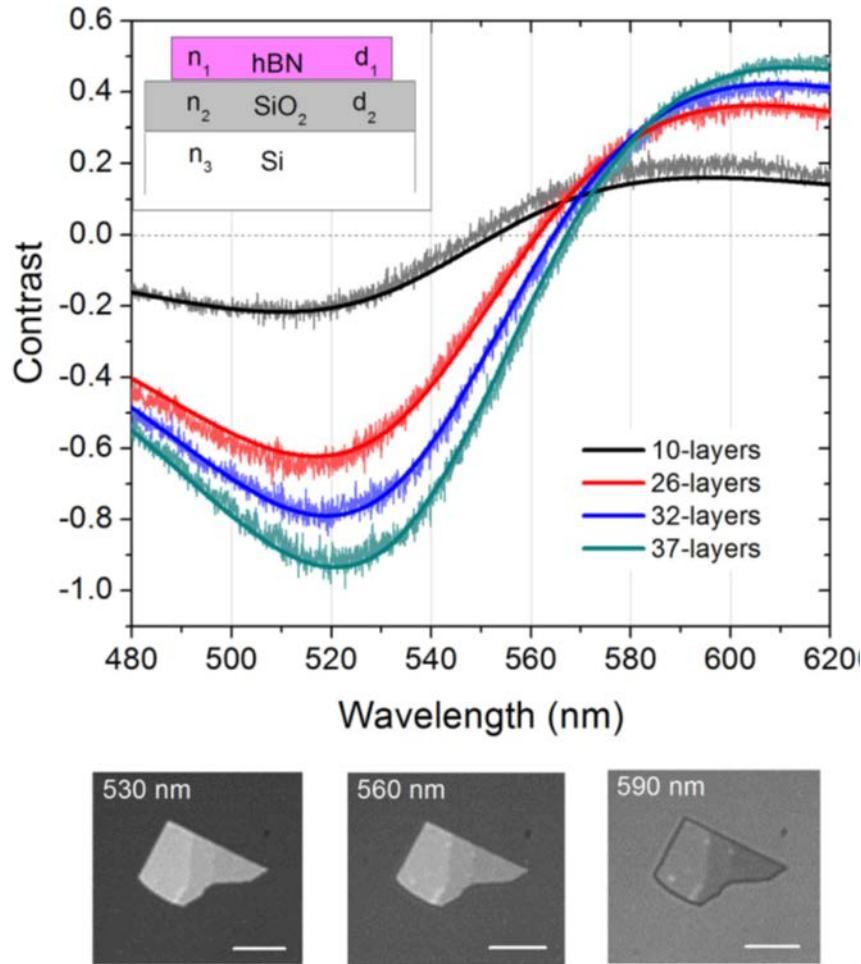


Figure 4.1: The optical contrast of hBN on SiO<sub>2</sub>/Si substrate as a function of the wavelength of light. Different curves correspond to flakes with different number of layers. The dark solid lines are the fits obtained using the multilayer interference calculations. The bottom panels show optical microscope images at three discrete wavelengths corresponding to positive, zero, and negative contrast. The scale bar represents 5  $\mu\text{m}$ .

The sample geometry is shown schematically in the inset of Fig. 4.1. Few layer hBN flakes were prepared by mechanical exfoliation of hBN single crystals on 285 nm SiO<sub>2</sub>/Si substrates. The hBN was grown

using the high pressure method that has been previously described<sup>58</sup>. Using a femtosecond Ti:Sa amplifier and a filamentation setup<sup>59</sup>, we nonlinearly broaden the light pulse spectrum to produce a broadband white light source spanning from 460 nm to 850 nm. White light is incident normally from air on the hBN/SiO<sub>2</sub>/Si structure, and is focused to a small spot size using a 50x, NA = 0.5 microscope objective. The backwards reflected light is collected, and after passing through a beamsplitter, it is imaged on to the entrance slit of a spectrometer. The spectrally resolved reflection signal is obtained using a CCD at the exit aperture of the spectrometer.

The quantity measured in our experiments is the optical contrast in reflectivity of a three-tiered structure, which can be defined as:

$$C = \frac{R_{SiO_2} - R_{hBN+SiO_2}}{R_{SiO_2}} \quad 4.1$$

where  $R_{SiO_2}$  is the reflection coefficient at normal incidence for a bare SiO<sub>2</sub>/Si substrate, and  $R_{hBN+SiO_2}$  is the reflection coefficient of the hBN/SiO<sub>2</sub>/Si stack. The value of  $C$  corresponds to the normalized change in reflectivity of the hBN compared to the substrate. The measured optical contrast is plotted in *Figure 4.1* as a function of wavelength for hBN flakes of varying thicknesses. The thickness of the hBN flakes was determined after optical imaging using atomic force microscopy (AFM). A thickness of 3.33 nm corresponds to 10 layers of hBN because the  $c$ -axis lattice constant of hBN is 0.333 nm. Several observations can be made from these data. The contrast for a given flake can be both positive and negative depending on the wavelength, with a zero crossing in between. A contrast of zero would mean the flake being invisible at that wavelength, i.e., it has the same reflectivity as the substrate. The zero-

contrast wavelength is dependent on the flake thickness, and varies from 550 nm to 570 nm (for 282 nm SiO<sub>2</sub>) as the number of layers increases from a few to tens of layers. The negative contrast is stronger, and its peak is observed between 520 and 530 nm. The positive contrast peaks between 590 and 620 nm. On the bottom panels of *Figure 4.1*, we show three microscope images of a hBN flake taken at selected wavelength bands centered on 530, 560, and 590 nm. Clearly, one can see the flake has greater reflectivity than substrate at 530 nm, i.e., negative contrast, and lesser reflectivity than substrate, i.e., positive contrast at 590 nm. The 560 nm image corresponds to the region near the zero-contrast wavelength. Since the flake has two step edges, three distinct thicknesses can be observed. The sharp tip of the flake is thinnest, and hence closest to zero contrast at 560 nm. In order to model the optical contrast, we use a multilayer interference approach. Essentially, a transfer matrix method<sup>60</sup> is used, where we consider three layers, hBN, SiO<sub>2</sub>, and Si, having refractive indices  $n_1$ ,  $n_2$ , and  $n_3$ , respectively (refer to the inset of *Figure 4.1*). The light is incident from the airside, which implies  $n_0 = 1$ . A recursive relation can be written, in general, for the electric fields at the interface between layers  $j$  and  $j+1$  as:

$$\Gamma_j = \frac{r_j + \Gamma_{j+1}e^{-2ik_jd_j}}{1 + r_j\Gamma_{j+1}e^{-2ik_jd_j}} \quad 4.2$$

where  $d_j$  is the thickness of layer  $j$  and  $\Gamma_j = \frac{E_{j-}}{E_{j+}}$  with  $E_{j-}$  and  $E_{j+}$  representing the backward and forward propagating electric field at the  $j^{\text{th}}$  interface. The reflection coefficient of the  $j^{\text{th}}$  interface is given by  $r_j$ , where:

$$r_j = \frac{n_{j-1} - n_j}{n_{j-1} + n_j} \quad 4.3$$

The wavevector of the light in the  $j^{\text{th}}$  layer is  $k_j = 2\pi \frac{n_j}{\lambda}$ . The thickness of the hBN and SiO<sub>2</sub> are  $d_1$  and  $d_2$ , while the thickness of Si is assumed semi-infinite. The recursion is initiated at the SiO<sub>2</sub>/Si interface by setting  $\Gamma_3 = r_3$ , and then  $\Gamma_2$  and  $\Gamma_1$  are successively calculated to obtain reflectivity of the stack,  $R = |\Gamma_1|^2$ . It is straightforward to generalize this method to a stack with an arbitrary number of interfaces.

The contrast between the region with a hBN flake and the background SiO<sub>2</sub> can then be evaluated by setting the refractive index  $n_1$  of hBN layer equal to 1 (air) and using the formula:

$$C = \frac{R(n_1 = 1) - R(n_1 = n_{hBN})}{R(n_1 = 1)} \quad 4.4$$

The refractive index of hBN is taken to be 1.85 at 560 nm, and a weak linear variation is invoked, leading to a 3% higher (lower) value at 480 (640) nm<sup>61</sup>. Both SiO<sub>2</sub> and the underlying Si have wavelength dependent complex refractive indices<sup>62</sup>. The solids curves in *Figure 4* show the calculated optical contrast for various hBN thicknesses. The thickness of the SiO<sub>2</sub> layer was taken to be 282 nm in all of the calculations, which is within the 285±65 nm value listed by the manufacturer for the thickness of the SiO<sub>2</sub> on the Si wafer. The thickness of the hBN flakes was determined by AFM measurements. The fits to the experimental curves are very good over the entire wavelength range.

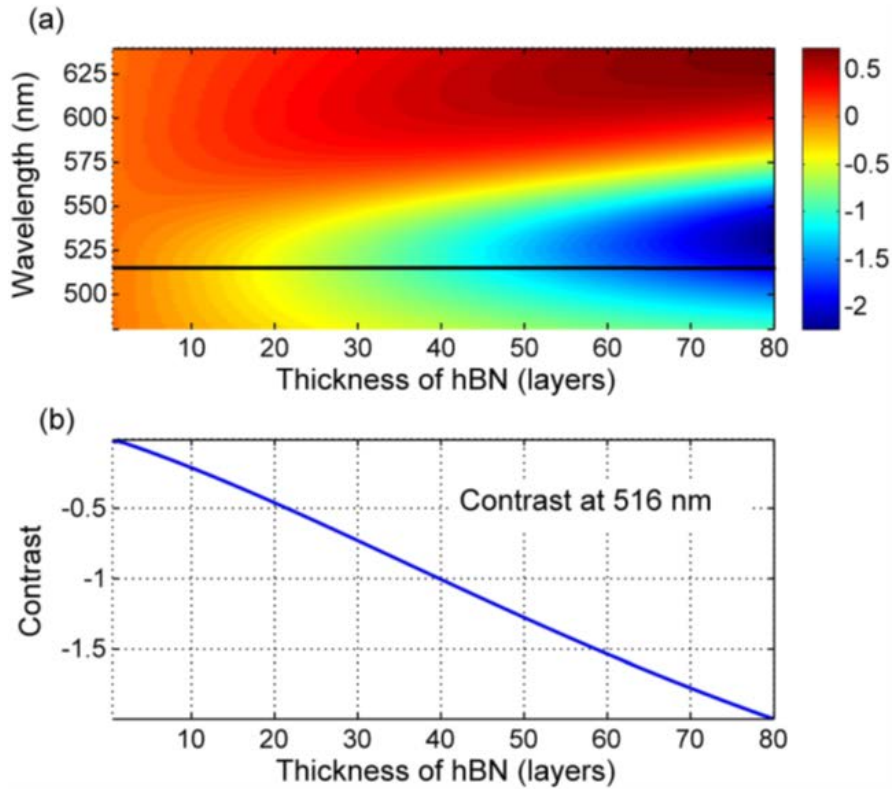


Figure 4.2 : (a) Calculated optical contrast as a function of the wavelength of light and thickness of hBN for a 282nm SiO<sub>2</sub> layer. (b) Line out at 516nm shows that the contrast varies linearly with the thickness of the hBN flake between 1 and 80 layers.

In Fig. 4.2(a), we show the dependence of the optical contrast on the wavelength of light as well as the thickness of the hBN layer for 1–80 layers. This calculation is performed with a 282 nm thick SiO<sub>2</sub> layer to match the experimental data. The negative contrast peak increases rapidly in intensity with the number of layers. In Fig. 4.2(b), we show the variation of contrast at a fixed wavelength of 516 nm, which is near the negative peak. The contrast varies linearly with the thickness of hBN from 1 to 80 layers. This fact implies that contrast observation at a single wavelength can be used for fast and accurate characterization

of the thickness of the hBN flake. In particular, we find that the contrast varies by approximately 2.5% per layer of hBN at this wavelength.

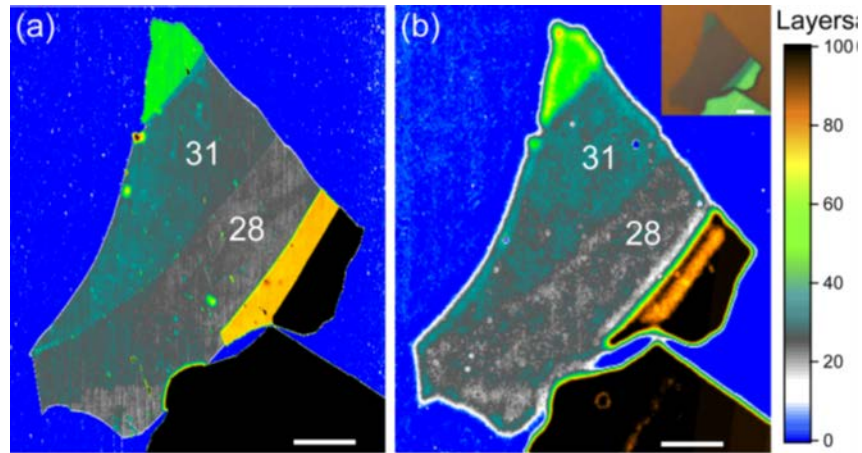


Figure 4.3: The comparison of optical contrast image with the atomic force microscopy image. (a) AFM image of a hBN flake on a  $\text{SiO}_2$  substrate. (b) Optical contrast image of the same hBN flake. The thickness of the two central regions in number of layers is marked on the images. Color bar representing the number of layers is common between the AFM and optical contrast image. The optical contrast values are converted to thickness using 2.5% per layer. Inset shows the microscope image of hBN flake. The length scale bar represents 2 nm in all images. The comparison illustrates the ability of the optical contrast method to measure the thickness of hBN flakes as well as differentiate small steps corresponding to changes in thickness of a few layers of hBN.

Fig. 4.3(a) shows an AFM image of a hBN flake which exhibits many different thicknesses ranging from 28 to 81 layers. Two distinct regions in the center can be discerned. They are separated by a small step of 3 layers. The typical acquisition time for an AFM image with this resolution is on the order of 10 min. In Fig 4.3(b), we show an optical contrast image of the same flake obtained at 516 nm wavelength using an optical microscope. A bandpass filter centered at 516 nm and with a width of 5 nm was placed in front of the microscope light to acquire the image. The resulting image was recorded on a monochrome CCD camera

with an exposure time of 0.25 s. One can clearly observe the 3-monolayer step in the optical contrast image with over a factor of 1000 improvement in the time required for imaging the flake. The wavelength dependence of the contrast exhibits three unique regions, which can be used to calibrate the thickness directly. For a SiO<sub>2</sub> substrate thickness of 282 nm, these regions are 515-530 nm for large negative contrast, 550-570 nm for near zero contrast, and 590-620 nm for positive contrast. The negative contrast varies linearly with the thickness of hBN from 1 to 80 layers. This provides a straightforward thickness calibration using only optical methods.

## 4.2 Transferring Graphene on hBN

The process of transferring graphene onto hBN depends on whether the graphene is CVD grown or exfoliated. Since exfoliated graphene samples are of better crystal quality, they are preferentially used to make devices in which crystal quality and orientation are important. The process for such a transfer uses PMMA or other polymer layers as a carrier for graphene flakes onto hBN flakes, which have been exfoliated onto Si/SiO<sub>2</sub> or any desired substrate<sup>47,63</sup>. A schematic of such a process used to obtain g-hBN on transparent fused silica substrate is shown in *Figure 4.4*.

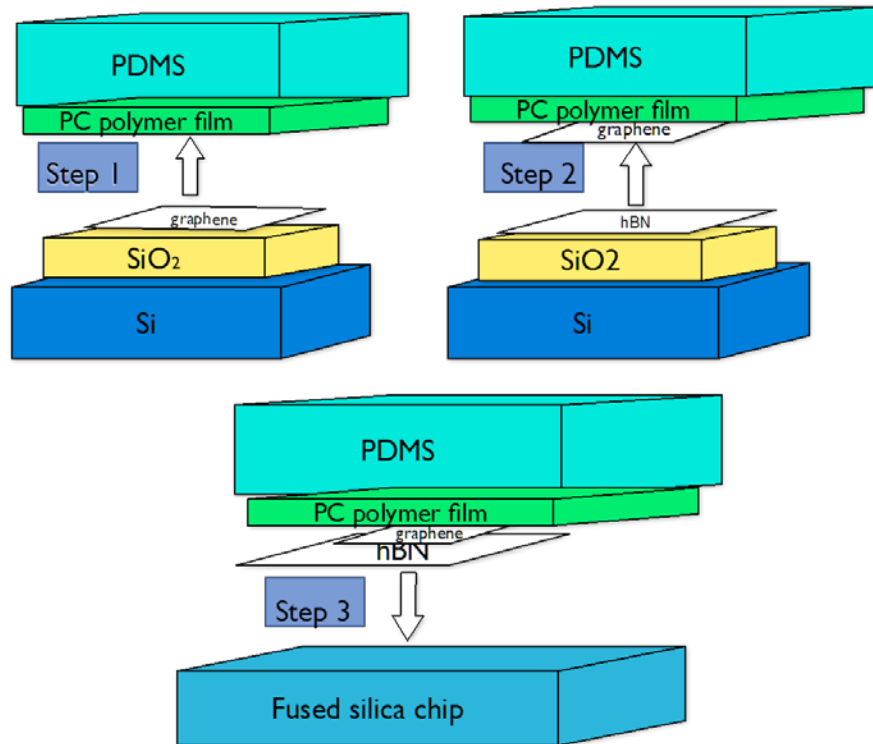


Figure 4.4: Schematic for the steps involved in transferring graphene onto hBN flakes on top of a fused silica substrate.

Since optical probing requires sample sizes of the order of the spot size of the laser ( $\sim 10\mu\text{m}$ ), we transfer CVD grown graphene onto hBN flakes that have been already exfoliated onto SiO<sub>2</sub>/Si chips<sup>64</sup>. The copper sheet on which graphene is grown via the CVD process is cut into 5 mm x 5 mm square sheets. One drop of PMMA-950 is placed on top of this sheet, and then spun at 2000 rev/min for 50 seconds. The PMMA covered sheet is heated to 150 °C for 5 minutes to let the PMMA flow, then cooled to room temperature. To etch the copper, it is placed floating on a mixture of hydrogen peroxide, hydrochloric acid, and DI water in the ratio 0.5:1:9 respectively for 20 minutes. Using a microscope slide, the

PMMA film is then transferred (floating) to a beaker of DI water for 15 minutes. It is transferred again to an additional beaker of DI water for 15 minutes. Pre-prepared exfoliated hBN on SiO<sub>2</sub> samples are cleaned using an acetone/IPA rinse. This substrate is then lowered into the DI water and brought up underneath the PMMA film, so the film sits on top of the SiO<sub>2</sub>/Si substrate. The sample is then dried using nitrogen gas, heated to 150 °C for 15 minutes to let the PMMA flow and then cooled to room temperature. The heating step ensures better adhesion. The sample is then placed in acetone for 20 minutes to dissolve the PMMA film. Finally, the sample is rinsed with IPA to get rid of soluble fragments and impurities. The sample is then annealed in a steady flow of argon and hydrogen gas at 350 °C for three hours. The annealing increases the contact between graphene and hBN by conforming the graphene sheet onto the substrate<sup>65</sup>.

### 4.3 Electronic properties of g-hBN

Graphene devices that use hBN as the substrate have shown much better performance compared to devices that use SiO<sub>2</sub> as the substrate<sup>47</sup>. The amorphous nature of SiO<sub>2</sub> results in the rough topography of its surface. This translates to the corrugations in the graphene layer, which is bad for transport properties. Trapped charges in the SiO<sub>2</sub> layer also cause spontaneous doping in the graphene layer. This results in large fluctuations of charge density (i.e. the Fermi level of graphene) over the sheet of graphene. Using hBN as the substrate alleviates both these issues. Jiamin Xue et al<sup>48</sup> have found that the surface roughness of the graphene layer reduces from 224.5 pm for graphene on SiO<sub>2</sub> to 30.2 pm for graphene on hBN. They also report that

charge fluctuations of graphene on SiO<sub>2</sub> are 100 times larger than for graphene on hBN. The surface topography and charge density fluctuations are shown in *Figure 4.5*.

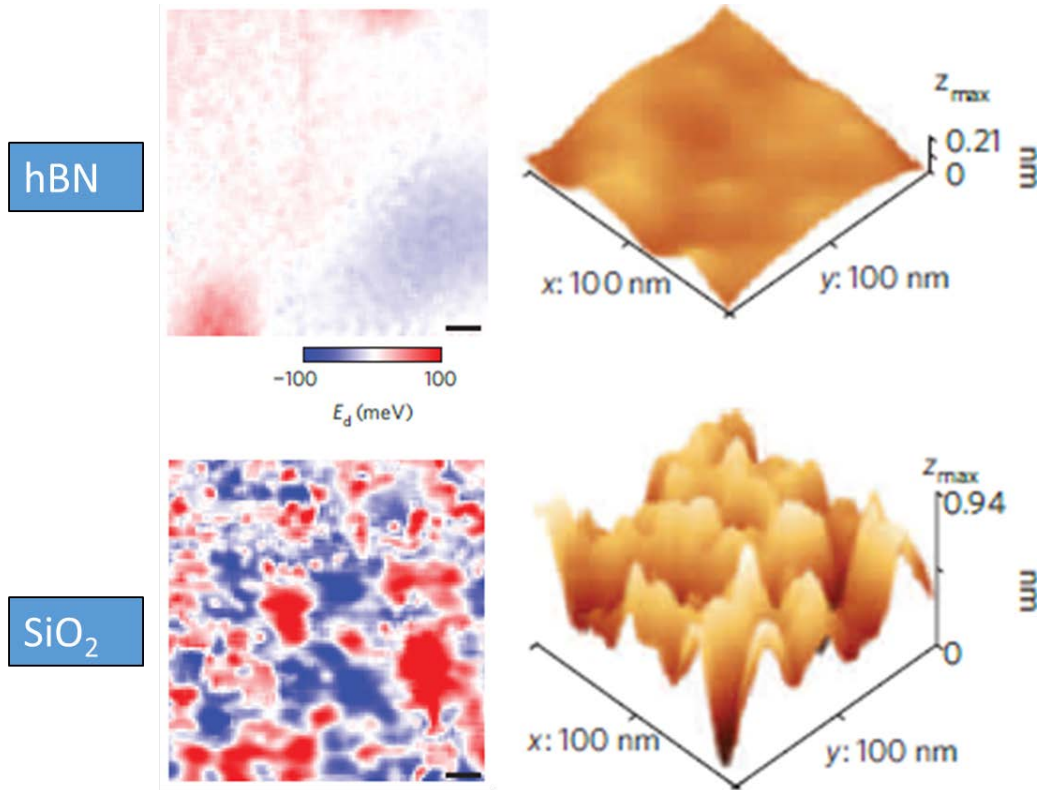


Figure 4.5: Charge fluctuations (left), represented by variation in Fermi level, and surface topography (right) for graphene on hBN (top) and SiO<sub>2</sub> (bottom). Image adapted from Jiamin Xue et al, Nature Materials, Vol 10, pages 282 – 285 (2011).

Graphene on hBN substrates also exhibits periodic modulations that correspond to the Moiré pattern, which results when superposing two similar lattices on top of each other<sup>48,53</sup>. The wavelength of this pattern is longer than the atomic lattice, and depends on the angle between the lattices<sup>53</sup>. The moiré pattern serves as a weak periodic potential for the graphene layer. This weak periodic potential leads to the formation of new Dirac points<sup>52,54</sup> around the K and K' points in the

graphene Brillouin zone. The energy at which these new Dirac points occur depends on the wavevector ( $\vec{G}$ ) of the moiré pattern as  $E_{new} = \pm \frac{\hbar v_f |\vec{G}|}{2}$ , assuming that the graphene Dirac point is at  $E = 0$ . Here,  $v_f$  is the velocity of the massless Dirac fermions near the original Dirac point. The generation of new Dirac points at the zone boundaries of the superlattice Brillouin zone (related to the moiré pattern) is because the states with crystal momentum  $\vec{k}$  are mixed with states with crystal momentum  $\vec{k} - \vec{G}$  due to the periodic superlattice potential. The modified bandstructure near the new Dirac points is shown in *Figure 4.6*. The figure was generated by modifying the Dirac Hamiltonian of graphene with a weak periodic potential of the moiré pattern as done in Ref. 42.

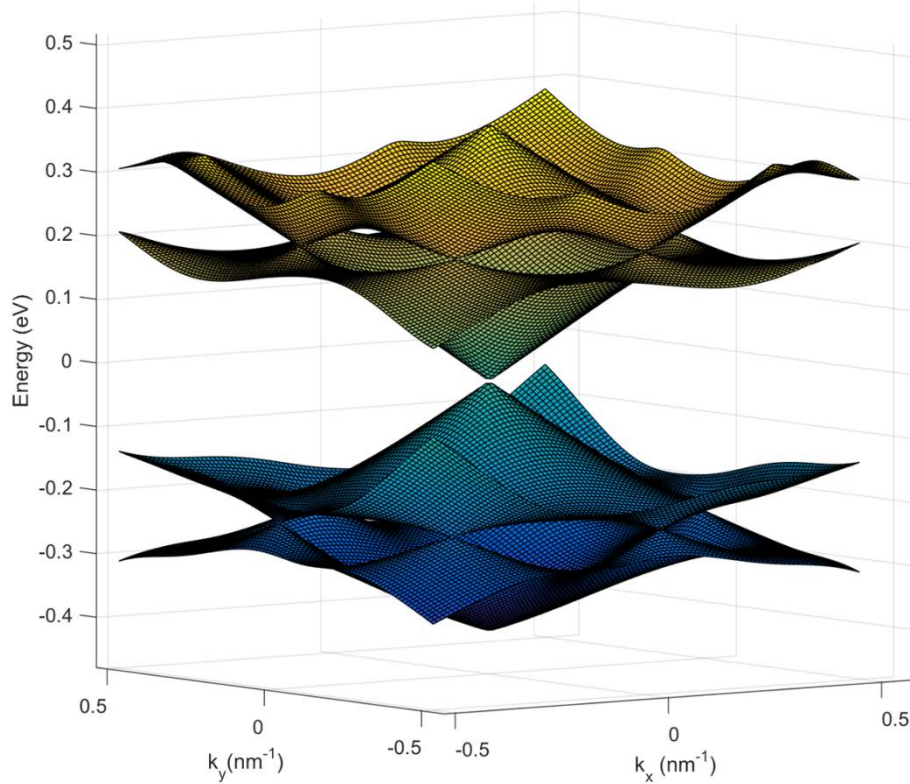


Figure 4.6: Bandstructure of graphene near the Dirac point modified by the weak periodic superlattice potential. New Dirac points are formed around the original Dirac point.

## 4.4 Ultrafast relaxation of hot phonons in g-hBN Heterostructures

Graphene heterostructures have garnered a lot of interest in the last decade<sup>66</sup>. Advances in fabrication techniques have made it possible to engineer devices with better transport, optical, and thermal properties<sup>47</sup>. As described in the previous section, heterostructures of graphene and hBN show much higher mobility compared to those using SiO<sub>2</sub> as a substrate<sup>47,48,53</sup>. This improvement is a result of the hBN

substrate being free of charged impurities, and displacing the graphene away from the impurities in the SiO<sub>2</sub> substrate<sup>48</sup>. In this section, I will describe our efforts to track the cooling of hot photo-excited carriers in graphene-hBN (g-hBN) heterostructures using ultrafast pump-probe spectroscopy. Our observations indicate that the carriers cool down four times faster in the case of graphene on hBN than on a silicon oxide substrate thus overcoming the hot phonon (HP) bottleneck that plagues cooling in graphene devices.

As electronic devices continue to scale down in size and push power capabilities, heat management has become a critical issue. Relaxation dynamics of photoexcited (PE) carriers has been studied extensively by many groups using variety of techniques such as photocurrent measurement, Raman time resolved Raman spectroscopy, transport measurements, and ultrafast pump-probe spectroscopy<sup>36,67,68</sup> etc. Upon photoexcitation (with an ultrafast pulse for example), electrons and holes are excited, into a highly non-thermal system. This bath of carriers exchanges energy among themselves through coulombic interactions, and thermalize into a hot (~1000K) Fermi-Dirac population within tens of femtoseconds<sup>69</sup>. This hot thermal population cools further through the emission of optical phonons near the  $\Gamma$  point of the phonon dispersion. When the temperatures of the carriers and optical phonon bath equalize, this cooling channel slows down, and this is termed as the Hot Phonon (HP) bottleneck<sup>67,70-74</sup>. Cooling through direct acoustic phonon emission is not viable because of a vanishingly small phase space for such a scattering process<sup>75</sup>. The hot optical phonons cool down through anharmonic decay to acoustic phonons, which are subsequently

absorbed into the substrate. Direct cooling of the charge carriers is also predicted to occur through coupling with the surface phonons of the underlying polar substrate<sup>73,76–78</sup>. Theoretical predictions and experiments place the hot optical phonon lifetime in graphene, graphite, and CNTs in the 1-5ps range<sup>67,70,79–82</sup>. The buildup of optical phonons is detrimental to device performance, and the HP bottleneck has been invoked to explain current saturation and negative differential conductance in graphene and CNTs<sup>71,72,83</sup>. The HP bottleneck also affects the photoresponse<sup>84</sup> of optoelectronic devices. Exploring cooling channels that can efficiently de-energize the optical phonons and remove the HP bottleneck is important. In that regard, graphene heterostructures incorporating an appropriate substrate, such as hBN, could offer additional mechanisms for accelerating the cooling process. Recent reports show that the active cooling efficiency due to the Peltier effect in graphene-hBN devices is more than twice as big as the highest reported room temperature efficiency<sup>85</sup>. A comparative study of relaxation dynamics for graphene on hBN and SiO<sub>2</sub> is missing from literature. In this section, we study the relaxation of carriers in graphene-hBN heterostructure devices. Our findings indicate that the substrate interface plays a major role in the carrier cooling process, and carriers in graphene devices fabricated on hBN substrates relax significantly faster than those on SiO<sub>2</sub> substrates thus providing relief of the HP bottleneck and enabling better device performance.

#### 4.4.1 Experimental Results

An optical image of one of the samples used in this study is shown in *Figure 4.7*. The spot marked 1 has graphene on hBN (g-hBN) whereas

spot 2 has graphene on SiO<sub>2</sub> (g-SiO<sub>2</sub>). The Raman spectra of g-SiO<sub>2</sub> and g-hBN are shown in Fig. 4.7 (b). The absence of a D peak means that both the g-SiO<sub>2</sub> and g-hBN are defect free. We can infer from the G and 2D peak positions that g-SiO<sub>2</sub> and g-hBN are p-doped by about  $3.5 \times 10^{12} \text{ cm}^{-2}$  and  $1 \times 10^{12} \text{ cm}^{-2}$  respectively<sup>20,21</sup>, which is well below the 1.58 eV probing photon energy.

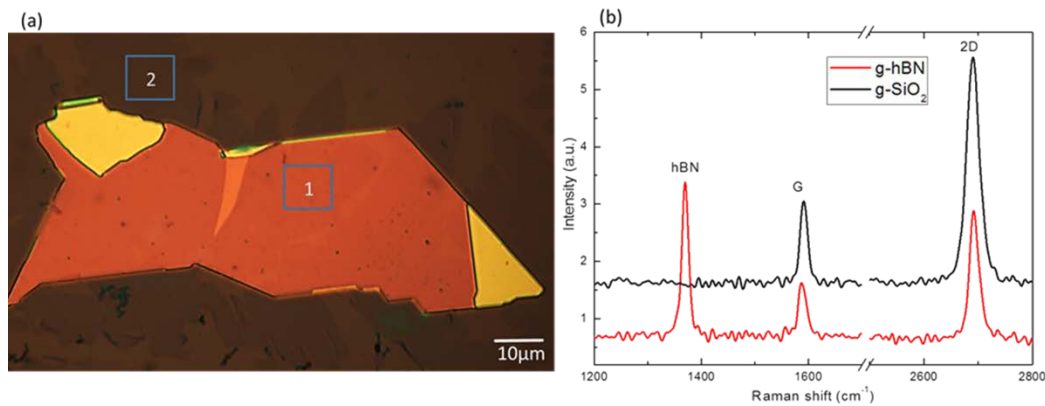


Figure 4.7: (a) Optical image of sample 1. The mean thickness of the hBN flake shown here is 118 nm as measured using AFM. Spot marked 1 is g-hBN and spot marked 2 is g-SiO<sub>2</sub> (b) Raman spectra of the graphene on hBN (red) and on SiO<sub>2</sub> (black). The curves are vertically offset for clarity.

For the pump-probe study I used amplified 780 nm pulses from our Ti-sapphire laser amplifier for both pump and probe beams. I measured the spot sizes (spatial FWHM) of the pump and probe beams using the knife edge technique as 154 μm and 23 μm respectively. The temporal FWHM of the pulses as measured using the FROG technique was 45 fs. I conducted the experiment with a range of pump pulse energies, all of which were below the damage threshold of graphene under irradiation with ultrafast pulses<sup>22</sup>. The pump was chopped using an optical chopper, and the probe reflectivity of the sample was

measured using lock-in detection. The polarizations of the pump and probe were crossed for better rejection of the pump scatter.

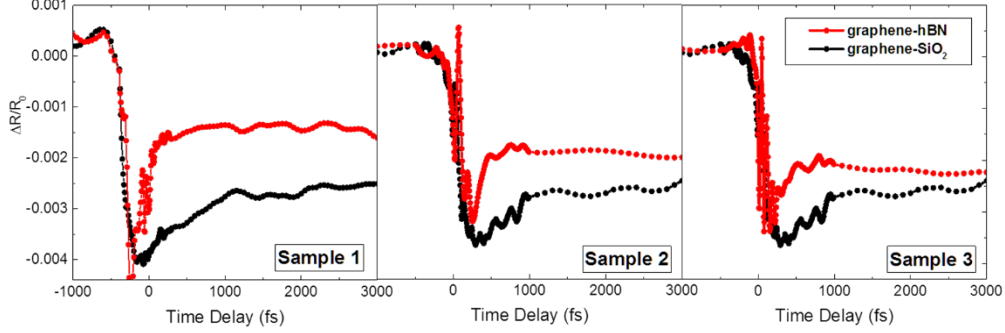


Figure 4.8: Experimental differential reflectivity curves for different samples of g-hBN pumped using  $60 \frac{\mu J}{cm^2}$  per pulse. The reflectivity of g-SiO<sub>2</sub> is shown for comparison (red: g-hBN and black: g-SiO<sub>2</sub>)

The relaxation of PE carriers is captured by the differential reflectivity,  $\frac{\Delta R(t)}{R_0}$ , of the sample. Fig. 4.8 shows  $\frac{\Delta R(t)}{R_0}$  as a function of the pump-probe time delay for three different g-hBN structures along with curves for g-SiO<sub>2</sub> for comparison. It is immediately evident from Fig. 4.8 that the relaxation dynamics of g-hBN are faster than that of g-SiO<sub>2</sub>.

The pump pulse energy is  $60 \frac{\mu J}{cm^2}$ . The baseline at large positive pump probe delay is non-zero because of the underlying contribution from silicon base of our samples. This baseline is constant over 100 picoseconds, which is far greater timescale than the cooling of charge carriers in graphene. We have independently verified that this baseline does not contribute to the lifetimes extracted from our experiment as seen in *Figure 4.9*. The addition of hBN flake does not change the response of silicon in any way since hBN is transparent to the pump light (780nm). The thickness of the hBN doesn't affect the relaxation

timescale as seen from Fig. 4.9 (a). The  $\frac{\Delta R(t)}{R_0}$  versus time delay measurements shown above relax to a non-zero value. This is the residual signal shown by the silicon chip on which the graphene and hBN flakes are deposited. The reflectivity curves for the plain Si/SiO<sub>2</sub> show that we can approximate the silicon response with a sigmoidal function. This response has no decay as we have verified over 70 ps (Fig. 4.9 (b)).

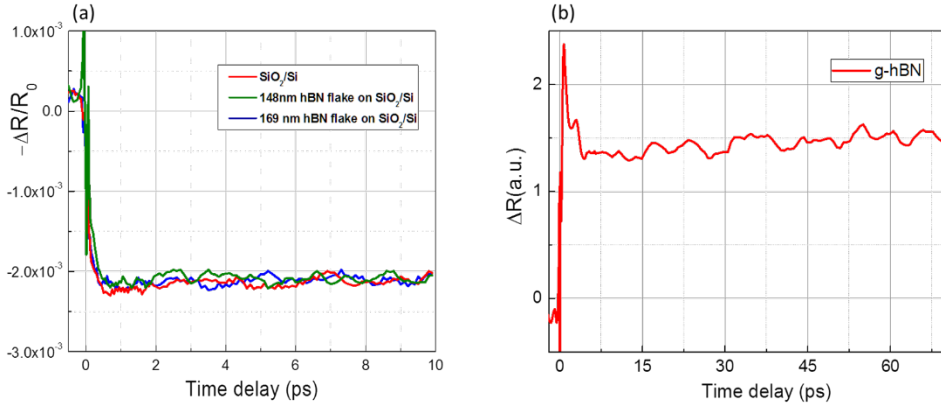


Figure 4.9: (a) Reflectivity curves for plain SiO<sub>2</sub>/Si chip and hBN flakes over various thicknesses. (b) Long scan of time delay of g-hBN showing a flat response after the initial cooling.

#### 4.4.2 Two-Temperature Model

In order to quantify the timescales observed in the experiment we modeled the temperature dynamics of the heterostructure using a two-temperature model<sup>86,87</sup>. The two-temperature model simulates the heat transfer between the laser, charge carriers, phonons, and the substrate. The equations that govern the electronic temperature ( $T_{el}$ ) and optical phonon temperature ( $T_{op}$ ) are:

$$\frac{dT_{el}}{dt} = \frac{I(t) - \Gamma(T_{el}, T_{op})}{c_{el}(T)} \quad 4.5$$

$$\frac{dT_{op}}{dt} = \frac{\Gamma(T_{el}, T_{op})}{c_{op}(T)} - \frac{T_{op} - T_0}{\tau_{op}} \quad 4.6$$

$T_0$  is the ambient room temperature;  $c_{op}$  and  $c_{el}$  denote the phononic and electronic heat capacity of graphene;  $I(t)$  is the time profile of the pump pulse, which is assumed to be a Gaussian with a FWHM of 45 fs. The thermal relaxation timescale is  $\tau_{op}$ , which denotes the optical phonon lifetime in graphene. The coupling between  $T_{el}$  and  $T_{op}$  is given by the function  $\Gamma(T_{el}, T_{op})$ , which governs the rate of generation and absorption of the phonons.

$$\Gamma(T_{el}, T_{op}) = \beta \left\{ \left(1 + n(\hbar\Omega, T_{op})\right) \int D(E)D(E - \hbar\Omega)f(E, T_{el})(1 - f(E - \hbar\Omega)) dE - n(\hbar\Omega, T_{op}) \int D(E)D(E + \hbar\Omega)f(E, T_{el})(1 - f(E + \hbar\Omega))dE \right\} \quad 4.7$$

The coupling constant ( $\beta$ ) is taken as  $8 \frac{eV^2}{cm^2.s}$ , which is the best fit with the experimental data.  $D(E)$  is the density of electronic states of graphene is given by  $D(E) = \frac{2E}{\pi} (\hbar v_f)^{-2}$ . The Fermi-Dirac formula for the distribution of carriers is  $f(E, T_{el}) = \left( \exp\left(\frac{E}{kT_{el}}\right) + 1 \right)^{-1}$ . The Bose-Einstein occupation of optical phonons at energy  $\hbar\Omega$  is  $n(\hbar\Omega, T_{op}) = \left( \exp\left(\frac{\hbar\Omega}{kT_{op}}\right) - 1 \right)^{-1}$ . The two optical phonons branches that contribute are the  $E_{2g}$ -mode phonons near the  $\Gamma$ -point and  $A_1$ -mode phonons near the K-point of graphene. We neglect the dispersion, and assume that  $\hbar\Omega \approx 200 \text{ meV}$ . The expressions for the  $c_{el}$  and  $c_{op}$  are derived from theory and experiment respectively, and the values for both are taken from the work by Chun Hung Lui et al<sup>88</sup>.

The graphene was assumed to be intrinsic after verifying that the doping only affects the maximum  $T_{el}$  reached by 2%, and doesn't change the time dynamics. We keep the electron-phonon interaction strength ( $\beta$ ) fixed for all cases, and vary the absorbed fluence to match the peak electronic temperature with the experimental value. The model can easily be extended to include the transient heating of the hBN (and for the SiO<sub>2</sub> underneath) due to the inflow of heat from the graphene layer but the rise in temperature of the substrate is negligible ( $\sim 1$ K) because of the large specific heat capacity of hBN. Once the electronic temperature is obtained from the above equations, we can extract the optical conductivity ( $\sigma$ ) and refractive index ( $\eta$ ) of graphene from the equations:

$$\sigma_{inter}(T) = \frac{\pi e^2}{2h} \tanh \frac{E_{probe}}{4kT} \quad 4.8$$

$$\sigma_{intra}(T) = \frac{\pi e^2}{2h} \left( \frac{8 \ln(2)}{\pi} \right) \frac{\gamma kT}{(E_{probe}^2 + \gamma^2)} \quad 4.9$$

$$\eta_{graphene} = \sqrt{\varepsilon_{core} + \frac{i(\sigma_{inter} + \sigma_{intra})}{\varepsilon_0 \omega}} \quad 4.10$$

$\sigma_{inter}$  and  $\sigma_{intra}$  denote the interband and intraband contributions to the optical conductivity respectively. The contribution of the core electrons (that don't participate in electronic transitions) to the relative permittivity of graphene is denoted as  $\varepsilon_{core}$ . We calculated the reflectivity of the graphene/hBN/SiO<sub>2</sub>/Silicon stack using the transfer matrix method of thin film interference<sup>89</sup>. Thus, knowing the electronic temperature,  $T_{el}(t)$ , as a function of time delay allows us to calculate reflectivity,  $R(t)$ , as a function of time delay. The differential reflectivity of the sample shows the opposite trend as the electronic temperature,

i.e., a decrease in  $\frac{\Delta R(t)}{R_0}$  corresponds to an increase in the electronic temperature as seen in Fig. 4.10.

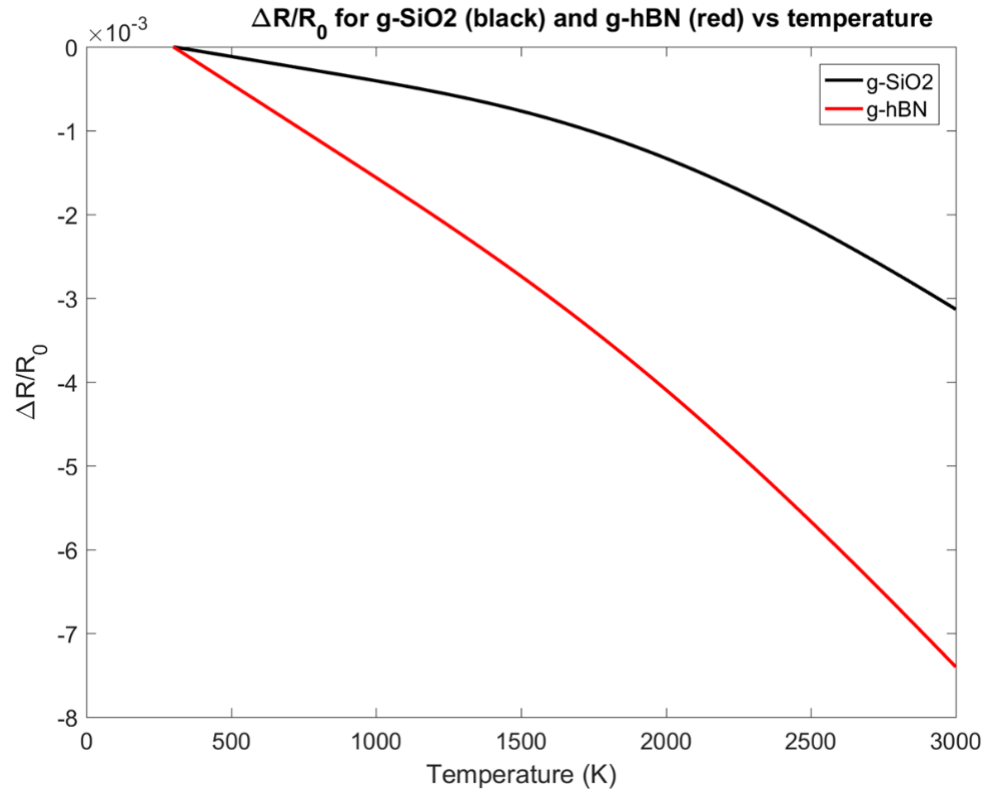


Figure 4.10: Differential reflectivity curves versus temperature for g-hBN (red) and g-SiO<sub>2</sub> (black) calculated using the two-temperature model.

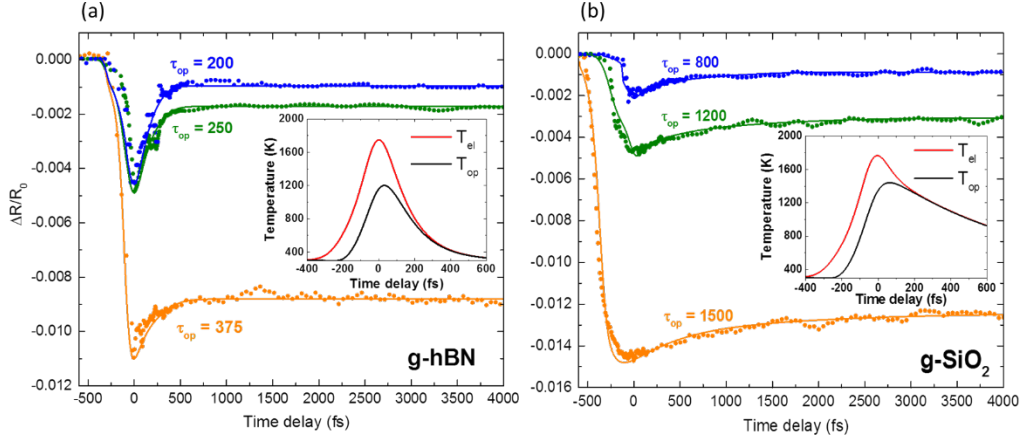


Figure 4.11 : (a) Differential reflectivity curves for graphene-hBN with different pump fluences: 80  $\frac{\mu\text{J}}{\text{cm}^2}$  (orange), 60  $\frac{\mu\text{J}}{\text{cm}^2}$  (green) and 50 (blue)  $\frac{\mu\text{J}}{\text{cm}^2}$ . (b) Differential reflectivity curves for graphene-SiO<sub>2</sub> for the same fluences. Inset: Electronic (red) and phonon (black) temperature profiles for the case with the lowest fluence.

Fig. 4.11 (a) shows the relaxation for g-hBN pumped with pulse fluences of 80 (orange), 60 (green) and 50 (blue)  $\frac{\mu\text{J}}{\text{cm}^2}$  for which we extract optical phonon lifetimes of 375 fs, 250 fs and 200 fs ( $\pm 25\text{fs}$ ). Fig. 4.11 (b) shows the corresponding fits for g-SiO<sub>2</sub>, and the corresponding lifetimes are 1500 fs, 1200 fs, and 800 fs ( $\pm 50\text{fs}$ ). The inset shows the temperature profiles for the case with the fastest decay. We assume that the only cooling mechanism available to the electrons is through losing heat to the optical phonon bath. Other possible modes of electronic cooling, such as directly coupling to the substrate or coupling to the acoustic phonons, are neglected. The interplay between the electron-phonon coupling strength ( $\beta$ ) and optical phonon lifetime ( $\tau_{op}$ ) determines whether the electrons cool down substantially before equilibrating with the phonons, i.e. before the bottleneck sets in. The fast decay of optical phonons in the case of g-hBN has an immediate

cooling effect on the electronic temperature. As seen in the temperature profile for g-SiO<sub>2</sub>,  $T_{el}$  and  $T_{op}$  equalize around 1200 K whereas for g-hBN the temperatures have cooled down to 600 K before equalizing. The phonon relaxation lifetimes in g-hBN are lower than those measured for g-SiO<sub>2</sub> by about a factor of four for all fluences indicating that additional cooling channels for graphene's optical phonons are available when hBN is used as the substrate. The range of values of  $\tau_{op}$  for g-SiO<sub>2</sub> (0.8 – 1.5 ps) agrees well with previous measurements of the phonon lifetime in SiO<sub>2</sub> supported graphene<sup>74,82</sup>. At higher fluences (i.e. high initial carrier densities), multibody effects like carrier screening, plasmonic modes, and plasmon-phonon interactions might come into play<sup>90</sup>. While these multibody effects are not captured by the simple two-temperature model, it still allows us to phenomenologically deduce the optical phonon relaxation lifetime.

The doping profile changes the total energy absorbed from the pump pulse; thus, the maximum electron temperature. This might affect the simulated dynamics. To address this question, we simulated the dynamics with and without the doping. The Fermi energy,  $\mu(T_{el})$  of the electrons is a temperature dependent quantity. Considering the high temperature involved in our experiment, we need to take the Fermi energy shift into account. To incorporate the temperature dependent Fermi energy into our simulation, we modify the expression for the specific heat as follows.

$$\begin{aligned}
C_{el} &= \frac{d}{dT} \left[ \int_0^{+\infty} D(E) f(E - \mu(T_{el}), T_{el}) E dE \right] \\
&= \frac{d}{dT} \left[ \int_0^{+\infty} N(E) E dE \right]
\end{aligned} \tag{4.11}$$

Where  $N(E)$  is the number density at energy  $E$ . The expression for  $\mu(T_{el})$  can be derived by invoking the expression for total carrier concentration which is constant. The g-SiO<sub>2</sub> in our experiment is p-doped with a hole density of  $\sim 3 \times 10^{12} \text{ cm}^{-2}$  whereas the g-hBN has smaller initial doping ( $\leq 1 \times 10^{12} \text{ cm}^{-2}$ ).

$$N_{tot} = \int_0^{+\infty} D(E)f(E - \mu(T_{el}), T_{el})dE \quad 4.12$$

Solving the equation for moderately high temperatures ( $> 300K$ ) shows an asymptotically inverse variation with temperature<sup>91</sup>:

$$\mu(T) \propto \frac{N}{T} \quad 4.13$$

We can therefore ignore the variation of the Fermi energy with temperature, since the initial temperatures of carriers in the sample is very high. Incorporating the initial p-doping of the sample gives a small linear correction term. The effect of including this term in the differential reflectivity of g-hBN is shown in *Figure 4.12*. We note that the doping doesn't change the carrier cooling dynamics.

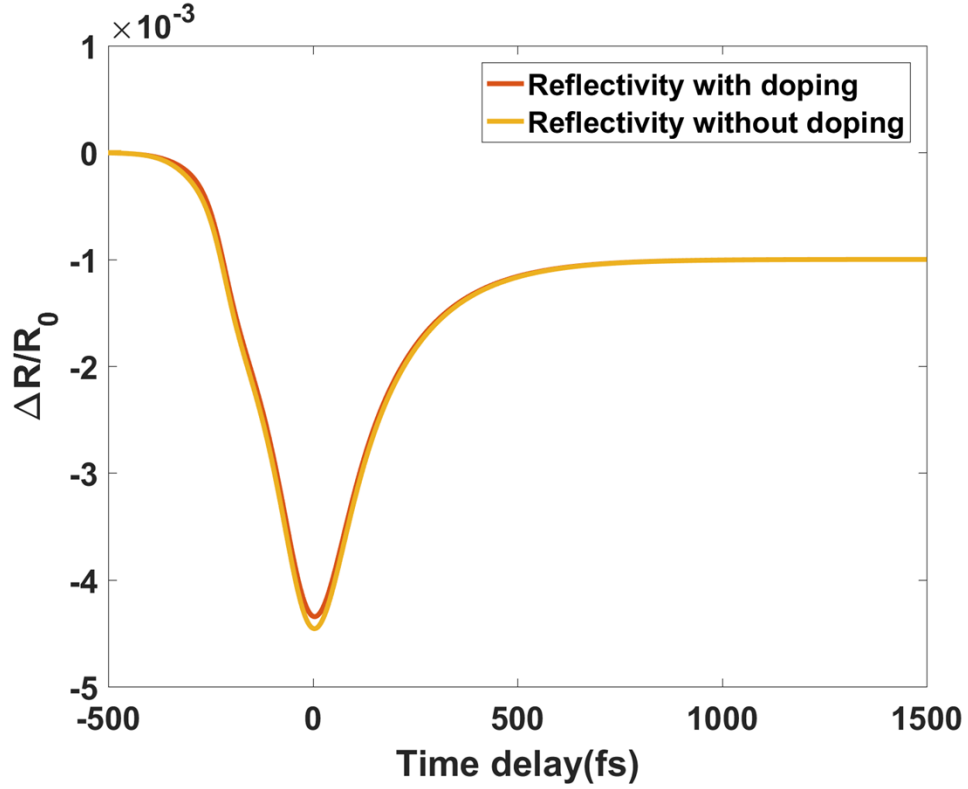


Figure 4.12: Transient differential reflectivity curves for g-hBN calculated ignoring (yellow) and including (red) the initial p-doping doping.

#### 4.4.3 Heat transfer in graphene heterostructures

At low fluence where these multibody effects are relatively small, and the temperature differential is smallest, we can estimate the interfacial thermal conductance of the graphene – hBN interface from the optical phonon lifetimes using the lumped heat capacity model. The phonon lifetime is related to the interfacial conductance by the equation

$$G_k = \frac{c_{eff}}{\tau_{op}} \quad 4.14$$

where,

$$\frac{1}{c_{eff}} = \frac{1}{c_{hBN}} + \frac{1}{c_{op}+c_{el}} \quad 4.15$$

The heat capacity  $c_{eff}$  is the effective heat capacity per unit area of the composite graphene-hBN system<sup>92</sup>. The heat capacity and thermal conductance of hBN can be ignored because the limiting term in the vertical heat transport dynamics of the heterostructure is the interfacial thermal conductance between graphene and the substrate. Since the measured phonon lifetime shows a decreasing trend with the temperature differential, we estimate the lower limit of the room temperature interfacial conductance of the graphene-hBN interface from our measured relaxation lifetime for the lowest fluence as  $16.25 \frac{MW}{m^2.K}$  at room temperature. The corresponding value for the graphene-SiO<sub>2</sub> interface is  $3.75 \frac{MW}{m^2.K}$ . The value of  $G_k$  for g-hBN measured here is higher than that reported in the work by Chen et al.<sup>93</sup> by more than a factor of two. The sample used in their experiment underwent electron beam lithography and oxygen plasma etching, which might have possibly affected the interface quality and suppressed the interfacial conductance. As far as we know, no previous measurements of the relaxation of carriers in graphene on hBN exist. For comparison, we can calculate the equivalent relaxation times from the alternate methods for measurements and predictions of the interfacial thermal conductivity of the graphene – hBN interface. The results are listed in table 1.

Study	$G_k \left( \frac{MW}{m^2.K} \right)$	Thermal time constant (fs)	Notes
Mao, R. et al <sup>94</sup>	187	17	Room temperature, theoretical
Pak, A. J. et al <sup>95</sup>	4	800	Room temperature, theoretical

Chen, C. C. et al <sup>93</sup>	7.41	435	Room temperature, experimental
Zhang, J. et al <sup>96</sup>	3	1076	200-700 K, theoretical
Ting Li et al <sup>97</sup>	1-10	300-3000	200-600 K, theoretical

Table 1: Interfacial thermal conductance and thermal time constants for graphene on hBN.

#### 4.4.4 Theoretical aspects of heat transfer in g-hBN

Many mechanisms have been proposed to explain the cooling of hot carriers in graphene. In this section, I will provide an overview of some theories and their implications.

*Figure 4.13* shows a schematic of the competing channels for energy transport between graphene's carriers, intrinsic phonons, and the substrate after excitation with an ultrafast laser pulse. As described in a previous section, one narrative of the cooling process is as follows: the laser pulse leaves behind an extremely hot bath of electrons in a highly non-equilibrium state. The electrons rapidly thermalize due to Coulomb mediated carrier-carrier scattering ( $\sim 30$  fs) and coupling with optical phonons ( $\sim 500$  fs)<sup>32,67,98</sup>. This fast thermalization time is also indicative of the fact that the electrons and holes reach the same temperature within tens of picoseconds<sup>69</sup>. Further cooling is limited by the cooling of the hot optical phonons through anharmonic coupling to acoustic phonons ( $1 - 5$  ps)<sup>79,81,82</sup>. Furthermore, the decrease in lifetime with the number of graphene layers has prompted a suggestion that the carriers directly interact with the lattice vibrations of the substrate<sup>82</sup>.

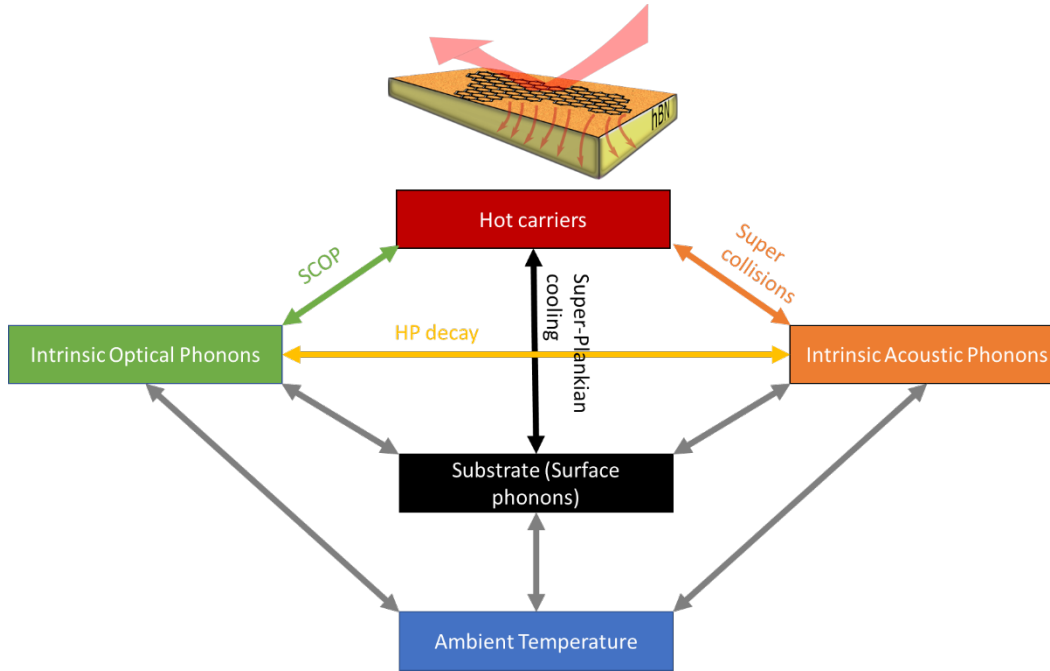


Figure 4.13: Different heat flow pathways available to photoexcited charge carriers.

Direct coupling of the carriers to the intrinsic acoustic phonons in graphene is not a major contributor to the cooling process because of the momentum mismatch between the acoustic phonons and carriers reduces the phase space for such a process. Recent theoretical<sup>99</sup> and experimental<sup>100–102</sup> evidence has pointed to a defect mediated scattering between the carriers and acoustic phonons in graphene called supercollision cooling. In this process, the defects provide the momentum mismatch between the acoustic phonons and the carriers<sup>103</sup>. The importance of the supercollision pathway increases at high defect densities<sup>101</sup>, low carrier energies, and higher lattice temperatures<sup>100,103</sup>. The cooling rate in a supercollision process is governed by the equation<sup>99</sup>

$$J = A(T_{el}^3 - T_{ac}^3) \quad 4.16$$

where  $T_{ac}$  is the temperature of the acoustic phonon. Solving Eqn. 4.16, we get a hyperbolic temperature decay.

$$T_{el}(t) = \frac{T_{el}(0)}{1 + \frac{t}{\tau_0}} \quad 4.17$$

This hyperbolic cooling profile does not give a good fit with our data for graphene on hBN. The interface between graphene and hBN is free of defects and impurities therefore, defect mediated supercollision process cannot be the major cooling pathway for g-hBN.

Another alternative cooling mechanism that has been proposed is the coupling of carriers in graphene with the phonon-polaritons of the substrate<sup>76,104</sup>. At the time of this writing, researchers have recently found experimental evidence for Super-Planckian cooling<sup>105</sup>. In the so called Super-Planckian cooling mechanism of carriers in graphene, the electrons couple radiatively with the hyperbolic phonon-polariton modes in hBN. This near field (evanescent) coupling between the carriers and substrate provides a very efficient cooling channel and aids in the fast cooling of photoexcited carriers in graphene.

The interaction between graphene and the substrate also depends on many other factors like topographic conformity, coulombic interactions and adhesion energy. The g-hBN interface can be more transparent to heat carrying phonons because of the similar masses of carbon, boron, and nitrogen<sup>94</sup>. The curvature of the graphene sheet is an additional contributor to the interface thermal resistance in g-SiO<sub>2</sub><sup>95</sup>. Annealing contributes to the graphene sheet conforming to the substrate and hBN being atomically flat means the graphene sheet in g-

hBN has lower cumulative curvature than the graphene sheet in g-SiO<sub>2</sub> effectively decreasing interfacial resistance in g-hBN.

In summary, we've seen that interlayer interactions play a major role in the carrier dynamics of graphene heterostructures. In the next chapter, I will introduce another class of 2D heterostructures called Transition Metal Dichalcogenides (TMDs) which are complementary to graphene because of their semiconducting properties. I will present non-degenerate pump-probe measurements that show that strong electron-phonon interactions can cause renormalization in the bandstructure of TMDs.

# CHAPTER 5.

## Phonon Induced Renormalization in Transition Metal Dichalcogenides

The discovery of graphene paved the way for an immense volume of research into two-dimensional, atomic layer materials. There now exists a repertoire of 2D materials that includes metals (e.g., NbSe<sub>2</sub>), semimetal (graphene), semiconductors (MoS<sub>2</sub>, WS<sub>2</sub>, MoSe<sub>2</sub> and WSe<sub>2</sub>) and insulators (hBN). These materials can be mixed and matched to build heterostructures with optical, electronic or thermal properties that suit specific applications. TMDs (MoS<sub>2</sub>, WS<sub>2</sub>, MoSe<sub>2</sub> and WSe<sub>2</sub>) are a subclass of 2D materials that retain the convenient planar honeycomb structure of graphene. They are semiconductors with a direct optical band gap in the visible spectrum therefore they absorb strongly in the visible region of the optical spectrum. This opens possibilities for optoelectronic device applications. In principle, because of the high binding energy of the excitons in TMDs, we could make very efficient photovoltaic devices by harnessing photoexcited charge carriers. Conversely, we can inject charge carriers into TMD based p-n junction devices to make visible light sources. Coupled spin and valley degree of freedom makes TMDs a potential candidate for the burgeoning fields of spintronics and valleytronics.

The room temperature photoluminescence (PL) efficiency of TMD samples is low ( $\sim 1\%$ )<sup>106</sup>. Photodetectors and LED devices made using TMD materials also suffer from low quantum efficiency. At low temperatures, the recombination of excitons is dominated by radiative recombination<sup>107,108</sup>. At higher temperatures (above 100 K) non-radiative recombination of carriers due to defect assisted recombination<sup>109–111</sup> or exciton-exciton annihilation processes<sup>107,112,113</sup> can come into play. Non-radiative recombination processes decrease exciton population and thus fewer excitons are left to combine radiatively effectively reducing the PL efficiency.

Chemical vapor deposition (CVD) techniques have made it possible to obtain large area samples quickly. Defects or impurities may be present in the lattice of CVD grown samples as remnants from the growth procedure<sup>109</sup>. Defects act like potential wells which trap carriers and excitons, effectively localizing them. A defect state can act as a recombination center if the wavefunction of the state has good overlap with the valence and conduction bands<sup>110</sup>. Therefore, states lying deep in the bandgap act as recombination centers where as shallow states (closer to the valence or conduction band) act as donor or acceptor states. Defects have also been proposed as a possible reason for low mobility in TMD transistors<sup>114</sup>

Another pathway for non-radiative recombination of carriers and excitons is through the mediation of phonons. Electron-phonon interaction is very important in semiconductors because apart from reducing the PL efficiency, hot phonon effect is responsible for low mobility and current saturation<sup>83,115,116</sup>. Experimental work on carrier-

phonon interactions in TMDs has been limited to variation of PL linewidth<sup>117</sup> and lifetime<sup>118–121</sup> with temperature. Theoretical efforts have concentrated on modelling lateral thermal conductivity<sup>122–124</sup>, phonon relaxation lifetimes<sup>125</sup>, phonon mediated free carrier cooling<sup>43</sup> and phonon-induced bandstructure changes<sup>126</sup>. In this chapter, I will present time domain experimental results indicating strong many-body interactions between carriers, excitons, defect states and phonons in WS<sub>2</sub>. Similar results were obtained for MoS<sub>2</sub> (appendix A) indicating that multibody interaction play a major role in the carrier recombination of TMDs.

## 5.1 Static spectroscopy of WS<sub>2</sub> and MoS<sub>2</sub>

Due to the reduced dimensionality of TMD materials, screening between charge particles is reduced compared to traditional semiconductors. This leads to large binding energies in excitons. The optical properties of these materials in the visible range are dominated by the excitonic resonances which lie a little below the band gap energy. *Figure 5.1* shows the bandstructure near the K valley of the Brillouin zone. An excitonic level (only A exciton shown) that lies a little below the conduction band and mid gap defect states that can trap and localize carriers are also shown below the band gap.

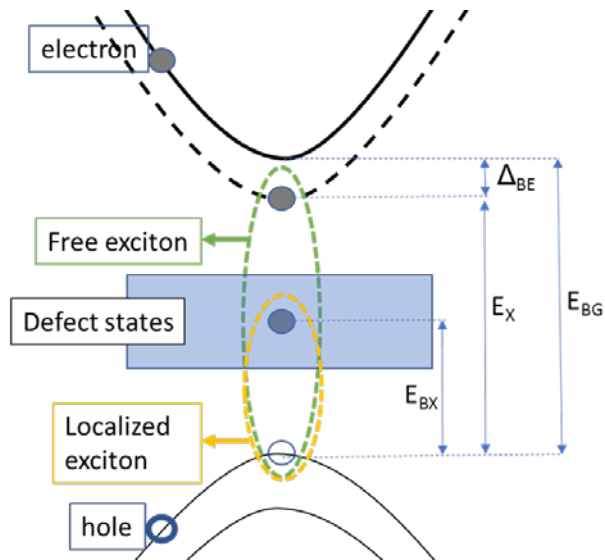


Figure 5.1: Schematic representation of the bandstructure of a TMD near the K point. Defect states, free and localized excitons are also shown.

The samples used in the experiments describe below were grown<sup>^</sup> using a CVD procedure on sapphire substrates. Individual triangular flakes as shown in Fig. 5.2 are monocrystalline with no domain walls. Since the spot size of the laser is  $< 10 \mu m$ , only the monocrystalline area is probed.

<sup>^</sup> Samples were grown by Sefaattin Tongay's group at ASU. Tempe, AZ.

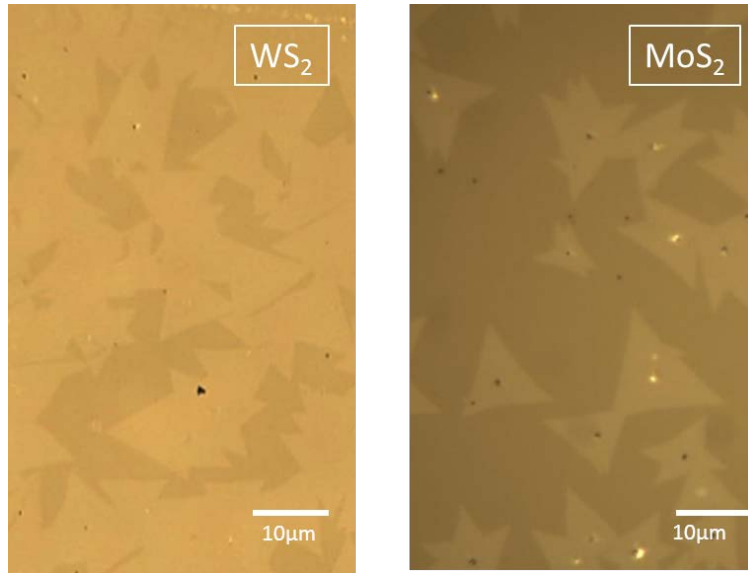


Figure 5.2: Optical images of CVD grown WS<sub>2</sub> (left) and MoS<sub>2</sub> on a c-sapphire substrate.

Optical absorption spectra and room temperature PL spectra of the samples are shown in *Figure 5.3*. Two peaks corresponding to the A and B exciton are seen in the absorption spectrum.

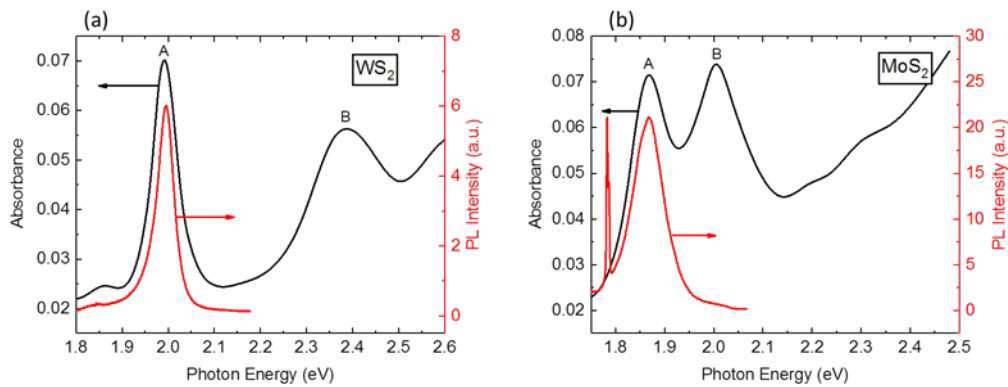


Figure 5.3: Absorbance (black) and photoluminescence (red) of (a) WS<sub>2</sub> and (b) MoS<sub>2</sub>

The absorption spectrum was obtained by using calculating the contrast of the sample over the sapphire background. If  $n_s$  is the refractive index of the substrate,  $R_{sam}$  and  $R_{sub}$  are the reflection

coefficients from the sample and bare substrate respectively; then we can calculate the absorbance<sup>♣</sup>,  $A$ , of the sample using the relation:

$$\frac{R_{sam} - R_{sub}}{R_{sub}} = \frac{4A}{n_s^2 - 1} \quad 5.1$$

## 5.2 Non-degenerate pump-probe spectroscopy of WS<sub>2</sub>

For the time resolved experiments, a 40 fs pulse train from a Ti-sapphire laser was frequency doubled to 400 nm and chopped at 200 Hz to be used as the pump beam. The pump fluences used ranged from  $400 \frac{\mu J}{cm^2}$  to  $1500 \frac{\mu J}{cm^2}$ . Tunable light pulses ( $\sim 40$  fs) in the visible region produced using an Optical Parametric Amplifier (OPA) were used to probe the pump-induced reflectivity changes in the sample. The pump and probe beams were cross polarized for better pump rejection at the detector. After photoexcitation, a host of multibody processes dictate the transient change in absorbance, such as phase space filling<sup>128</sup>, spectral broadening<sup>129</sup>, stimulated emission<sup>130</sup>, exciton-exciton scattering (biexciton formation<sup>131,132</sup>, exciton-exciton annihilation<sup>110</sup> and exciton self-renormalization<sup>129</sup>) and carrier-phonon interactions<sup>43,126,133</sup>. The pump-induced differential reflectivity,  $\frac{\Delta R}{R_0}$ , measured by the time resolved experiments can be converted to differential absorption change,  $\Delta A$ , using Eqn. 5.1:

$$\Delta A(\hbar\omega, t) = \frac{\Delta R(\hbar\omega, t)}{R_0} \left( A(\hbar\omega) + \frac{n_s^2 - 1}{4} \right) \quad 5.2$$

---

<sup>♣</sup>Absorbance is defined as  $A = -\ln\left(\frac{I_T}{I_i}\right)$ ; where  $I_i$  and  $I_T$  are the incident and transmitted intensities.

Where  $\frac{\Delta R(\omega,t)}{R_0}$  is the differential reflectivity signal measured with a probe energy  $\hbar\omega$  and time delay  $t$ .

Fig 5.4 shows the differential absorbance curves for WS<sub>2</sub> at probe energies of (a) 1.92 eV (red shifted from A-peak), (b) 2 eV (on resonance with A-peak) and (c) 2.06 eV (blue shifted from A-peak) respectively with a pump fluence of  $1500 \frac{\mu J}{cm^2}$ . We estimate a maximum initial photoexcited carrier density of  $5 \times 10^{14} cm^{-2}$  from the absorbance<sup>127</sup> of WS<sub>2</sub> at 400 nm (3.1 eV).

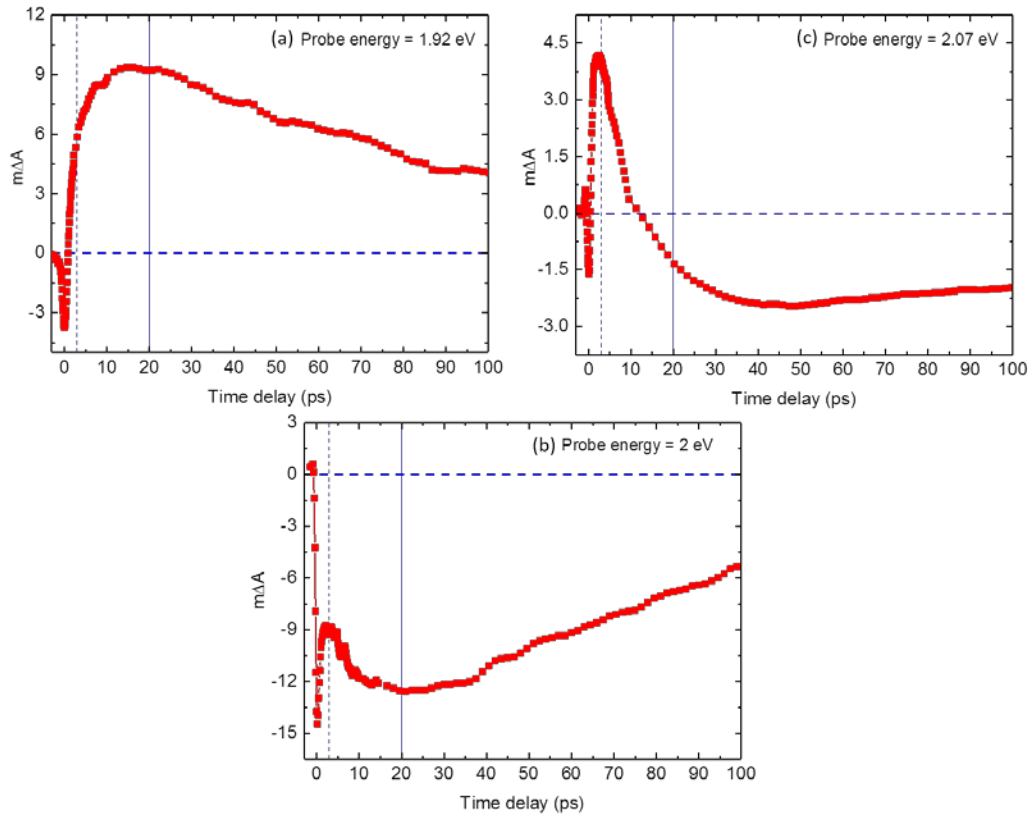


Figure 5.4: Transient absorbance curves for WS<sub>2</sub> at (a) 1.92 eV (b) 2 eV and (c) 2.07 eV at a pump fluence of  $1500 \frac{\mu J}{cm^2}$

The differential absorbance near the excitonic peak shows striking variation with probe photon energy. For example, we can see from *Figure 5.4* that the change in absorbance at a time delay of 3 ps (marked with a dashed vertical reference line) goes from a positive value at 1.92 eV to a negative value at 2 eV and back to a positive value at 2.06 eV. This oscillatory behavior of  $\Delta A$  near the exciton energy has been observed in both monolayer and bulk TMDs and is a signature of bandgap renormalization of the excitonic peak<sup>109,127,129</sup>. The dynamics at larger time delays, like the broad negative bump in Fig. 5.4 (b) around 20 ps (marked with a solid vertical reference line), cannot be easily explained using the standard narrative of carrier relaxation. To understand the dynamics, we need to delineate the contributions of the various multibody interactions at play in the system.

The pump pulse excites carriers into the conduction band which quickly lose energy via intravalley scattering and bind to oppositely charged carriers to form excitons. Within a couple of hundred femtoseconds most ( $\sim 60\%$ ) of the photoexcited free carriers cool down and bind with oppositely charged carriers to form excitons<sup>134,135</sup>. The increase in the population of excitons causes Pauli blocking from excitonic states which inhibits further absorption of the probe beam and consequently causes a dip in the transient absorbance. Thus, the absorbance near time delay zero initially decreases for all three probe energies. The Pauli blocking dip is followed by an immediate rise in transient absorbance which has been previously attributed to the absorption of the probe light by carriers trapped in the defect states<sup>109,136–140</sup>. This channel causes an increase in  $\Delta A$  that persists for a

$\sim 3$  ps after the negative peak due to Pauli blocking. The existence of defect states in our sample is seen in cold temperature (4.3 K) PL spectrum shown in *Figure 5.5* (a). The broad peak labelled ‘LE’ (for Localized Exciton) represents excitons that are trapped at defect sites. These localized excitons lose their kinetic energy and are thus ‘localized’. The peak labeled ‘FE’ is the free exciton peak which is blue shifted by about 60 meV from its position at room temperature (RT) due to carrier-phonon interactions. The LE peak is absent in the room temperature PL spectrum shown in *Figure 5.3* due to thermally activated non-radiative recombination as opposed to thermally induced dissociation due to its high binding energy<sup>118</sup>.

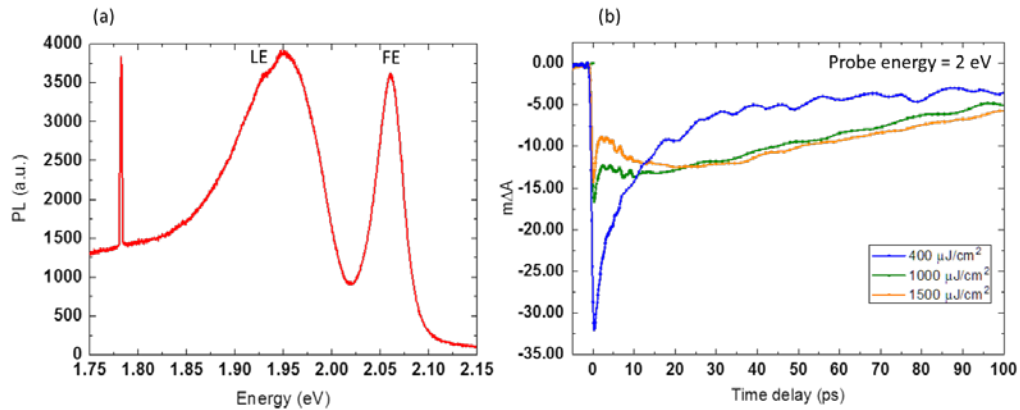


Figure 5.5: (a) PL of WS<sub>2</sub> sample at 4.3 K (b) Transient absorbance of WS<sub>2</sub> with varying fluence.

The LE peak is very broad indicative of a broad range of defect energies. In TMDs, defects such as metal atom vacancies, chalcogen atom vacancies, oxygen interstitial and grain boundaries, created by varying the growth parameters or induced via particle irradiation, have been identified using a variety of techniques such as TEM, XPS, STM,

Raman spectroscopy and PL spectroscopy<sup>109–111,141–147</sup>. Although both free carriers and carrier bound as excitons are susceptible to capture, the capture cross section of bound carriers is higher than that for free carriers<sup>110</sup>. Carrier trapping by defects related to oxygen substitution has been observed primarily in CVD grown TMDs<sup>109,136,148</sup> although it has been proposed to explain the recombination rates in exfoliated TMDs<sup>111</sup> also. Defect trapped carriers modifying the transient absorption signal has been seen before in low temperature grown semiconductors as well<sup>137–140</sup>. In all the above experiments, carrier trapping occurs in a few picoseconds followed by slow ( $\sim 100$  ps) release and recombination. To shed more light on the role of defect states in the increasing transient absorption signal, we varied the fluence of the pump excitation. *Figure 5.5* (b) shows the transient absorbance of WS<sub>2</sub> at 2 eV (on resonance with the exciton) at different fluences. Contrary to our expectation, the lowest fluence ( $400 \frac{\mu J}{cm^2}$ ) shows the deepest dip due to Pauli blocking and the magnitude of the dip decreases with increasing fluence. This can be explained by the effect of the defect state absorption increase which is completely absent at the lowest fluence. Since the defect capture time is of the order of exciton formation ( $\sim 1$  ps), at higher fluences, a higher population of excitons is trapped by the defect states leading to a higher increase of transient absorption. This reduces the magnitude of the Pauli blocking dip. The peak following the dip is higher for higher fluences showing defect induced absorption dominates the change in absorption at higher excitation densities. The transient absorption curve at low fluence shows a simple biexponential relaxation with a fast component due to exciton thermalization and a slow

component due to radiative recombination. The increase in the defect induced absorption peak also indicate that the defect states are not saturated with carrier trapping. The transient absorption curve at low fluence shows a biexponential relaxation with a fast excitation due to exciton thermalization and a slow component radiative recombination<sup>136</sup>. Two other contributions to the dynamics in the few-picosecond time delay regime are from Auger recombination and carrier induced band gap renormalization (BGR). Defect assisted fast Auger recombination of excitons has been proposed as a non-radiative pathway for decreasing exciton population in the few-picosecond regime. This partially counters the effect of Pauli blocking. Carrier induced BGR causes a red shift in the absorption spectrum<sup>127,149,150</sup>. This manifests as a decrease in absorption at 2 eV and increase in absorption at 1.92 eV. This is clearly seen in *Figure 5.4* as the dip in  $\Delta A$  near zero is more than twice as large at 2 eV ( $-0.015$ ) compared to the value at 1.92 eV ( $-0.007$ ).

At a probe energy of 1.92 eV and time delay between 3 – 20 ps the increasing transient absorbance saturates and starts decreasing towards zero. This behavior is similar to that observed by Ke Chen et al<sup>109,136</sup> in ML MoSe<sub>2</sub>. This slow decrease has a timescale of 131 ps and is the signature of trapped carriers being released through recombination with a carrier of opposite charge. To put it in other words, a defect releasing a hole is equivalent to its capturing an un-trapped electron and vice versa. This mechanism reduces the population of excitons and charged carriers in the system through non-radiative recombination. The excess energy is released as phonons leading to

lattice heating. The timescale of this recombination mechanism is slower than that of carrier trapping and ranges from 50 – 800  $ps$ <sup>109,136,148,151</sup> depending on the doping levels and defect density of the sample. As a contrast, defect assisted Auger recombination which does not involve phonons has a timescale of 1 – 2  $ps$ <sup>110,151</sup>.

However, transient absorption signal decay due to carrier recombination cannot explain the behavior of the transient absorbance curves at probe energy of 2  $eV$  beyond 5  $ps$ . A very broad minimum around delay of 20  $ps$  with a full width at half maximum of several tens of picoseconds, is clearly discernable. The feature at a time delay of 20  $ps$  is positive at 1.92  $eV$  but negative at 2.0  $eV$  and 2.06  $eV$ . The oscillatory nature of the feature with increasing probe energy indicates an optical bandgap renormalization effect corresponding to a red shifted absorption profile.<sup>127,129</sup> The very late onset of the feature ( $\sim 20$   $ps$ ) rules out carrier (both free and bound) induced renormalization as a possible cause for renormalization. Similarly, the late onset of the decrease in  $\Delta A$  rules out other carrier-population induced effects such as exciton-exciton annihilation, bi-exciton formation, intra and intervalley dark excitons etc. because the carrier population peaks near zero time delay and any effects caused due to carrier induced renormalization must be maximum at zero delay.

A potential mechanism for the late onset of absorption changes is phonon induced band gap renormalization. As mentioned before, phonons are emitted during the relaxation of photoexcited carriers and during the slow recombination of carriers at defect sites. Since the recombination timescale is very slow, the phonon population reaches a

maximum at later time delays as observed. There are many indications in literature to support the role of phonons in the observed red-shift of the excitonic peak. Theoretical calculations predict a large cross section for carrier-phonon interaction in TMDs<sup>133,152–154</sup>. Alejandro Molina-Sanchez et al<sup>126</sup> have performed ab-initio calculations for MoS<sub>2</sub> that prove that the optical phonon induced renormalization red-shifts the excitonic peak. Seffattin Tongay et al<sup>153</sup> showed the transition of multilayer MoSe<sub>2</sub> from an indirect to a direct bandgap material with an increase in temperature. Multi-phonon assisted process at defect sites has been proposed as the mechanism responsible for carrier relaxation in InGaAs/GaAs quantum dots<sup>155,156</sup>. Recently, a two-level recombination mechanism for defect mediated recombination through phonon emission was proposed to explain the non-radiative recombination rate in CdTe<sup>157</sup>.

### 5.3 Modelling recombination rates

To better understand the multibody interactions in our experiment, we can model the dynamics as a four-level system. The energy schematic of our model is show in Fig 5.6. The four states considered are the free carriers  $|C\rangle$ , excitons  $|X\rangle$ , defect-trapped states  $|D\rangle$  and the ground state  $|G\rangle$ . The various relaxation pathways and associated timescales are labelled. The phonons released upon recombination are denoted by the red wavy line.

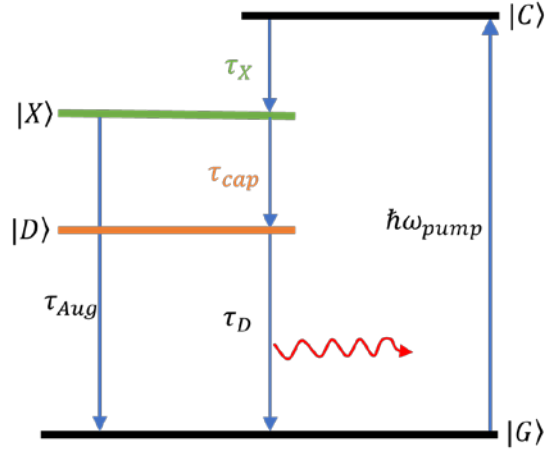


Figure 5.6: Energy schematic of the model used to simulate dynamics showing the coupling between states.

The time dynamics of the photoexcited TMD sample are described by the system of coupled differential equations:

$$\frac{dn_c}{dt} = I(t) - \frac{n_c}{\tau_X} \quad 5.3$$

$$\frac{dn_X}{dt} = \frac{n_c}{\tau_X} - \frac{n_X}{\tau_{cap}} - \frac{n_X}{\tau_{Aug}} \quad 5.4$$

$$\frac{dn_D}{dt} = \frac{n_X}{\tau_{cap}} - \frac{n_D}{\tau_D} \quad 5.5$$

$$\frac{dn_P}{dt} = k \cdot \frac{n_D}{\tau_D} - \frac{n_P}{\tau_{ph}} \quad 5.6$$

$I(t)$  is the incident pump pulse with a 40 fs gaussian profile;  $n_c$ ,  $n_X$ ,  $n_D$  and  $n_{ph}$  are the free carrier population, exciton population, population of the defect states and phonon population respectively. For simplicity, we ignore the difference between the release times of electrons and holes. We also ignore the capture of free carriers by defect sites because the capture cross-section is far lower compared to exciton capture<sup>110</sup>. The relaxation rates are as follows:  $\tau_X$  is the exciton

formation time,  $\tau_{cap}$  is the exciton capture time,  $\tau_{Aug}$  is the defect-assisted Auger recombination time,  $\tau_D$  is the phonon assisted recombination time and finally  $\tau_{ph}$  is the phonon relaxation time. The factor  $k$  in Eqn. 5.6 is proportional to the number of phonons released per recombination event. After solving the above equations, the differential absorbance is calculated using a simple proportionality formula:

$$\Delta A(\hbar\omega, t) = \alpha_X(\hbar\omega) \cdot n_X(t) + \alpha_D(\hbar\omega)n_D(t) + \alpha_{ph}(\hbar\omega)n_{ph}(t) \quad 5.7$$

Where the  $\alpha_X$  term determines the contribution of Pauli blocking and carrier-induced BGR,  $\alpha_D$  is the defect induced absorption coefficient which is proportional to the density of defects in the sample and  $\alpha_{ph}$  is the coefficient of phonon induced absorption change. We find that the bandgap renormalization due to phonons is of the same order of magnitude as carrier induced BGR, i.e.,  $\frac{\alpha_X}{\alpha_{ph}} \sim 1$ , although as expected, phonon induced effects are dominant at later time delays. *Figure 5.7* shows the fits for the data in *Fig. 5.4* with the values  $\tau_D = 60 \text{ ps}$  and  $\tau_{ph} = 20 \text{ ps}$ . The phonon relaxation time,  $\tau_{ph}$ , denotes the anharmonic decay rate of phonons into lower energy phonons and eventual transfer into the substrate. We could not find any prior theoretical or experimental estimates for the decay lifetime of phonons in  $\text{WS}_2$ . This is the first direct time-domain measurement of the phonon-induced BGR and phonon relaxation time.

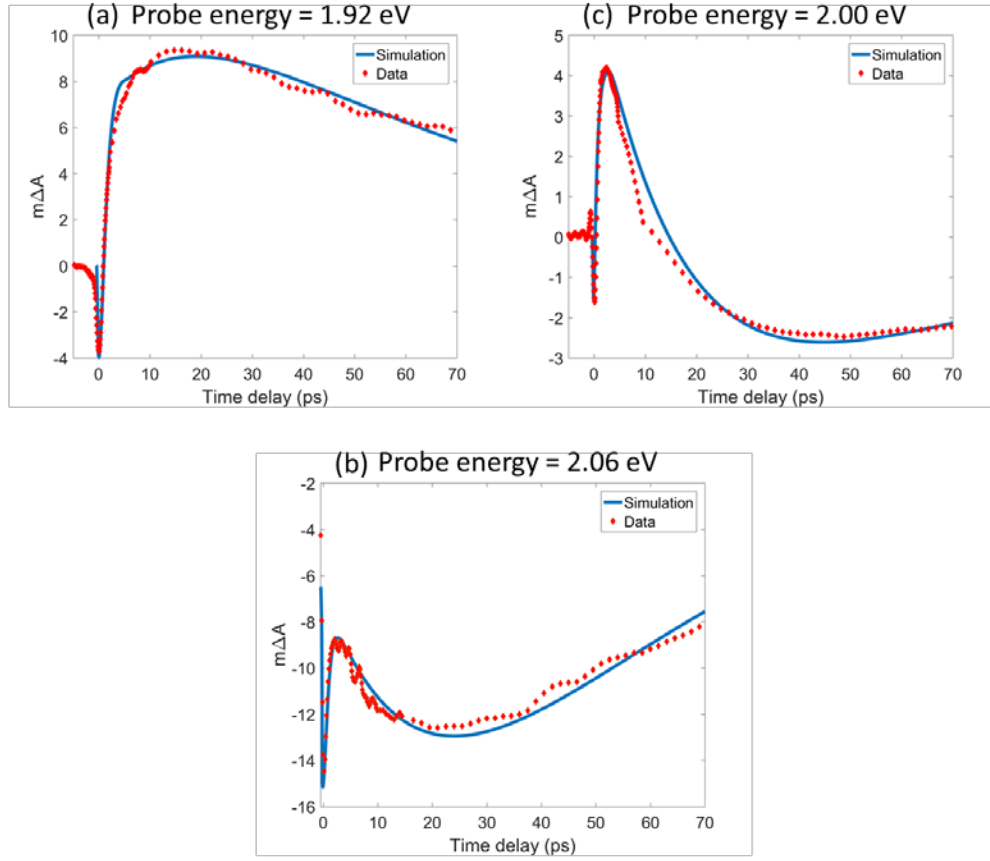


Figure 5.7: Calculated absorbance curves simulating the data in Fig 5.3 using Eqn. 5.7

Strong phonon induced optical bandgap renormalization has been previously predicted in theory for  $\text{MoS}_2$ <sup>126</sup> and  $\text{MoSe}_2$ <sup>153</sup>. The redshift of the excitonic peak with increasing temperature can be modelled using a variant of Varshni equation<sup>158</sup>.

$$E_X(T) = E_X(0) - S \cdot \langle \hbar\omega \rangle \left[ \coth \left( \frac{\langle \hbar\omega \rangle}{2k_B T} \right) - 1 \right] \quad 5.8$$

Where,  $T$  is the lattice temperature,  $S$  is a constant proportional to the electron-phonon coupling and  $\langle \hbar\omega \rangle$  is the average phonon energy. Fig. 5.8 (a) shows the measured absorbance of the A-exciton of  $\text{WS}_2$  at

room temperature and the same peak slightly broadened ( $\sim 5\%$ ) and red shifted by  $22\text{ meV}$  due to phonon induced renormalization<sup>126,129,148</sup>. The difference between the curves ( $\Delta A$ ) is shown in Fig 5.8 (b). The dashed lines represent the probe energies. The energy shift and broadening were chosen to match the values of  $\Delta A$  from *Fig. 5.8* (b) at the probe energies  $1.92\text{ eV}$ ,  $2\text{ eV}$ , and  $2.07\text{ eV}$  (marked by vertical dashed lines) to the contribution of maximum phonon induced renormalization,  $\Delta A_{ph} = \alpha_D(\hbar\omega)n_D(t)$ , extracted from the fits in *Figure 5.7*. The parameters  $S = 2.47$ , and  $E_X(0) = 2.08\text{ eV}$ , were obtained from cold PL data<sup>159</sup>. Using  $\langle\hbar\omega\rangle = 13\text{ meV}$ , also extracted from low temperature PL data, for the average phonon energy results in an estimated maximum lattice temperature increase ( $\sim 20\text{ ps}$ ) of  $30\text{ K}$ . However, near room temperature, the value of  $\langle\hbar\omega\rangle$  is predicted to be closer to that of optical phonons<sup>126</sup> ( $50\text{ meV}$ ) increasing the estimated lattice temperature increase to  $170\text{ K}$ . Using the bulk heat capacity value of  $\text{WS}_2$ <sup>160</sup> and absorbance of  $0.16$  at  $400\text{ nm}$ , if the entire photon energy at a fluence of  $1500\frac{\mu\text{J}}{\text{cm}^2}$  is converted to lattice heating, the increase in temperature is  $\sim 800\text{ K}$ . Therefore, we estimate that about a quarter of the excited carriers relax via phonon-mediated recombination.

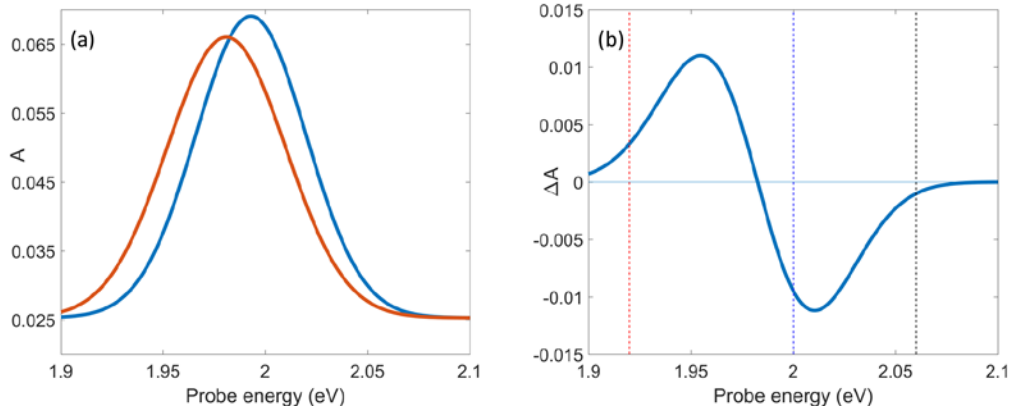


Figure 5.8: (a) Measured room temperature absorbance (blue) and temperature renormalized absorbance using Eqn. 5.8. (b) Change in absorbance due to renormalization.

In summary, we observe a plethora of multi-body effects in TMDs upon high carrier excitations. There are contributions to the transient absorbance signal from Pauli blocking, defect-induced absorption and bandgap renormalization. We observe giant optical bandgap renormalization in  $\text{WS}_2$  (and  $\text{MoS}_2$ ) which we ascribe to the slow buildup of phonons generated through phonon assisted carrier recombination at defect sites. By fitting our data to a simple four level decay model, we estimate the relaxation time scale for phonons in  $\text{WS}_2$  as  $\sim 20$  ps.

# CHAPTER 6.

## Conclusions

In conclusion, 2D materials display strong many-body interactions due to reduced screening. Strong bandgap renormalization is caused when photoexcited carriers relax by transferring energy to phonons. To prove this, I use ultrafast spectroscopy to perform pump-probe measurements on 2D materials. We observe immense many-body interactions in 2D materials manifesting as bandgap renormalization. A summary of the work presented in this thesis is as follows:

In Chapter 2, I introduce the concept of ultrafast light pulses and mathematically describe various parameters of an ultrafast pulse in the time domain and Fourier domain. I give a brief and intuitive description of the physics behind the generation, amplification and measurement of ultrafast pulses. A summary of the thesis is as follows:

In Chapter 3, I describe the electronic and optical properties of graphene, the most popular 2D material. I describe the growth and characterization of CVD graphene. I present pump-probe spectroscopy measurements around the M-point of graphene using which we were able to estimate the Deformation potential for the acoustic phonon mediated bandstructure renormalization.

In Chapter 4, I discuss carrier dynamics in heterostructures of graphene-hexagonal Boron Nitride. We devised a simple optical technique to identify the thickness of hBN flakes on Si/SiO<sub>2</sub> substrates.

Using degenerate pump-probe spectroscopy, we observed that carrier relaxation in graphene-hBN structures is up to four times faster than graphene on Si/SiO<sub>2</sub>. This overcomes the so called hot phonon effect and paves the way for high mobility graphene devices. I also present a two-temperature model to simulate carrier and phonon temperatures in graphene. At the end, I discuss some possible theoretical reasons for the reduced carrier lifetimes in graphene-hBN structures.

Finally, in Chapter 5, I present non-degenerate pump-probe results in WS<sub>2</sub>. Under large photoexcited carrier densities, we see that the transient absorption at larger time delays is dominated by phonon-induced optical bandgap renormalization. These phonons are generated in a multi-phonon assisted carrier recombination process of carriers trapped at defect sites. I also simulate the dynamics using a four-level model and estimate the phonon relaxation lifetime to be around 20 ps.

# Appendix A

## A.1 Transient absorbance curves for MoS<sub>2</sub>

The transient absorption measurements shown in Chapter 5 for WS<sub>2</sub> were conducted on CVD grown MoS<sub>2</sub> also. We see similar renormalization effects in the transient absorption when we change the probe energy. This indicates that phonon-induced bandgap renormalization is a general feature in TMD materials.

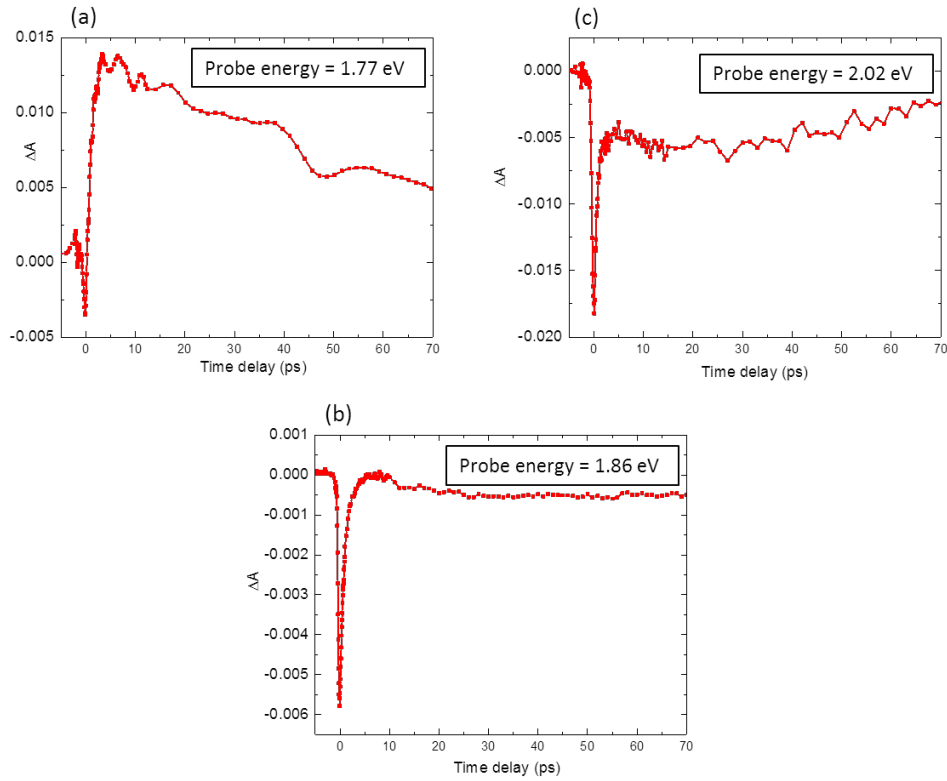


Figure A.1: Transient absorption curves for MoS<sub>2</sub> with probe energy (a) 1.77 eV, (b) 1.86 eV and (c) 2.02 eV. The fluence is fixed at  $1500 \frac{\mu\text{J}}{\text{cm}^2}$ .

Fig A.1 (a) shows the differential absorption for probe energy 1.77 eV which is red shifted from both A and B excitons of MoS<sub>2</sub>. The broad positive signal matches the response for WS<sub>2</sub> with red shifted probe energies as shown in *Fig 5.4* (a). Fig. A1 (b) and (c) show the transient absorption curves at probe energies in resonance with the A and B excitons respectively of MoS<sub>2</sub> showing a broad negative response as expected due to bandgap renormalization. The pump fluence is fixed at  $1500 \frac{\mu\text{J}}{\text{cm}^2}$ .

# Appendix B

As with most scientific endeavors, not all the avenues I explored during my tenure as a graduate student came to fruition. In this section, I will describe some ideas that I pursued or intended to pursue but couldn't due to various reasons.

## B.1 High energy excitons in graphene

The optical absorption of graphene at lower energies is dominated by  $\pi \rightarrow \pi^*$  transitions as explained in chapter 3. The excitonic effect is manifested by a redshift of the van Hove peak by 1 eV. At higher energies, outlying valence and conduction bands come into the picture and it is possible to have resonant excitonic effects at these energies. Li Yang<sup>161</sup> predicts strong resonant excitonic effects at energies higher than 10 eV in graphene and bi-layer graphene. The prominent mechanisms that contribute these effects are  $\sigma \rightarrow \sigma^*$  and  $\sigma \rightarrow \pi^*$  interband transfers. Due to their nearly parallel nature, the  $\sigma \rightarrow \pi^*$  transitions contribute strongly to the excitonic effects as this decreases the relative velocity between the electrons and holes and simultaneously increases the joint density of states. These high energy effects are characterized by two features: A narrow resonant peak at 12.5 eV and a broad peak at  $\sim 13.75$  eV as shown in Fig B.1.

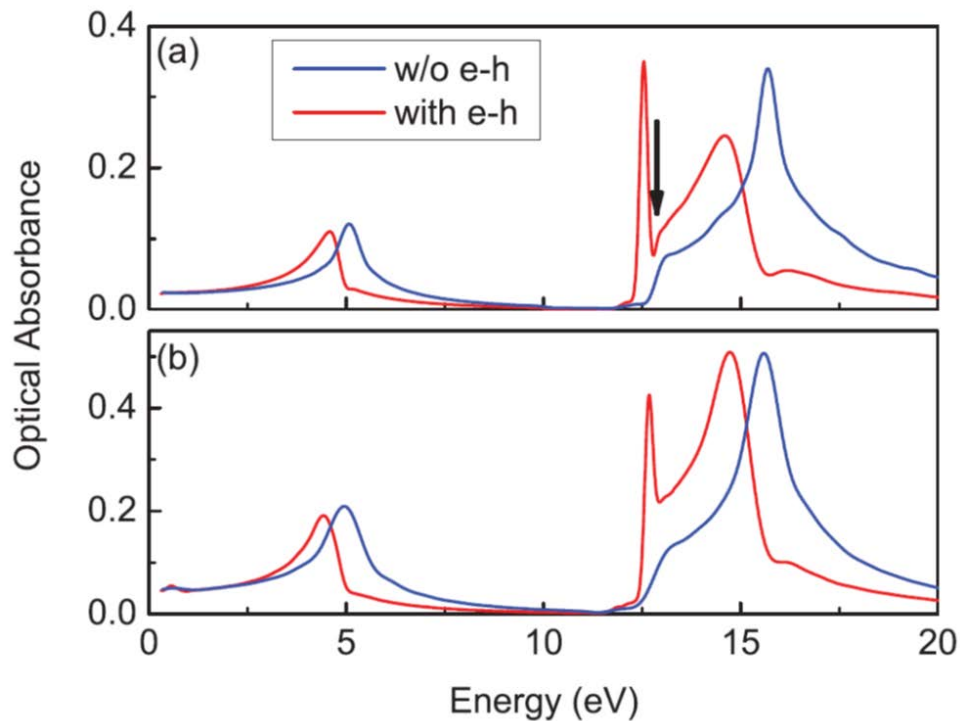


Figure B.1: Optical absorption spectrum with and without electron-hole interactions for (a) monolayer and (b) bilayer graphene. Adapted with permission from Li Yang, “Excitons in intrinsic and bilayer graphene”, *PHYSICAL REVIEW B* **83**, 085405 (2011)

The only experimental work that probes the response of graphene to high-energy photons is by Santoso et al<sup>162</sup> where UV vacuum reflectivity is used to measure optical conductivity of epitaxial graphene from 0 – 35 eV. Although they observed structure in the reflection spectrum for graphite and thick multi-layered graphene, they do not observe any response at high photon energies  $> 10$  eV for monolayer graphene. The low energy spectrum in this work also doesn’t match the low energy spectrum observed by other groups<sup>163</sup> on exfoliated monolayer graphene. This difference is probably due to strong plasmonic

effects inherent in the oblique reflection geometry as well as strong influence from the SiC substrate.

The high energy excitons will be accessible using XUV harmonics produced using HHG. The narrow absorption peak at  $12.54\text{ eV}$  will lie between the 7<sup>th</sup> and 9<sup>th</sup> harmonic of the  $1.6\text{ eV}$  driving laser. The broad peak centered around  $13.75\text{ eV}$  can be sampled using the 9<sup>th</sup> and 11<sup>th</sup> harmonics. More XUV photons in the interesting regions of the absorption spectrum between the odd harmonics of the driving laser can be produced using few-cycle pulses to drive the HHG process or using two pulse driving field for the HHG process.

## B.2 XUV spectroscopy of magnetic materials

Magnetic Tunnel Junctions (MTJ) that have the magnetic easy axis perpendicular to the plane of the sample have been garnering interest because of their potential application in low power and high density MRAM devices. These junctions display a property called perpendicular magnetic anisotropy (PMA)<sup>164,165</sup>. This effect is realized in practice using CoFeB-MgO based thin-film structures. The CoFeB layer plays the role of the ferromagnet and MgO layer is the insulating barrier between two oppositely magnetized CoFeB layers. A strong electric field applied across the layers can be used to manipulate the PMA effect in MTJ devices. This effect is known as Voltage Controlled Magnetic Anisotropy (VCMA)<sup>166,167</sup>. Using voltages to manipulate the magnetization will be more energy efficient than the conventional Spin Transfer Torque (STT) in addition to being compatible with other voltage controlled semiconducting devices. The PMA effect at the

CoFeB-MgO interface is explained by the hybridization of  $2p_z$  electrons of oxygen atom with the  $3d_{z^2}$  electrons in Co/Fe. This can be interpreted as a charge transfer from the oxygen in the MgO layer to the heavy metal (Co/Fe) in the CoFeB layer<sup>168</sup>. Charge transfer has been observed and measured using XUV absorption spectroscopy at the M-edge of Fe ( $\sim 57$  eV) in  $\alpha - Fe_2O_3$  where a charge transfer from the ligand (O) to metal (Fe)<sup>169</sup> has been observed.

To measure the timescales associated with VCMA induced magnetization, we can use pump-probe spectroscopy. For this experiment, a sample with only one CoFeB magnetic layer and without the extra capping layers (as shown in Fig. E2) will suffice. The electric field required to observe VCMA is  $\sim 1 \frac{V}{\text{\AA}}$ . The electric field associated with the  $\sim 40$  fs Ti-Sapphire laser can easily surpass this field requirement if the polarization of the laser has a component into the plane of the sample. Thus, the NIR laser can be used as the pump. If the pump induced VCMA causes a change in the PMA of the interface, charge transfer from MgO to CoFeB should cause a transmission or reflection change in the M-edge of Co/Fe. The XUV radiation produced from HHG in Ne gas can be used as the probe. The probe pulse can sample the transmission or reflection of the M-edge of Co/Fe that lies between 50 – 60 eV where the XUV flux is high if Ne is used as the generating gas.

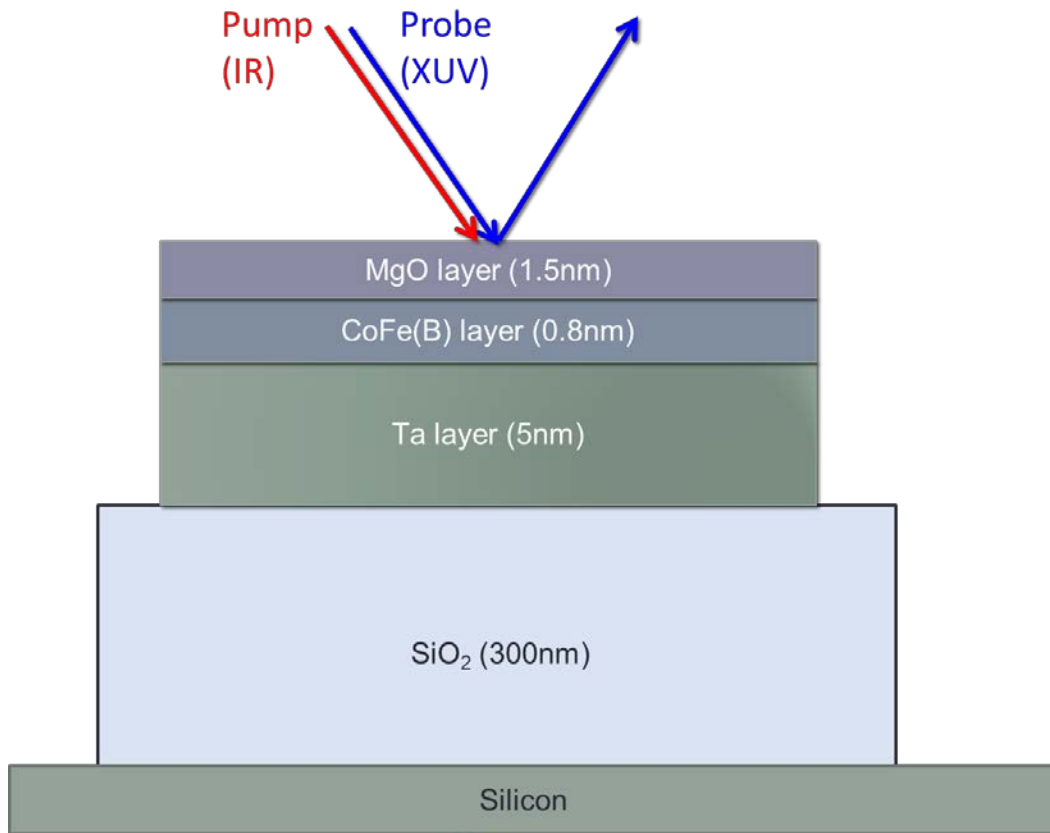


Figure B.2: Sample geometry for probing PMA effect in CoFeB ferromagnet with a MgO insulating capping layer.

# REFERENCES

1. Ippen, E. P., Shank, C. V. & Dienes, A. Passive mode locking of the cw dye laser. *Appl. Phys. Lett.* **21**, 348–350 (1972).
2. Sugioka, K. & Cheng, Y. Ultrafast lasers — reliable tools for advanced materials processing. 1–12 (2014). doi:10.1038/lssa.2014.30
3. Cundiff, S. T. & Ye, J. Colloquium: Femtosecond optical frequency combs. *Rev. Mod. Phys.* **75**, 325–342 (2003).
4. Kane, D. J. Principal components generalized projections: a review [Invited]. *J. Opt. Soc. Am. B* **25**, A120 (2008).
5. Trebino, R. *et al.* REVIEW ARTICLE Measuring ultrashort laser pulses in the time-frequency domain using frequency-resolved optical gating. **68**, 3277–3295 (1997).
6. Novoselov, K. S. *et al.* Electric Field Effect in Atomically Thin Carbon Films. *Science (80-. )*. **306**, 666–669 (2004).
7. Castro Neto, a. H., Peres, N. M. R., Novoselov, K. S. & Geim, a. K. The electronic properties of graphene. *Rev. Mod. Phys.* **81**, 109–162 (2009).
8. Peres, N. M. R. Colloquium: The transport properties of graphene: An introduction. *Rev. Mod. Phys.* **82**, 2673–2700 (2010).
9. Balandin, A. a *et al.* Superior thermal conductivity of single-layer graphene. *Nano Lett.* **8**, 902–7 (2008).
10. Freitag, M., Low, T. & Avouris, P. Increased responsivity of suspended graphene photodetectors. *Nano Lett.* **13**, 1644–1648 (2013).

11. Xing, G., Guo, H., Zhang, X., Sum, T. C. & Huan, C. H. A. The Physics of ultrafast saturable absorption in graphene. *Opt. Express* **18**, 4564–73 (2010).
12. Freitag, M., Low, T. & Avouris, P. Increased Responsivity of Suspended Graphene Photodetectors. (2013).
13. Gan, X. *et al.* Strong enhancement of light-matter interaction in graphene coupled to a photonic crystal nanocavity. *Nano Lett.* **12**, 5626–31 (2012).
14. Freitag, M. *et al.* Energy Dissipation in Graphene Field-Effect Transistors 2009. *Nano* **9**, 1883–1888 (2009).
15. Wang, X., Zhi, L. & Müllen, K. Transparent, conductive graphene electrodes for dye-sensitized solar cells. *Nano Lett.* **8**, 323–327 (2008).
16. Zhou, Q. & Zettl, A. Electrostatic graphene loudspeaker. *Appl. Phys. Lett.* **102**, (2013).
17. Li, X. *et al.* Large-area graphene single crystals grown by low-pressure chemical vapor deposition of methane on copper. *J. Am. Chem. Soc.* **133**, 2816–2819 (2011).
18. Blake, P. *et al.* Making graphene visible. *Appl. Phys. Lett.* **91**, (2007).
19. Ferrari, A. C. & Basko, D. M. Raman spectroscopy as a versatile tool for studying the properties of graphene. *Nat. Nanotechnol.* **8**, 235–46 (2013).
20. Ahn, G. *et al.* Optical Probing of Electronic Interaction between Graphene and Hexagonal Boron Nitride. 1–19 (2013).
21. Das, A. *et al.* Monitoring dopants by Raman scattering in an

- electrochemically top-gated graphene transistor. *Nat. Nanotechnol.* **3**, 210–5 (2008).
22. Roberts, A. *et al.* Response of graphene to femtosecond high-intensity laser irradiation. *Appl. Phys. Lett.* **99**, 2014–2017 (2011).
  23. Ferrari, A. C. Raman spectroscopy of graphene and graphite: Disorder, electron-phonon coupling, doping and nonadiabatic effects. *Solid State Commun.* **143**, 47–57 (2007).
  24. Ferrari, A. C. & Robertson, J. Interpretation of Raman spectra of disordered and amorphous carbon. *Phys. Rev. B* **61**, 14095–14107 (2000).
  25. Ando, T., Zheng, Y. & Suzuura, H. Dynamical Conductivity and Zero-Mode Anomaly in Honeycomb Lattices. *J. Phys. Soc. Japan* **71**, 1318–1324 (2002).
  26. Stauber, T., Peres, N. & Geim, a. Optical conductivity of graphene in the visible region of the spectrum. *Phys. Rev. B* **78**, 85432 (2008).
  27. Mak, K. F. *et al.* Measurement of the optical conductivity of graphene. *Phys. Rev. Lett.* **101**, 196405 (2008).
  28. Dawlaty, J. M. *et al.* Measurement of the Optical Absorption Spectra of Epitaxial Graphene from Terahertz to Visible. 2–6 (2008). doi:10.1063/1.2990753
  29. Nair, R. R. *et al.* Fine structure constant defines visual transparency of graphene. *Science* **320**, 1308 (2008).
  30. Chae, D. H. *et al.* Excitonic fano resonance in free-standing graphene. *Nano Lett.* **11**, 1379–1382 (2011).
  31. Mak, K. F., Shan, J. & Heinz, T. F. Seeing Many-Body Effects in

- Single- and Few-Layer Graphene: Observation of Two-Dimensional Saddle-Point Excitons. *Phys. Rev. Lett.* **106**, 46401 (2011).
32. Malic, E., Winzer, T., Bobkin, E. & Knorr, A. Microscopic theory of absorption and ultrafast many-particle kinetics in graphene. **205406**, (2011).
  33. Adam Thomas Roberts. Time Domain Spectroscopy of Graphene. 1–270 (2008).
  34. Winnerl, S. *et al.* Carrier Relaxation in Epitaxial Graphene Photoexcited Near the Dirac Point. *Phys. Rev. Lett.* **107**, 237401 (2011).
  35. Kadi, F. *et al.* Microscopic description of intraband absorption in graphene: The occurrence of transient negative differential transmission. *Phys. Rev. Lett.* **113**, 1–5 (2014).
  36. Dawlaty, J. M., Shivaraman, S., Chandrashekar, M., Rana, F. & Spencer, M. G. Measurement of ultrafast carrier dynamics in epitaxial graphene. *Appl. Phys. Lett.* **92**, 42113–42116 (2008).
  37. Bolotin, K. I., Sikes, K. J., Hone, J., Stormer, H. L. & Kim, P. Temperature-dependent transport in suspended graphene. *Phys. Rev. Lett.* **101**, 1–4 (2008).
  38. Fratini, S. & Guinea, F. Substrate-limited electron dynamics in graphene. *Phys. Rev. B - Condens. Matter Mater. Phys.* **77**, 1–6 (2008).
  39. Chen, J.-H., Jang, C., Xiao, S., Ishigami, M. & Fuhrer, M. S. Intrinsic and extrinsic performance limits of graphene devices on SiO<sub>2</sub>. *Nat. Nanotechnol.* **3**, 206–209 (2008).

40. Chen, J.-H., Jang, C., Xiao, S., Ishigami, M. & Fuhrer, M. S. Intrinsic and extrinsic performance limits of graphene devices on SiO<sub>2</sub>. *Nat. Nanotechnol.* **3**, 206–209 (2008).
41. Kaasbjerg, K., Thygesen, K. S. & Jacobsen, K. W. Unraveling the acoustic electron-phonon interaction in graphene. *Phys. Rev. B* **85**, 165440 (2012).
42. Borysenko, K. M. *et al.* First-principles analysis of electron-phonon interactions in graphene. *Phys. Rev. B - Condens. Matter Mater. Phys.* **81**, 3–6 (2010).
43. Kaasbjerg, K., Bhargavi, K. S. & Kubakaddi, S. S. Hot-electron cooling by acoustic and optical phonons in monolayers of MoS<sub>2</sub> and other transition-metal dichalcogenides. *Phys. Rev. B - Condens. Matter Mater. Phys.* **90**, 1–13 (2014).
44. Kaasbjerg, K., Thygesen, K. S. & Jacobsen, K. W. Unraveling the acoustic electron-phonon interaction in graphene. *Phys. Rev. B - Condens. Matter Mater. Phys.* **85**, 7–9 (2012).
45. Breusing, M. *et al.* Ultrafast nonequilibrium carrier dynamics in a single graphene layer. *Phys. Rev. B* **83**, 153410 (2011).
46. Binder, R., Roberts, A. T., Kwong, N. H., Sandhu, A. & Everitt, H. O. Global k-space analysis of electron-phonon interaction in graphene and application to M<sub>2</sub> point spectroscopy. *Phys. Rev. B* **93**, 85414 (2016).
47. Dean, C. R. *et al.* Boron nitride substrates for high-quality graphene electronics. *Nat. Nanotechnol.* **5**, 722–726 (2010).
48. Xue, J. *et al.* Scanning tunnelling microscopy and spectroscopy of ultra-flat graphene on hexagonal boron nitride. *Nat. Mater.* **10**,

- 282–5 (2011).
49. Decker, R. *et al.* Local electronic properties of graphene on a BN substrate via scanning tunneling microscopy. *Nano Lett.* **11**, 2291–2295 (2011).
  50. Ponomarenko, L. A. *et al.* Tunable metal–insulator transition in double-layer graphene heterostructures. *Nat. Phys.* **7**, 958–961 (2011).
  51. Mayorov, A. S. *et al.* Micrometer-scale ballistic transport in encapsulated graphene at room temperature. *Nano Lett.* **11**, 2396–9 (2011).
  52. Park, C.-H., Yang, L., Son, Y.-W., Cohen, M. L. & Louie, S. G. Anisotropic behaviours of massless Dirac fermions in graphene under periodic potentials. *Nat. Phys.* **4**, 213–217 (2008).
  53. Yankowitz, M. *et al.* Emergence of superlattice Dirac points in graphene on hexagonal boron nitride. *Nat. Phys.* **8**, 382–386 (2012).
  54. Park, C.-H., Yang, L., Son, Y.-W., Cohen, M. & Louie, S. New Generation of Massless Dirac Fermions in Graphene under External Periodic Potentials. *Phys. Rev. Lett.* **101**, 126804 (2008).
  55. Watanabe, K., Taniguchi, T. & Kanda, H. Direct-bandgap properties and evidence for ultraviolet lasing of hexagonal boron nitride single crystal. *Nat. Mater.* **3**, 404–409 (2004).
  56. Mak, K. F., He, K., Shan, J. & Heinz, T. F. Control of valley polarization in monolayer MoS<sub>2</sub> by optical helicity. *Nat. Nanotechnol.* **7**, 494–498 (2012).
  57. Wang, X., Zhao, M. & Nolte, D. D. Optical contrast and clarity of

- graphene on an arbitrary substrate. *Appl. Phys. Lett.* **95**, 81102 (2009).
58. Taniguchi, T. & Watanabe, K. Synthesis of high-purity boron nitride single crystals under high pressure by using Ba-BN solvent. *J. Cryst. Growth* **303**, 525–529 (2007).
  59. Roberts, A., Shivaram, N., Xu, L. & Sandhu, A. Optimization of few-cycle pulse generation: spatial size, mode quality and focal volume effects in filamentation based pulse compression. *Opt. Express* **17**, 23894–23902 (2009).
  60. Golla, D. *et al.* Optical thickness determination of hexagonal boron nitride flakes. *Appl. Phys. Lett.* **102**, 161906 (2013).
  61. STENZEL, O. *et al.* *Physica status solidi. A, Applied research : PSS. Physica status solidi. A. Applied research* **158**, ([Akademie Verlag], 1970).
  62. Palik, E. D. *Handbook of optical constants of solids*. (Academic Press, 1998).
  63. Zomer, P. J., Guimares, M. H. D., Brant, J. C., Tombros, N. & Van Wees, B. J. Fast pick up technique for high quality heterostructures of bilayer graphene and hexagonal boron nitride. *Appl. Phys. Lett.* **105**, (2014).
  64. Suk, J. W. *et al.* Transfer of CVD-grown monolayer graphene onto arbitrary substrates. *ACS Nano* **5**, 6916–6924 (2011).
  65. Wang, L. *et al.* Negligible environmental sensitivity of graphene in a hexagonal boron nitride/graphene/h-BN sandwich structure. *ACS Nano* **6**, 9314–9319 (2012).
  66. Geim, A. K. & Grigorieva, I. V. Van der Waals heterostructures.

- Nature* **499**, 419–25 (2013).
67. Wang, H. *et al.* Ultrafast relaxation dynamics of hot optical phonons in graphene. *Appl. Phys. Lett.* **96**, 1–4 (2010).
  68. Strait, J. H. *et al.* Very slow cooling dynamics of photoexcited carriers in graphene observed by optical-pump terahertz-probe spectroscopy. *Nano Lett.* **11**, 4902–4906 (2011).
  69. Johannsen, J. C. *et al.* Direct View of Hot Carrier Dynamics in Graphene. *Phys. Rev. Lett.* **111**, 27403 (2013).
  70. Iglesias, J. M., Martín, M. J., Pascual, E. & Rengel, R. Hot carrier and hot phonon coupling during ultrafast relaxation of photoexcited electrons in graphene. *Appl. Phys. Lett.* **108**, (2016).
  71. Lazzeri, M., Piscanec, S., Mauri, F., Ferrari, A. C. & Robertson, J. Electron transport and hot phonons in carbon nanotubes. *Phys. Rev. Lett.* **95**, 1–4 (2005).
  72. Pop, E. *et al.* Negative differential conductance and hot phonons in suspended nanotube molecular wires. *Phys. Rev. Lett.* **95**, 1–4 (2005).
  73. Lazzeri, M. & Mauri, F. Coupled dynamics of electrons and phonons in metallic nanotubes: Current saturation from hot-phonon generation. *Phys. Rev. B - Condens. Matter Mater. Phys.* **73**, 1–6 (2006).
  74. Gao, B. *et al.* Studies of intrinsic hot phonon dynamics in suspended graphene by transient absorption microscopy. *Nano Lett.* **11**, 3184–3189 (2011).
  75. Bistrizter, R. & MacDonald, A. H. Electronic cooling in graphene. *Phys. Rev. Lett.* **102**, 13–16 (2009).

76. Low, T., Perebeinos, V., Kim, R., Freitag, M. & Avouris, P. Cooling of photoexcited carriers in graphene by internal and substrate phonons. *Phys. Rev. B - Condens. Matter Mater. Phys.* **86**, 1–9 (2012).
77. Hwang, E. H. & Das Sarma, S. Surface polar optical phonon interaction induced many-body effects and hot-electron relaxation in graphene. *Phys. Rev. B - Condens. Matter Mater. Phys.* **87**, 1–10 (2013).
78. Ahn, S., Hwang, E. H. & Min, H. Inelastic carrier lifetime in a coupled graphene/electron-phonon system: Role of plasmon-phonon coupling. *Phys. Rev. B - Condens. Matter Mater. Phys.* **90**, 1–7 (2014).
79. Bonini, N., Lazzeri, M., Marzari, N. & Mauri, F. Phonon anharmonicities in graphite and graphene. *Phys. Rev. Lett.* **99**, 1–4 (2007).
80. Song, D. *et al.* Direct measurement of the lifetime of optical phonons in single-walled carbon nanotubes. *Phys. Rev. Lett.* **100**, 225503 (2008).
81. Yan, H. *et al.* Time-resolved Raman spectroscopy of optical phonons in graphite: Phonon anharmonic coupling and anomalous stiffening. *Phys. Rev. B - Condens. Matter Mater. Phys.* **80**, 1–4 (2009).
82. Kang, K., Abdula, D., Cahill, D. G. & Shim, M. Lifetimes of optical phonons in graphene and graphite by time-resolved incoherent anti-Stokes Raman scattering. *Phys. Rev. B - Condens. Matter Mater. Phys.* **81**, 1–6 (2010).

83. Li, J. *et al.* Phonon-limited carrier mobility and resistivity from carbon nanotubes to graphene. *Phys. Rev. B - Condens. Matter Mater. Phys.* **92**, 29–35 (2015).
84. Gabor, N. M. *et al.* Hot carrier-assisted intrinsic photoresponse in graphene. *Science* **334**, 648–52 (2011).
85. Duan, J. *et al.* High thermoelectric power factor in graphene/hBN devices. *Proc. Natl. Acad. Sci.* 201615913 (2016). doi:10.1073/pnas.1615913113
86. Lui, C. H., Mak, K. F., Shan, J. & Heinz, T. F. Ultrafast Photoluminescence from Graphene. *Phys. Rev. Lett.* **105**, 127404 (2010).
87. Jiang, L. & Tsai, H.-L. Improved Two-Temperature Model and Its Application in Ultrashort Laser Heating of Metal Films. *J. Heat Transfer* **127**, 1167 (2005).
88. Lui, C. H., Mak, K. F., Shan, J. & Heinz, T. F. Ultrafast photoluminescence from graphene. *Phys. Rev. Lett.* **105**, 1–4 (2010).
89. Katsidis, C. C. & Siapkas, D. I. General transfer-matrix method for optical multilayer systems with coherent, partially coherent, and incoherent interference. *Appl. Opt.* **41**, 3978 (2002).
90. Shah, J. *Ultrafast spectroscopy of semiconductors and semiconductor nanostructures.* (Springer).
91. Falkovsky, L. A. . b. Thermodynamics of electron-hole liquids in graphene. *JETP Lett.* **98**, 161–164 (2013).
92. Edgar, J. H. *Properties of Group III Nitrides.* (Institution of Engineering and Technology, 1994).

93. Chen, C. C., Li, Z., Shi, L. & Cronin, S. B. Thermal interface conductance across a graphene/hexagonal boron nitride heterojunction. *Appl. Phys. Lett.* **104**, (2014).
94. Mao, R. *et al.* Phonon engineering in nanostructures: Controlling interfacial thermal resistance in multilayer-graphene/dielectric heterojunctions. *Appl. Phys. Lett.* **101**, 10–14 (2012).
95. Pak, A. J. & Hwang, G. S. Theoretical Analysis of Thermal Transport in Graphene Supported on Hexagonal Boron Nitride: The Importance of Strong Adhesion Due to  $\pi$ -Bond Polarization. *Phys. Rev. Appl.* **6**, 34015 (2016).
96. Zhang, J., Hong, Y. & Yue, Y. Thermal transport across graphene and single layer hexagonal boron nitride. *J. Appl. Phys.* **117**, 134307 (2015).
97. Li, T., Tang, Z., Huang, Z. & Yu, J. Interfacial thermal resistance of 2D and 1D carbon/hexagonal boron nitride van der Waals heterostructures. *Carbon N. Y.* **105**, 566–571 (2016).
98. Kampfrath, T., Perfetti, L., Schapper, F., Frischkorn, C. & Wolf, M. Strongly Coupled Optical Phonons in the Ultrafast Dynamics of the Electronic Energy and Current Relaxation in Graphite. *Phys. Rev. Lett.* **95**, 187403 (2005).
99. Song, J. C. W., Reizer, M. Y. & Levitov, L. S. Disorder-assisted electron-phonon scattering and cooling pathways in graphene. *Phys. Rev. Lett.* **109**, 1–5 (2012).
100. Graham, M. W. *et al.* Transient absorption and photocurrent microscopy show that hot electron supercollisions describe the rate-limiting relaxation step in graphene. *Nano Lett.* **13**, 5497–

5502 (2013).

101. Alencar, T. V., Silva, M. G., Malard, L. M. & De Paula, A. M. Defect-induced supercollision cooling of photoexcited carriers in graphene. *Nano Lett.* **14**, 5621–5624 (2014).
102. Graham, M. W., Shi, S.-F., Ralph, D. C., Park, J. & McEuen, P. L. Photocurrent measurements of supercollision cooling in graphene. *Nat. Phys.* **9**, 103–108 (2013).
103. Betz, A. C. *et al.* Supercollision cooling in undoped graphene. *Nat. Phys.* **9**, 109–112 (2013).
104. Principi, A. *et al.* Super-Planckian Electron Cooling in a van der Waals Stack. *Phys. Rev. Lett.* **118**, 1–7 (2017).
105. Tielrooij, K. J. *et al.* Out-of-plane heat transfer in van der Waals stacks: electron-hyperbolic phonon coupling. 1–11 (2017).
106. Amani, M. *et al.* Near-unity photoluminescence quantum yield in MoS<sub>2</sub>. *Science (80-. )*. (2015). doi:10.1126/science.aad2114
107. Robert, C. *et al.* Exciton radiative lifetime in transition metal dichalcogenide monolayers. *Phys. Rev. B* **93**, 1–10 (2016).
108. Lagarde, D. *et al.* Carrier and polarization dynamics in monolayer MoS<sub>2</sub>. *Phys. Rev. Lett.* **112**, 1–5 (2014).
109. Chen, K. *et al.* Experimental evidence of exciton capture by mid-gap defects in CVD grown monolayer MoSe<sub>2</sub>. *npj 2D Mater. Appl.* **1**, 15 (2017).
110. Wang, H. *et al.* Fast exciton annihilation by capture of electrons or holes by defects via Auger scattering in monolayer metal dichalcogenides. *Phys. Rev. B - Condens. Matter Mater. Phys.* **91**, 17–19 (2015).

111. Wang, H., Zhang, C. & Rana, F. Ultrafast dynamics of defect-assisted electron-hole recombination in monolayer MoS<sub>2</sub>. *Nano Lett.* **15**, 339–345 (2015).
112. Sun, D. *et al.* Observation of Rapid Exciton – Exciton Annihilation in Monolayer Molybdenum Disulfide. *Nano Lett.* **14**, 5625 (2014).
113. Yuan, L. & Huang, L. Exciton dynamics and annihilation in WS<sub>2</sub> 2D semiconductors. *Nanoscale* **7**, 7402–7408 (2015).
114. Wu, Z. *et al.* Defects as a factor limiting carrier mobility in WSe<sub>2</sub>: A spectroscopic investigation. *Nano Res.* **9**, 3622–3631 (2016).
115. Golla, D., Brasington, A., LeRoy, B. J. & Sandhu, A. Ultrafast relaxation of hot phonons in graphene-hBN heterostructures. *APL Mater.* **5**, 1–16 (2017).
116. Kaasbjerg, K., Thygesen, K. S. & Jacobsen, K. W. Phonon-limited mobility in n-type single-layer MoS<sub>2</sub> from first principles. *Phys. Rev. B - Condens. Matter Mater. Phys.* **85**, 1–16 (2012).
117. Moody, G., Schaibley, J. & Xu, X. Exciton Dynamics in Monolayer Transition Metal Dichalcogenides. 1–27 (2016). doi:10.1364/JOSAB.33.000C39
118. Korn, T., Heydrich, S., Hirmer, M., Schmutzler, J. & Schiller, C. Low-temperature photocarrier dynamics in monolayer MoS<sub>2</sub>. *Appl. Phys. Lett.* **99**, (2011).
119. Wang, G. *et al.* Polarization and time-resolved photoluminescence spectroscopy of excitons in MoSe<sub>2</sub> monolayers. *Appl. Phys. Lett.* **106**, 6–9 (2015).
120. Tongay, S. *et al.* Thermally Driven Crossover from Indirect toward Direct Bandgap in 2D Semiconductors: MoSe<sub>2</sub> versus MoS<sub>2</sub>. *Nano*

- Lett.* **12**, 5576–5580 (2012).
121. Yan, T., Qiao, X., Liu, X., Tan, P. & Zhang, X. Photoluminescence properties and exciton dynamics in monolayer WSe<sub>2</sub>. **101901**, (2015).
  122. Wei, X. L. *et al.* Phonon thermal conductivity of monolayer MoS<sub>2</sub>: A comparison with single layer graphene. *Appl. Phys. Lett.* **105**, 5 (2014).
  123. Saha, D. & Mahapatra, S. Analytical insight into the lattice thermal conductivity and heat capacity of monolayer MoS<sub>2</sub>. *Phys. E Low-Dimensional Syst. Nanostructures* **83**, 455–460 (2016).
  124. Yan, R. *et al.* Thermal conductivity of monolayer molybdenum disulfide obtained from temperature-dependent Raman spectroscopy. *ACS Nano* **8**, 986–993 (2014).
  125. Cai, Y., Lan, J., Zhang, G. & Zhang, Y. W. Lattice vibrational modes and phonon thermal conductivity of monolayer MoS<sub>2</sub>. *Phys. Rev. B - Condens. Matter Mater. Phys.* **89**, 1–8 (2014).
  126. Molina-s, A., Palummo, M., Marini, A. & Wirtz, L. Temperature-dependent excitonic effects in the optical properties of single-layer MoS<sub>2</sub>. **155435**, 1–8 (2016).
  127. Pogna, E. A. A. *et al.* Photo-induced bandgap renormalization governs the ultrafast response of single-layer MoS<sub>2</sub>. *ACS Nano* **10**, 1182–1188 (2016).
  128. Zhang, S. *et al.* Direct Observation of Degenerate Two-Photon Absorption and Its Saturation in WS<sub>2</sub> and MoS<sub>2</sub> Monolayer and Few-Layer Films. *ACS Nano* 150713134910007 (2015). doi:10.1021/acsnano.5b03480

129. Sim, S. *et al.* Exciton dynamics in atomically thin MoS<sub>2</sub>: Interexcitonic interaction and broadening kinetics. *Phys. Rev. B - Condens. Matter Mater. Phys.* **88**, 1–5 (2013).
130. Nie, Z. *et al.* Ultrafast Electron and Hole Relaxation Pathways in Few-Layer MoS<sub>2</sub>. *J. Phys. Chem. C* **119**, 20698–20708 (2015).
131. You, Y. *et al.* Observation of biexcitons in monolayer WSe<sub>2</sub>. *Nat. Phys.* **11**, 477–481 (2015).
132. Sie, E. J., Frenzel, A. J., Lee, Y. H., Kong, J. & Gedik, N. Intervalley biexcitons and many-body effects in monolayer MoS<sub>2</sub>. *Phys. Rev. B - Condens. Matter Mater. Phys.* **92**, 1–8 (2015).
133. Wang, Z. W., Li, W. P., Xiao, Y., Li, R. Z. & Li, Z. Q. Influence of exciton-phonons coupling on the exciton binding energy in monolayer transition metal dichalcogenides. *Appl. Phys. Lett.* **110**, 1–7 (2017).
134. Ceballos, F., Cui, Q., Bellus, M. Z. & Zhao, H. Exciton formation in monolayer transition metal dichalcogenides. *Nanoscale* **8**, 11681–11688 (2016).
135. Steinleitner, P. *et al.* Direct Observation of Ultrafast Exciton Formation in a Monolayer of WSe<sub>2</sub>. 2–7 (2017). doi:10.1021/acs.nanolett.6b04422
136. Chen, K. *et al.* Carrier Trapping by Oxygen Impurities in Molybdenum Diselenide.
137. Kostoulas, Y., Ucer, K. B., Wicks, G. W. & Fauchet, P. M. Femtosecond carrier dynamics in low-temperature grown Ga<sub>0.51</sub>In<sub>0.49</sub>P. *Appl. Phys. Lett.* **67**, 3756 (1995).
138. Kostoulas, Y., Waxer, L. J., Walmsley, I. a., Wicks, G. W. &

- Fauchet, P. M. Femtosecond carrier dynamics in low-temperature-grown indium phosphide. *Appl. Phys. Lett.* **66**, 1821 (1995).
139. Gupta, S. *et al.* Subpicosecond carrier lifetime in GaAs grown by molecular beam epitaxy at low temperatures. *Appl. Phys. Lett.* **59**, 3276–3278 (1991).
140. Harmon, "E.S. *et al.* Carrier lifetime versus anneal in low temperature growth {GaAs}. *Appl.Phys.Lett.*63(16),1993 2248-2250 **63**, 2248–2250 (1993).
141. Su, W., Jin, L., Qu, X., Huo, D. & Yang, L. Defect passivation induced strong photoluminescence enhancement of rhombic monolayer MoS<sub>2</sub>. *Phys. Chem. Chem. Phys.* **18**, 14001–14006 (2016).
142. Chow, P. K. *et al.* Defect-Induced Photoluminescence in Monolayer Semiconducting Transition Metal Dichalcogenides. *ACS Nano* **9**, 1520–1527 (2015).
143. Tongay, S. *et al.* Defects activated photoluminescence in two-dimensional semiconductors: interplay between bound, charged and free excitons. *Sci. Rep.* **3**, 2657 (2013).
144. Nan, H. *et al.* Strong Photoluminescence Enhancement of MoS<sub>2</sub> through Defect Engineering and Oxygen Bonding. *{ACS} Nano* **8**, 5738–5745 (2014).
145. Zhou, W. *et al.* Intrinsic structural defects in monolayer molybdenum disulfide. *Nano Lett.* **13**, 2615–2622 (2013).
146. Wei, X. *et al.* Mo-O bond doping and related-defect assisted enhancement of photoluminescence in monolayer MoS<sub>2</sub>. *AIP Adv.* **4**, (2014).

147. Lin, Z. *et al.* Defect engineering of two-dimensional transition metal dichalcogenides. *2D Mater.* **3**, 22002 (2016).
148. Cunningham, P. D. *et al.* Charge Trapping and Exciton Dynamics in Large-Area CVD Grown MoS<sub>2</sub>. *J. Phys. Chem. C* **120**, 5819–5826 (2016).
149. Jahnke, F., Wehling, T. O. & Gies, C. Influence of Excited Carriers on the Optical and Electronic Properties of MoS<sub>2</sub>. (2014). doi:10.1021/nl500595u
150. Chernikov, A., Ruppert, C., Hill, H. M., Rigosi, A. F. & Heinz, T. F. Population inversion and giant bandgap renormalization in atomically thin WS<sub>2</sub> layers. *Nat. Photonics* **9**, 466–470 (2015).
151. Wang, H., Zhang, C. & Rana, F. Ultrafast Dynamics of Defect-Assisted Electron – Hole Recombination in Monolayer MoS<sub>2</sub>. *Nano Lett.* **15**, 339–345 (2015).
152. Liang, Y. *et al.* New Mechanism for Strongly Bound Excitons in Gapless Two-Dimensional Structures. *arXiv:1401.6663 [cond-mat]* **115418**, 2–7 (2014).
153. Tongay, S. *et al.* Thermally driven crossover from indirect toward direct bandgap in 2D Semiconductors: MoSe<sub>2</sub> versus MoS<sub>2</sub>. *Nano Lett.* **12**, 5576–5580 (2012).
154. Molina-s, A., Palumbo, M., Marini, A. & Wirtz, L. Temperature dependent excitonic effects in the optical properties of single-layer MoS<sub>2</sub>. 1–9 (2016).
155. Sercel, P. C. Multiphonon-assisted tunneling through deep levels: A rapid energy-relaxation mechanism in nonideal quantum-dot heterostructures. *Phys. Rev. B* **51**, 14532–14541 (1995).

156. Schroeter, D., Griffiths, D. & Sercel, P. Defect-assisted relaxation in quantum dots at low temperature. *Phys. Rev. B* **54**, 1486–1489 (1996).
157. Yang, J.-H., Shi, L., Wang, L.-W. & Wei, S.-H. Non-Radiative Carrier Recombination Enhanced by Two-Level Process: A First-Principles Study. *Sci. Rep.* **6**, 21712 (2016).
158. O'Donnell, K. P. & Chen, X. Temperature dependence of semiconductor band gaps. *Appl. Phys. Lett.* **58**, 2924–2926 (1991).
159. He, Z. *et al.* Layer-dependent modulation of tungsten disulfide photoluminescence by lateral electric fields. *ACS Nano* **9**, 2740–2748 (2015).
160. Peng, B. *et al.* Thermal conductivity of monolayer MoS<sub>2</sub>, MoSe<sub>2</sub>, and WS<sub>2</sub>: Interplay of mass effect, interatomic bonding and anharmonicity. **2**, 5767–5773 (2015).
161. Yang, L. Excitons in intrinsic and bilayer graphene. **85405**, 1–5 (2011).
162. Santoso, I. *et al.* Observation of room-temperature high-energy resonant excitonic effects in graphene. *Phys. Rev. B - Condens. Matter Mater. Phys.* **84**, 1–4 (2011).
163. Mak, K. F., Ju, L., Wang, F. & Heinz, T. F. Optical spectroscopy of graphene: From the far infrared to the ultraviolet. *Solid State Commun.* **152**, 1341–1349 (2012).
164. Peng, S. *et al.* Origin of interfacial perpendicular magnetic anisotropy in MgO/CoFe/metallic capping layer structures. *Sci. Rep.* **5**, 18173 (2015).
165. Endo, M., Kanai, S., Ikeda, S., Matsukura, F. & Ohno, H. Electric-

- field effects on thickness dependent magnetic anisotropy of sputtered MgO/Co<sub>40</sub>Fe<sub>40</sub>B<sub>20</sub>/Ta structures. *Appl. Phys. Lett.* **96**, 2013–2016 (2010).
166. Bauer, U., Przybylski, M. & Beach, G. S. D. Voltage control of magnetic anisotropy in Fe films with quantum well states. *Phys. Rev. B* **89**, 174402 (2014).
167. Wang, W.-G., Li, M., Hageman, S. & Chien, C. L. Electric-field-assisted switching in magnetic tunnel junctions. *Nat. Mater.* **11**, 64–68 (2011).
168. Khoo, K. H. *et al.* First-principles study of perpendicular magnetic anisotropy in CoFe/MgO and CoFe/Mg<sub>3</sub>B<sub>2</sub>O<sub>6</sub> interfaces. *Phys. Rev. B - Condens. Matter Mater. Phys.* **87**, 1–6 (2013).
169. Vura-Weis, J. *et al.* Femtosecond M<sub>2,3</sub>-Edge Spectroscopy of Transition-Metal Oxides: Photoinduced Oxidation State Change in  $\alpha$ -Fe<sub>2</sub>O<sub>3</sub>. *J. Phys. Chem. Lett.* **4**, 3667–3671 (2013).